UNIVERSITY OF OKLAHOMA

GRADUATE COLLEGE

STABILITY DOMAINS AND BIFURCATIONS IN SERIES COMPENSATED POWER NETWORKS SUBJECTED TO ASYNCHRONOUS WIND GENERATION AND INDUCTION MOTOR DYNAMICS

A DISSERTATION

SUBMITTED TO THE GRADUATE FACULTY

in partial fulfillment of the requirements for the

Degree of

DOCTOR OF PHILOSOPHY

By

JONATHAN DEVADASON
Norman, Oklahoma
2021

STABILITY DOMAINS AND BIFURCATIONS IN SERIES COMPENSATED POWER NETWORKS SUBJECTED TO ASYNCHRONOUS WIND GENERATION AND INDUCTION MOTOR DYNAMICS

A DISSERTATION APPROVED FOR THE
SCHOOL OF ELECTRICAL AND COMPUTER ENGINEERING

BY THE COMMITTEE CONSISTING OF

Dr. Paul S. Moses, Chair

Dr. Jie Cai, Outside Member

Dr. Choon Yik Tang, Member

Dr. John N. Jiang, Member

Acknowledgments

I would like to first thank my supervisor, Dr. Paul S. Moses for all his contributions during my doctorate. His guidance and encouragement have proven invaluable to me and have made me the researcher I am today. Next, I would like to thank the members of my doctoral committee for serving in this role, as well as, for their many contributions: Dr. Choon Yik Tang for his helpful instruction during the Control Theory course, Dr. John Jiang for giving me helpful feedback about my teaching, and Dr. Jie Cai for his words of encouragement about my research. I would also like to thank Dr. Mohammad A.S. Masoum of Utah Valley University for his helpful guidance and advice during the preparation of my journal papers. Next, I would like to thank my dear parents, Mr. Joseph, and Dr. Reenie Devadason for the many sacrifices they have made for my education. Throughout the years, their unwavering love and support have guided me through the most difficult times, especially during my move to the United States. I would also like to thank my brother Mr. Moses Devadason for his care and friendship. I am very grateful for the years of instruction and resources I received from the faculty and staff of the Electrical and Computer Engineering Department. In particular, I wish to thank Dr. Rodney Keele for all the administrative help and chocolate, Dr. Chad Davis for the opportunity to serve as his teaching assistant during my last three semesters to help me gain experience to start my career as an educator. I would like to now thank my chosen family and friends for their love and support including my adopted big sister Dr. Katryn Pasaribu, grandparents Mr. Sam and Ms. Yvonne Satterfield from First Baptist Church Knoxville, big brothers Michael Henderson and Derek Mehl, little sibling Skyler Moomey, little brother Josh Cater, little sister Krista Henderson, Mr. Daniel Glover, Dr. Wanghao Fei, Mr. Jace Huser, Mr. Garrett and Ms. Stephanie Robberson, Mr. Ali Sajadian, Mr. Mojtaba Jalalpour, Mr. Blake Woods, Ms. Melissa Gray and so many others who have loved and encouraged me to persevere. I would like to acknowledge now, my

parents-in-law Mr. Vance and Mrs. Wanda Martin, my brother and sister-in-law - Mr. Nathan and Ms. Kathryn Martin and my grandma-in-law - Ms. Dora Waguespack who have played a significant role in my well-being. Finally, I want to thank my wonderful husband, Benjamin Elliot Martin, M.D who gave me all his love and support towards the completion of my doctorate.

Jonathan Devadason

Table of Contents

List of Figures

List of Tables

Abstract

There are significant concerns regarding the stability of weak power grids due to feeders of high impedance. This thesis investigates the stability domain of Squirrel Cage Induction Generator - Wind Turbines (SCIG-WTs) with series compensation and weak interconnections to the power grid. Detailed time-domain and state-space modeling have revealed new bifurcations and oscillatory modes for a SCIG-WT connected radially or non-radially to a weak grid through a series compensated line. The stability domain analyses are carried out by computing bifurcations in the system by analyzing eigenvalues of the linearized system.

A Static Var Compensator (SVC) with an improved voltage regulator design has been proposed to improve the stability domain of the radial system with respect to series compensation. The analyses demonstrate for the first time how the degree of compensation at which the Hopf bifurcation occurs depends on the X/R ratio of the line, operating slip of the induction generator, and voltage regulator parameters as well as the time delays in measurements. A damping controller design is proposed which greatly improves the dynamic stability of the WT-SCIG and eliminates destructive Hopf bifurcations in weak grids for a wide range of series compensation. This allows for a much larger percentage series compensation than what is usually possible while avoiding instabilities and thereby maximizing power transfer capability.

In addition to analyzing the stability of SCIG-WTs with radial and non-radial interconnections, the stability domains of induction motor loads fed through series compensated feeders have been analyzed. The presence of subcritical Hopf bifurcations resulting in motor stalling and reversal in the rotation of the induction motor has been shown for the first time. The influence of Automatic Voltage Regulator (AVR) parameters on the stability domain of the system with respect to series compensation has been studied.

The influence of AVR gain and time constant along with the time constant of the voltage measurement transducer has been analyzed for the first time. The applications of this would help system planners to implement an appropriate level of series compensation so that safe, secure and reliable operation of the system can be achieved.

CHAPTER 1

INTRODUCTION

Economical growth in the recent years has led to a huge increase in the demand of electric power from the existing power system. New transmission infrastructure maybe needed between generating stations and load centers as existing lines are likely to become overloaded due to the increase in the amount of power transmitted to meet the system demand. With the ever increasing growth in the population, getting the right of way to install new transmission lines is a huge problem in addition to this being a very expensive solution. A low cost alternative would be to increase the existing power transmission capacity of the network by compensating a percentage of reactance of the lines using series capacitors which has been done for decades [1], [2], [3]. The transient stability limit of the system is improved due to reduction of voltage fluctuations and angular swing of the rotor of synchronous machines [4].

In addition to an increasing demand for energy, there is a huge need for clean forms of energy resulting in the deployment of more renewable energy sources from namely wind and solar. The installed capacity of off-shore wind farms is expected to reach 100 GW in the European Union by the year 2030 [5]. Wind turbines are placed at remote locations especially off-shore wind plants resulting in longer cables of high impedance. This greatly limits the power which can be transmitted to the grid due to higher voltage drops and increasing power losses [6]. Due to the constraints of the power transmission network, wind turbines are unable to operate at higher wind speeds resulting in under-utilization of the capacity of the electrical generators. This has been illustrated in Fig. 1.1 for a Type A wind farm connected to the grid through a feeder of high impedance.

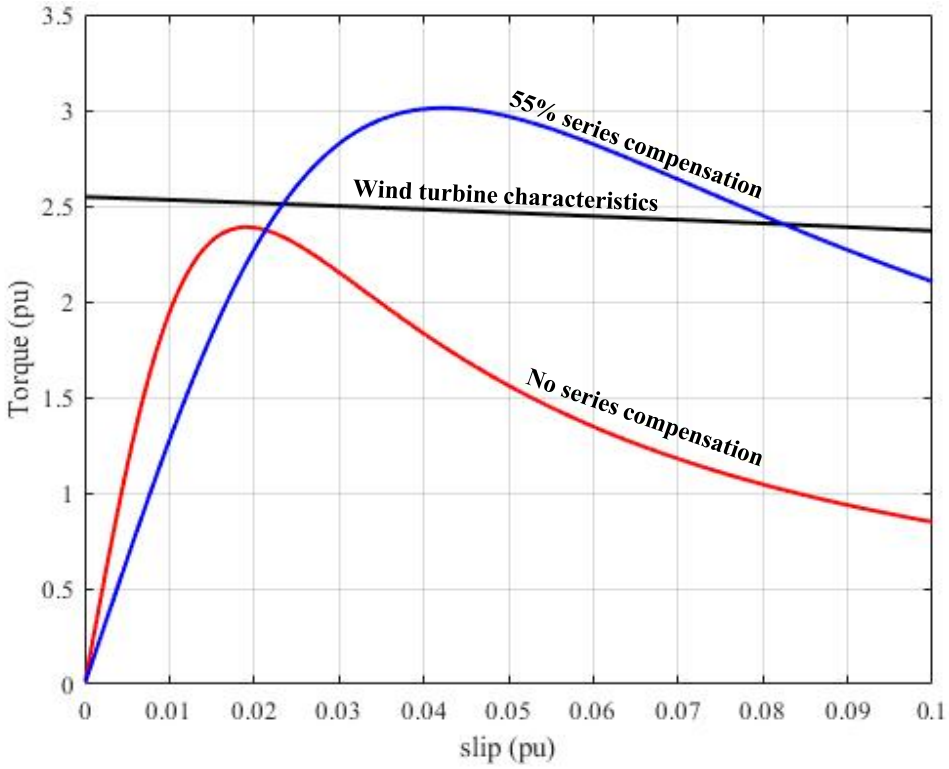

Fig. 1.1: Steady state torque versus slip of SCIG and wind turbine characteristics

In Fig. 1.1, characteristics of the wind turbine along with the characteristics of a Squirrel Cage Induction Generator (SCIG) connected to the grid with and without series capacitor compensation are shown. The wind turbine characteristics show the torque developed by the wind turbine with respect to the slip for a high wind velocity of 17 m/s. It can be seen from the figure that the system without series compensation, operation of the wind turbine at this speed as the wind turbine characteristics do not intersect with the characteristics of the SCIG. However, operation of the system was possible when the system is compensated using series capacitors.

Power systems which are weak and operating under heavily stressed conditions are vulnerable to bifurcations which result in a change in the structural and stability properties of a dynamical system. Bifurcations are classified into local and global types and the existence of both types in power systems have been shown in a number of published works.

Local bifurcations can be detected by analyzing eigenvalues of the Jacobian matrix obtained by linearizing the non-linear dynamical equations of the system. Most common local bifurcations in power systems and their characteristics have been summarized in Table 1.1.

1.1 Motivation

Series capacitors have been utilized to improve the power transfer capability of the existing network for a long time. However, series capacitors result in adverse effects on the stability of power systems when the compensation exceeds a critical value. Instability is due to subsynchronous resonance (SSR) which result in self-excited oscillations ([27], [28], [29]) commonly known as the Induction Generator Effect (IGE) or Torsional Interactions (TI) which may result in shaft fatigues and even shaft failure [30], [31], [32].

Series compensation has known to cause subsynchronous oscillations in wind farms as well [33], [34]. SSR is a well-documented phenomenon in Type - C wind turbines which make use of a Doubly Fed Induction Generators (DFIGs). Detailed modeling and analysis of SSR in DFIG based wind farms has been documented in [35], [36], [37], [38]. Also, mitigation of SSR in DFIG based wind farms has been studied in [39], [40], [41], [42]. However, DFIG based wind turbines may be expensive due to the power electronic converters employed on the rotor side and the grid side. A low cost alternative to DFIG based wind turbines is the Type - A wind turbines based on Squirrel Cage Induction Generators (SCIGs) which are still in use in developing countries. SCIG based wind turbines operate at fixed speed and are usually coupled to the grid. Therefore, these operate in a narrow slip range. SCIGs require reactive power for its operation which is usually supplied by shunt capacitor banks at the stator terminals.

It was shown earlier in Fig. 1.1 that operation at high wind speeds may not be possible if

BIFURCATION	CHARACTERISTICS
Saddle-node bifurcation	Power-flow Jacobian becomes singular Characterized by a zero eigenvalue Results in voltage instability and collapse [7], [8], [9], [10]
Hopf bifurcation	Characterized by a pair of complex eigenvalues crossing over to the right half of the complex plane resulting in a limit cycle [11], [12] Require higher order models to be detected [13], [14], [15] Classified into subcritical or supercritical based on the stability of oscillations [16], [17], [18]
Singularity induced bifurcation	Characteristic of systems modeled using differential and algebraic equations Results in an eigenvalue of the reduced system matrix diverging to infinity [19], [20]
Limit induced bifurcation	Occurs when certain system variables reach their limit resulting in a sudden change in stability Characterized by discrete changes in eigenvalue trajectories when limits are reached [21], [22], [23]
Node-Focus bifurcation	Occurs when a pair of complex eigenvalues transform into 2 real eigenvalues moving in opposite directions or 2 real eigenvalues collide and transform into a pair of complex eigenvalues [24] May not cause a change in the stability but may be a indicate the occurrence of a critical bifurcation like a Hopf bifurcation [23], [25], [26]

Table 1.1: Local bifurcations in power systems and their characteristics

the interconnection to the grid is weak unless series compensation is utilized. However, as a result of series compensation, SCIG based wind turbines may also experience SSR and this has been analyzed in [43], [44], [45] and [46]. In [47], a detailed eigenvalue analysis is presented for a Type-1 wind turbine to study the influences of series compensation and mechanical parameter variations. It has been shown that the SSR due to Induction Generator Effect (IGE) occurs at very high levels of series compensation. However, in this study, IGE is observed for realistic smaller series compensation levels close to 62% for a weak interconnection. In references [43] and [44], the mitigation of SSR is achieved using a supplementary damping controller which was analyzed through time domain simulations. However, the detailed eigenvalue analysis has not been presented.

Traditionally, studies on SSR are performed on systems consisting of a generator or a set of generators feeding power to an infinite bus through a series compensated network by applying bifurcation theory to the IEEE First Benchmark Model ([48], [49], [50], [51]). Bifurcation theory has been applied to study SSR in the IEEE Second Benchmark Model in [52] where the influence on exciter gain on SSR has been analyzed. However, the time constant of the exciter is assumed to be fixed, and its influence on SSR has not been addressed. Global bifurcations have been studied in the IEEE First Benchmark Model due to variations in damping and mechanical power of the synchronous generator ([53], [54]). Few studies have also been performed on induction motor loads fed through a series compensated feeder from a substation which is modeled as an infinite bus ([55], [56], [57]). In these references that have been stated, there is an assumption of a stiff voltage source namely the infinite bus which maybe equivalent to a substation in real time. However, the impact of generator voltage controller parameters on loads supplied from the substation has not been studied so far.

1.2 Objectives and scope of this thesis

This dissertation deals with analyzing stability domains and bifurcations of series compensated power systems with weak interconnections and various network configurations. The main emphasis of this work is to explore how the stability domain of series compensated systems are affected due to varying grid strengths. The following are the objectives and scope of this thesis:

[1] To develop dynamic models of weak power grids of various topologies.

[2] To perform eigenvalue analysis on the linearized system models to identify local bifurcations due to parameter variations which may affect the stability of the system.

[3] To design a voltage regulator for an SVC to enhance the stability domain of the system with respect to series compensation in a radially interconnected weak system.

[4] To present the results of time domain simulations which show the evolution of various system states with respect to time as the system is subject to different types of disturbances and also help identify global bifurcations.

This dissertation is organized as follows: Dynamic models of synchronous and induction machines and wind turbines have been presented in Chapter 2. Chapter 3 deals with the dynamic analysis of an SCIG-WT using fixed shunt capacitors at the stator terminals with a series compensated radial interconnection to the grid. Analysis of a radially interconnected, series compensated system with an SCIG-WT using an SVC at the stator terminals has been presented in Chapter 4. Enhancement of stability domains with respect to series compensation by means of a new damping controller which mitigates Hopf bifurcations causing instability due to SSR has been studied in Chapter 5 for the radially

interconnected, series compensated system with an SCIG-WT and SVC. The dynamic performance of induction motor loads supplied through series compensated networks has been studied in Chapters 6 and 7 where the influence of network and generator control parameters on the stability domain with respect to series compensation is analyzed.

1.3 Publications

A portion of the results presented in this dissertation have been published in 2 journals, the details of which are listed below. Parts of results presented in Chapters 3, 4 and 5 in this dissertation have been published in [2]. Chapter 7 describes the results presented in [1].

[1] J. Devadason, P.S. Moses, M.A.S. Masoum, "Multiparameter Stability Analysis of Systems with Induction Motor Loads, Weak Interconnections and Series Compensation," WSEAS Transactions on Circuits and Systems, vol. 20, pp. 128-138, 2021.

[2] J. Devadason, P.S. Moses, M.A.S. Masoum, "Stability Domain Analysis and Enhancement of Squirrel Cage Induction Generator Wind Turbines in Weak Grids," Energies, MDPI, Open Access Journal, vol. 14(16), pages 1-17, August 2021.

Other results not directly related to this dissertation that have been published during the PhD program can be found in papers listed below:

[1] J. Devadason, P.S. Moses and W. Fei, "Bifurcation Analysis of Weak Electrical Grids Considering Different Load Representations," 2019 IEEE 7th International Conference on Smart Energy Grid Engineering (SEGE), 2019.

[2] J. Devadason and P.S. Moses, "Analysis of Free Acceleration and Steady State Characteristics of Line-Started Induction Motors with Shunt Capacitor Compensation," 2019 IEEE Power & Energy Society General Meeting (PESGM), 2019.

[3] J. Devadason and P.S. Moses, "Small Signal Stability of a Series Compensated Microgrid Operating in Islanded Mode," 2020 Intermountain Engineering, Technology and Computing (IETC), 2020.

[4] D. Glover, J. Devadason and P.S. Moses, "Multi-Solar PV Allocation for Optimal Sizing and Placement on Distribution Feeders," 2020 International Conference on Smart Grids and Energy Systems (SGES), 2020.

[5] H. B. Sambo, J. Devadason and P.S. Moses, "Interactions of Rooftop Solar Photovoltaic Systems with Symmetrical and Unsymmetrical Faults in Distribution Feeders," 2021 IEEE Kansas Power and Energy Conference (KPEC), 2021.

CHAPTER 2

Dynamic Models of Rotating Machines and Wind Turbines

In this chapter, the dynamic models of synchronous machines, induction machines and wind turbines are developed which would be used throughout this thesis to analyze dynamics of various topologies of power system networks with weak interconnections. These mathematical models are derived based on references [58], [59] and [60]. Electromagnetic and electromechanical transients are modeled using differential equations in this dissertation to study stability issues in weak grids when series capacitors are utilized to enhance power transfer and strengthen the interconnection between the generator and the grid (Chapters 3 to 5) or the generator and load center (Chapters 6 and 7).

2.1 Dynamic modeling of synchronous machine

The two-axis model of a synchronous machine is developed in a reference frame fixed on the rotor. The state variables for the synchronous machine are the d and q axis stator currents, emfs induced in the rotor along the field and damper windings, speed and instantaneous position of the rotor. This model is interfaced with the electrical network in Chapter 7 to study interactions of synchronous generators with induction motor loads in a series compensated system.

2.1.1 Modeling of electromagnetic transients

Dynamics of flux linkages in the stator winding along the d and q axis is given by:

$$\frac{d}{dt}\{\psi_{sg}\} = R_a[U]\{I_{sg}\} + \omega[N_1]\{\psi_{sg}\} + \{V_{sg}\} \tag{2.1}$$

where the elements of matrices $[U]$ and $[N_1]$ are given by:

$$[U] = \begin{bmatrix} 1 & 0 \\ 0 & 1 \end{bmatrix} \tag{2.2}$$

$$[N_1] = \begin{bmatrix} 0 & 1 \\ -1 & 0 \end{bmatrix} \tag{2.3}$$

and the elements of the vectors $\{\psi_{sg}\}$, $\{I_{sg}\}$ and $\{V_{sg}\}$ are given by:

$$\{\psi_{sg}\} = [\psi_d \quad \psi_q]^T \tag{2.4}$$

$$\{I_{sg}\} = [I_d \quad I_q]^T \tag{2.5}$$

$$\{V_{sg}\} = [V_d \quad V_q]^T \tag{2.6}$$

The stator flux linkage vector can be expressed as:

$$\{\psi_{sg}\} = [X_{sg1}]\{I_{sg}\} + [N_1]\{E'_{sg}\} \tag{2.7}$$

where the elements of the matrix $[X_{sg1}]$ and vector $\{E'_{sg}\}$ are given by:

$$[X_{sg1}] = \begin{bmatrix} -X'_d & 0 \\ 0 & -X'_q \end{bmatrix} \tag{2.8}$$

$$\{E'_{sg}\} = [E'_d \quad E'_q]^T \tag{2.9}$$

On substituting (2.7) in (2.1), equation 2.10 is obtained which will be used to interface

the synchronous machine with the network using the term $\{V_{sg}\}$.

$$[X_{sg1}]\frac{d}{dt}\{I_{sg}\} + [N_1]\frac{d}{dt}\{E'_{sg}\} = [Z_{sg}]\{I_{sg}\} + \omega[N_1^2]\{E'_{sg}\} + \{V_{sg}\} \tag{2.10}$$

where

$$[Z_{sg}] = R_a[U] + \omega[N_1 X_{sg1}] \tag{2.11}$$

Dynamics of the emfs induced in the rotor windings of the synchronous machine along the d and q axis due to flux linkages in the damper and field windings respectively can be expressed as:

$$[M_r]\frac{d}{dt}\{E'_{sg}\} = -[U]\{E'_{sg}\} + [X_{sg2}]\{I_{sg}\} + [N_2]E_{fd} \tag{2.12}$$

where the elements of the matrices $[M_r]$ and $[X_{sg2}]$ can be written as:

$$[M_r] = \begin{bmatrix} T'_{qo} & 0 \\ 0 & T'_{do} \end{bmatrix} \tag{2.13}$$

$$[X_{sg2}] = \begin{bmatrix} 0 & X_q - X'_q \\ -(X_d - X'_d) & 0 \end{bmatrix} \tag{2.14}$$

2.1.2 Modeling of electromechanical transients

The electromechanical transients of the synchronous machine in generator mode are described by the swing equation given below:

$$2H\frac{d\omega}{dt} = T_m - T_e \tag{2.15}$$

$$\frac{d\delta}{dt} = \omega_s(\omega - 1) \tag{2.16}$$

where the electrical torque T_e of the synchronous machine is given by the following equation:

$$T_e = E'_d I_d + E'_q I_q + (X'_q - X'_d) I_d I_q \tag{2.17}$$

In equation 2.16, the rotor angle δ is measured with respect to a synchronously rotating reference and defines the instantaneous angular position of the rotor.

2.1.3 Linearization of synchronous machine model

In this section, the linearized equations corresponding to the nonlinear dynamic model of the synchronous machine are presented. The linearized state variable around an operating point is prefixed with a Δ and the values of state variables under equilibrium conditions is superscripted by 'o' in this dissertation. The linearized version of equation (2.10) is presented below:

$$[X_{sg1}]\frac{d}{dt}\{\Delta I_{sg}\} + [N_1]\frac{d}{dt}\{\Delta E'_{sg}\} = [Z_{sg}]^o\{\Delta I_{sg}\} + (\omega)^o[N_1^2]\{\Delta E'_{sg}\} + [N_1]\{\psi_{sg}\}^o\Delta\omega + \{\Delta V_{sg}\} \tag{2.18}$$

where $[Z_{sg}]$ is a function of the rotor speed of the generator at equilibrium which is given by $[Z_{sg}]^o = R_a[U] + (\omega)^o[N_1 X_{sg1}]$ and $\{\psi_{sg}\}^o$ is the vector of stator flux linkages of the synchronous generator evaluated using equation (2.7) at the equilibrium point. The linearized expression for the emfs induced in the field and damper windings of the synchronous machine is given by the following equation:

$$[M_r]\frac{d}{dt}\{\Delta E'_{sg}\} = -[U]\{\Delta E'_{sg}\} + [X_{sg2}]\{\Delta I_{sg}\} + [N_2]\Delta E_{fd} \tag{2.19}$$

Equations (2.15) and (2.16) are linearized and are given below:

$$2H\frac{d\Delta\omega}{dt} = \Delta T_m - [T_{sg1}]\Delta\{I_{sg}\} - [T_{sg2}]\Delta\{E'_{sg}\} \tag{2.20}$$

$$\frac{d\Delta\delta}{dt} = (\omega_s)\Delta\omega \tag{2.21}$$

The elements of matrices $[T_{sg1}]$ and $[T_{sg2}]$ are given in equations (2.22) and (2.23) respectively.

$$[T_{sg1}] = [(I_d)^o \quad (I_q)^o] \tag{2.22}$$

$$[T_{sg2}] = [(E'_d)^o + (X'_q - X'_d)(I_q)^o \qquad (E'_q)^o + (X'_q - X'_d)(I_q)^o] \tag{2.23}$$

2.2 Dynamic model of induction machine

The dynamic model of an induction machine operating in motoring and generating modes expressed in a reference frame rotating at synchronous speed is presented in this section. The state variables considered in the induction machine are the d and q axis stator currents, d and q axis rotor currents and slip of the machine. The induction generator model is interfaced with the electrical network in Chapters 3, 4 and 5 to analyze stability of systems with Squirrel Cage Induction Generator - Wind Turbines (SCIG-WTs) in series compensated networks. The induction motor model presented is interfaced with the series compensated network to compute stability domains with respect to series compensation in systems with induction motor loads supplied through weak networks in Chapters 6 and 7.

2.2.1 Modeling of electromagnetic transients

Dynamics of d and q axis stator and rotor currents for the induction machine operating as a motor are expressed using the following differential equations:

$$\frac{X_s}{\omega_s}[U]\frac{d}{dt}\{I_s\} + \frac{X_m}{\omega_s}[U]\frac{d}{dt}\{I_r\} = [Z_{im1}]\{I_s\} + [Z_{im2}]\{I_r\} + \{V_s\} \tag{2.24}$$

$$\frac{X_m}{\omega_s}[U]\frac{d}{dt}\{I_s\} + \frac{X_r}{\omega_s}[U]\frac{d}{dt}\{I_r\} = [Z_{im3}]\{I_s\} + [Z_{im4}]\{I_r\} \tag{2.25}$$

where

$$[Z_{im1}] = -R_s[U] + X_s[N_1] \tag{2.26}$$

$$[Z_{im2}] = X_m[N_1] \tag{2.27}$$

$$[Z_{im3}] = s_m X_m[N_1] \tag{2.28}$$

$$[Z_{im4}] = -R_r[U] + s_m X_r[N_1] \tag{2.29}$$

Similarly, the dynamics of d and q axis currents of an induction machine in generator mode of operation are governed by equations given below:

$$-\frac{X_s}{\omega_s}[U]\frac{d}{dt}\{I_s\} + \frac{X_m}{\omega_s}[U]\frac{d}{dt}\{I_r\} = [Z_{ig1}]\{I_s\} + [Z_{ig2}]\{I_r\} + \{V_s\} \tag{2.30}$$

$$-\frac{X_m}{\omega_s}[U]\frac{d}{dt}\{I_s\} + \frac{X_r}{\omega_s}[U]\frac{d}{dt}\{I_r\} = [Z_{ig3}]\{I_s\} + [Z_{ig4}]\{I_r\} \tag{2.31}$$

where

$$[Z_{ig1}] = R_s[U] - X_s[N_1] \tag{2.32}$$

$$[Z_{ig2}] = X_m[N_1] \tag{2.33}$$

$$[Z_{ig3}] = -s_g X_m [N_1] \tag{2.34}$$

$$[Z_{ig4}] = -R_r [U] + s_g X_r [N_1] \tag{2.35}$$

In all the equations presented above, $X_s = X_{ls} + X_m$ and $X_r = X_{lr} + X_m$ where X_{ls} and X_{lr} are the leakage reactances of the stator and rotor windings respectively and X_m is the magnetizing reactance of the induction motor. The matrices $[U]$ and $[N_1]$ are the same as defined in equations (2.2) and (2.3). In equations (2.24), (2.25), (2.30) and (2.31), $\{I_s\} = [I_{ds} \quad I_{qs}]^T$, $\{I_r\} = [I_{dr} \quad I_{qr}]^T$ and $\{V_s\} = [V_{ds} \quad V_{qs}]^T$. Note that in equations (2.25) and (2.31), the matrices $[Z_{im3}]$, $[Z_{im4}]$, $[Z_{ig3}]$ and $[Z_{ig4}]$ are a function of the slip of the machine. Since these matrices are multiplied by vectors containing stator and rotor currents which are also state variables, the resulting equations are nonlinear.

2.2.2 Modeling of electromechanical transients

The rotor speed of an induction motor is determined using the swing equation below:

$$2H_{im}\frac{ds_m}{dt} = T_m - T_e \tag{2.36}$$

where T_m is the mechanical torque demanded from the induction motor and T_e is the electrical torque output of the motor and is given by equation:

$$T_e = X_m(I_{qs}I_{dr} - I_{ds}I_{qr}) \tag{2.37}$$

Electromechanical dynamics of an induction generator are described using the swing equation as shown below:

$$2H_{ig}\frac{ds_g}{dt} = T_e - T_m \tag{2.38}$$

where T_m is the mechanical torque input to the induction generator. In this dissertation, the mechanical torque of the induction generator is supplied by the wind and T_e is the same as that of equation (2.37).

2.2.3 Linearization of induction machine model

The linearized equations corresponding to the electromagnetic transients of the induction motor are shown below:

$$\frac{X_s}{\omega_s}[U]\frac{d}{dt}\{\Delta I_s\} + \frac{X_m}{\omega_s}[U]\frac{d}{dt}\{\Delta I_r\} = [Z_{im1}]\{\Delta I_s\} + [Z_{im2}]\{\Delta I_r\} + \{\Delta V_s\} \tag{2.39}$$

$$\frac{X_m}{\omega_s}[U]\frac{d}{dt}\{\Delta I_s\} + \frac{X_r}{\omega_s}[U]\frac{d}{dt}\{\Delta I_r\} = [Z_{im3}]^o\{\Delta I_s\} + [Z_{im4}]^o\{\Delta I_r\} + [N_1]\{\lambda_r\}^o\Delta s_m \tag{2.40}$$

where

$$[Z_{im3}]^o = (s_m)^o X_m[N_1] \tag{2.41}$$

$$[Z_{im4}]^o = -R_r[U] + (s_m)^o X_r[N_1] \tag{2.42}$$

$$\{\lambda_r\}^o = X_m[U]\{I_s\}^o + X_r[U]\{I_r\}^o \tag{2.43}$$

Similarly, the linearized expressions corresponding to the electromagnetic transients of an induction generator can be written as:

$$-\frac{X_s}{\omega_s}[U]\frac{d}{dt}\{\Delta I_s\} + \frac{X_m}{\omega_s}[U]\frac{d}{dt}\{\Delta I_r\} = [Z_{ig1}]\{\Delta I_s\} + [Z_{ig2}]\{\Delta I_r\} + \{\Delta V_s\} \tag{2.44}$$

$$-\frac{X_m}{\omega_s}[U]\frac{d}{dt}\{\Delta I_s\} + \frac{X_r}{\omega_s}[U]\frac{d}{dt}\{\Delta I_r\} = [Z_{ig3}]\{\Delta I_s\} + [Z_{ig4}]\{\Delta I_r\} + [N_1]\{\lambda_r\}^o\Delta s_g \tag{2.45}$$

where

$$[Z_{ig3}]^o = -(s_g)^o X_m[N_1] \tag{2.46}$$

$$[Z_{ig4}]^o = -R_r[U] + (s_g)^o X_r[N_1] \tag{2.47}$$

$$\{\lambda_r\}^o = -X_m[U]\{I_s\}^o + X_r[U]\{I_r\}^o \tag{2.48}$$

Equations (2.36) and (2.38) which describe the electromechanical dynamics of the induction machine in motoring and generating mode are linearized and the corresponding expressions are given below:

$$2H_{im}\frac{d\Delta s_m}{dt} = \Delta T_m - [T_{im1}]\Delta\{I_s\} - [T_{im2}]\Delta\{I_r\} \tag{2.49}$$

$$2H_{ig}\frac{d\Delta s_g}{dt} = [T_{im1}]\Delta\{I_s\} + [T_{im2}]\Delta\{I_r\} - \Delta T_m \tag{2.50}$$

where

$$[T_{im1}] = X_m[-(I_{qr})^o \quad (I_{dr})^o] \tag{2.51}$$

$$[T_{im2}] = X_m[(I_{qs})^o \quad -(I_{ds})^o] \tag{2.52}$$

2.3 Modeling of wind turbine

In this section, the expression for the mechanical power input (P_w) to the generator from the wind turbine is presented as a function of slip of the generator. Figure 2.1 shows a wind turbine coupled to an electrical generator through a gear box which is used to translate the speed of rotation of the wind turbine blades to a value of rotor speed to achieve a suitable steady state operating point based on the electrical characteristics of the generator. The mechanical power developed by the wind turbine is a function of air density, swept area of the turbine blades and the power coefficient and is given by:

$$P_w = (1/2)\rho C_p(\lambda) A V_w^3 \tag{2.53}$$

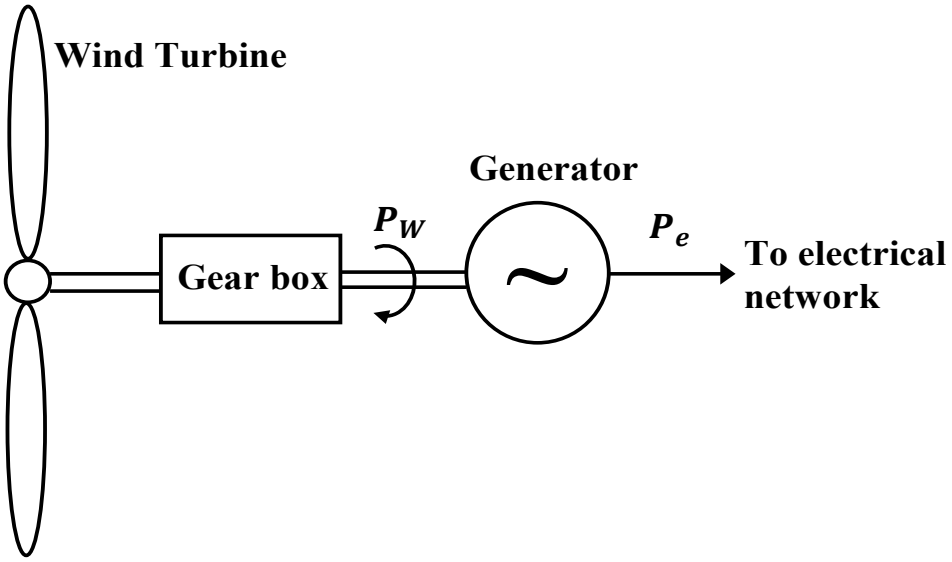

Fig. 2.1: Wind Turbine

$$T_w = P_w/\omega_r \tag{2.54}$$

where C_p is the power coefficient given by equation (2.55), A is the radius of swept area by the wind turbine blades and ρ is the air density.

$$C_p(\lambda) = c_1(c_2/\lambda_i - c_3\theta - c_4\theta^{c_5} - c_6)e^{-c_7/\lambda_i} \tag{2.55}$$

where

$$\frac{1}{\lambda_i} = \frac{1}{\lambda + c_8\theta} - \frac{c_9}{\theta^3 + 1} \tag{2.56}$$

where $\lambda = \omega_r R/V_w$. R is the rotor radius and λ is called 'Tip Speed Ratio' (TSR). If N_s is the synchronous speed in rpm, n_s is the speed of the wind turbine in rpm which is given by $n_s = \frac{N_s}{G_r}$ where G_r is the gear box ratio. The expression for TSR in terms of N_s and slip s_g as:

$$\lambda = \frac{2\pi R N_s}{60 V_w}(1 - s_g) \tag{2.57}$$

2.3.1 Linearization of wind turbine model

In this section, the linearized mathematical model of the wind turbine is presented. Before deriving the linearized expressions, the equations for the mechanical power and torque developed by the wind turbine in per unit are presented below:

$$P_w = (1/2)\rho C_p(\lambda) A V_w^3 * (10^{-6}/S_b) \tag{2.58}$$

$$T_w = \frac{P_w}{\omega_r} = \frac{P_w}{1 - s_g} \tag{2.59}$$

In equation (2.58), the power coefficient C_p is a function of λ which is a function of the generator slip and this is obvious from equation (2.57). Hence, P_w can be written as $P_w = K_o C_p(\lambda)$ where $K_o = (1/2)\rho A V_w^3 * (10^{-6}/S_b)$ and S_b being the base MVA of the system. The linearized expression for T_w can now be expressed as:

$$\Delta T_w = \frac{K_o}{1 - (s_g)^o}\Delta C_p + \frac{K_o C_p(\lambda^o)}{(1 - (s_g)^o)^2}\Delta s_g \tag{2.60}$$

The expression for TSR at equilibrium can be written as $\lambda^o = L_o(1 - (s_g)^o)$ where $L_o = \frac{2\pi R N_s}{60 V_w}$. The expression for $C_p(\lambda)$ can be written as $C_p = c_1 M(\lambda) N(\lambda)$ where

$$M(\lambda) = c_2/\lambda_i - c_3\theta - c_4\theta^{c_5} - c_6 \tag{2.61}$$

$$N(\lambda) = e^{-c_7/\lambda_i} \tag{2.62}$$

The linearized expression for C_p is now written as

$$\Delta C_p = C_{w1} C_{w2} \Delta s_g \tag{2.63}$$

where

$$C_{w1} = \frac{c_1 N(\lambda^o) L_o}{(\lambda^o + c_8\theta)^2} \tag{2.64}$$

$$C_{w2} = c_2 - c_7 M(\lambda^o) \tag{2.65}$$

Hence, the linearized expression for the torque developed by the wind turbine can be finally written as

$$\Delta T_w = \left[\frac{K_o C_{w1} C_{w2}}{1 - (s_g)^o} + \frac{K_o C_p(\lambda^o)}{(1 - (s_g)^o)^2} \right] \Delta s_g \tag{2.66}$$

2.4 Conclusion

In this chapter, nonlinear dynamic models of a synchronous generator, induction machine operating as a motor and as a generator and a wind turbine are presented. The synchronous machine model is developed in a reference frame fixed on the rotor of the machine and the induction machine model is developed in a reference frame rotating at synchronous speed. Linearized models of these components have been presented in this chapter as well. These nonlinear dynamic models will be interfaced with networks of different configurations in the forthcoming chapters to perform time domain simulations to understand dynamic behavior of systems subject to various disturbances. The linearized models developed in this chapter will be interfaced with linearized models of various electrical networks to compute the Jacobian matrix which will be used to analyze local bifurcations affecting the stability of the system.

CHAPTER 3

Dynamic analysis of Squirrel Cage Induction Generator - Wind Turbine with a Radial Interconnection to the Grid

In this chapter, the stability of SCIG-WTs connected to the grid through a radially connected series compensated line is investigated through eigenvalue analysis and time domain simulations. Previous research in this area claims that instability in the system due to the induction-generator effect (IGE) of SSR happens only at very high levels of series compensation (80% compensation) [61], [47]. Although this claim might be true in some cases, it may not be true in cases where the system is weak, such as interconnections involving long lines or feeders of high impedance. Eigenvalue analysis are presented for the linearized system model to analyze bifurcations leading to instabilities in the system. The influence of generator slip as well as the strength of the grid reflected as a function of the X/R ratio of the network has been considered while investigating stability domains with respect to series compensation. Time domain simulation of the non-linear dynamic model of the system has been performed to observe system behavior when subjected to a momentary disturbance in the grid voltage.

3.1 Mathematical modeling of network

The single line diagram of the system under study is shown in Fig.3.1. The terminal of the generator is connected to the grid through a series compensated line to enhance power transfer capability of the network. Reactive power support for the generator is supplied through shunt capacitors connected at the stator terminals. The dynamics of the fixed shunt capacitor connected at the stator terminals for reactive power support is

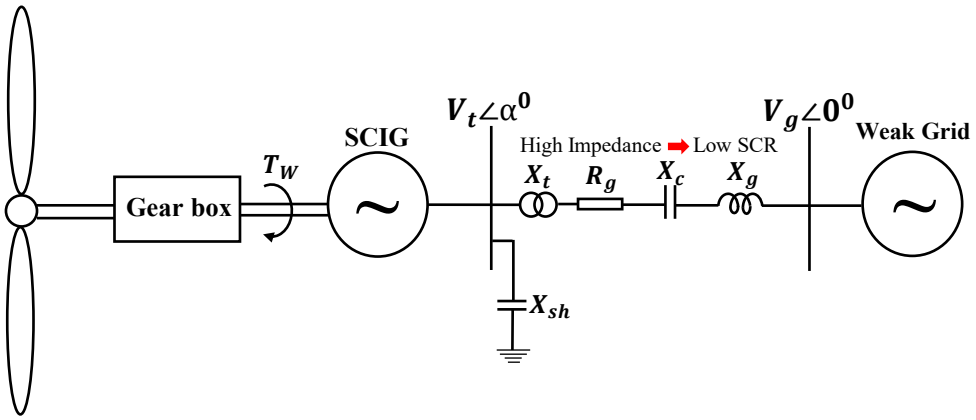

Fig. 3.1: Single line diagram of modified IEEE First Benchmark Model

described by the equation shown below:

$$\frac{1}{\omega_s}[U]\frac{d}{dt}\{V_s\} = [N_1]V_s + [Z_{sh}]\{I_s - I_n\} \tag{3.1}$$

where

$$[U] = \begin{bmatrix} 1 & 0 \\ 0 & 1 \end{bmatrix} \tag{3.2}$$

$$[N_1] = \begin{bmatrix} 0 & 1 \\ -1 & 0 \end{bmatrix} \tag{3.3}$$

$$[Z_{sh}] = X_{sh}[U] \tag{3.4}$$

and the elements of the vectors $\{I_s\}$, $\{I_n\}$ and $\{V_s\}$ are given by:

$$\{I_s\} = [I_{ds} \quad I_{qs}]^T \tag{3.5}$$

$$\{I_n\} = [I_{dn} \quad I_{qn}]^T \tag{3.6}$$

$$\{V_s\} = [V_{ds} \quad V_{qs}]^T \tag{3.7}$$

In the above equations, I_{dn} and I_{qn} are d and q components of the network currents. The dynamics of the voltage across the series capacitor along the d and q axis is expressed using the following differential equation:

$$\frac{1}{\omega_s}[U]p\{V_c\} = [N_1]\{V_c\} + [Z_{se}]\{I_n\} \tag{3.8}$$

where

$$[Z_{se}] = X_c[U] \tag{3.9}$$

and $\{V_c\} = [V_{dc} \quad V_{qc}]^T$.

The differential equation which describes the dynamics of the d and q components of the network currents is given below:

$$\frac{X_n}{\omega_s}[U]p\{I_n\} = [Z_{nw}]\{I_n\} - \{V_c\} - \{V_g\} + \{V_s\} \tag{3.10}$$

where $X_n = X_t + X_g$ and $\{V_g\} = [V_{dg} \quad V_{qg}]^T$ where V_{dg} and V_{qg} are the d and q components of the grid voltage. The elements of matrix $[Z_{nw}]$ are given below:

$$[Z_{nw}] = \begin{bmatrix} R_n & -X_n \\ X_n & R_n \end{bmatrix} \tag{3.11}$$

In this study, the resistance of the step-up transformer is assumed to be negligible, i.e $R_t = 0$ pu. Hence, $R_n = R_g$.

3.2 Linearization of mathematical model

The dynamic equations of the network presented in Section 3.1 are linearized and presented below:

$$\frac{1}{\omega_s}[U]p\{\Delta V_s\} = [N_1]\{\Delta V_s\} + [Z_{sh}]\{\Delta I_s - \Delta I_n\} \tag{3.12}$$

$$\frac{1}{\omega_s}[U]p\{\Delta V_c\} = [N_1]\{\Delta V_c\} + [Z_{se}]\{\Delta I_n\} \tag{3.13}$$

$$\frac{X_n}{\omega_s}[U]p\{\Delta I_n\} = [Z_{nw}]\{\Delta I_n\} - \{\Delta V_c\} - \{\Delta V_g\} + \{\Delta V_s\} \tag{3.14}$$

In equation (3.14), $\{\Delta V_{dqg}\} = 0$ since the voltage of the grid is assumed to be fixed under equilibrium conditions.

3.3 Eigenvalue analysis

The linearized mathematical model of the system consists of equations (2.44), (2.45), (2.50), (3.12), (3.13) and (3.14), . The complete list of linearized state variables of the system is given below:

$$\Delta X = \{\Delta I_{ds}, \Delta I_{qs}, \Delta I_{dr}, \Delta I_{qr}, \Delta I_{dn}, \Delta I_{qn}, \Delta V_{ds}, \Delta V_{qs}, \Delta V_{dc}, \Delta V_{qc}, \Delta s_g\}^T \tag{3.15}$$

These equations are cast in state space form $[M]\Delta\dot{X} = [A]\Delta X$. The Jacobian matrix of the system is obtained using $[J] = [M]^{-1}[A]$. Eigenvalues of the Jacobian matrix give very useful information regarding stability of the system and computing participation factors using the left and right eigenvectors reveal the contribution of individual system states. Presence of local bifurcations in the system could be detected by analyzing the eigenvalues of the system as certain parameters are varied.

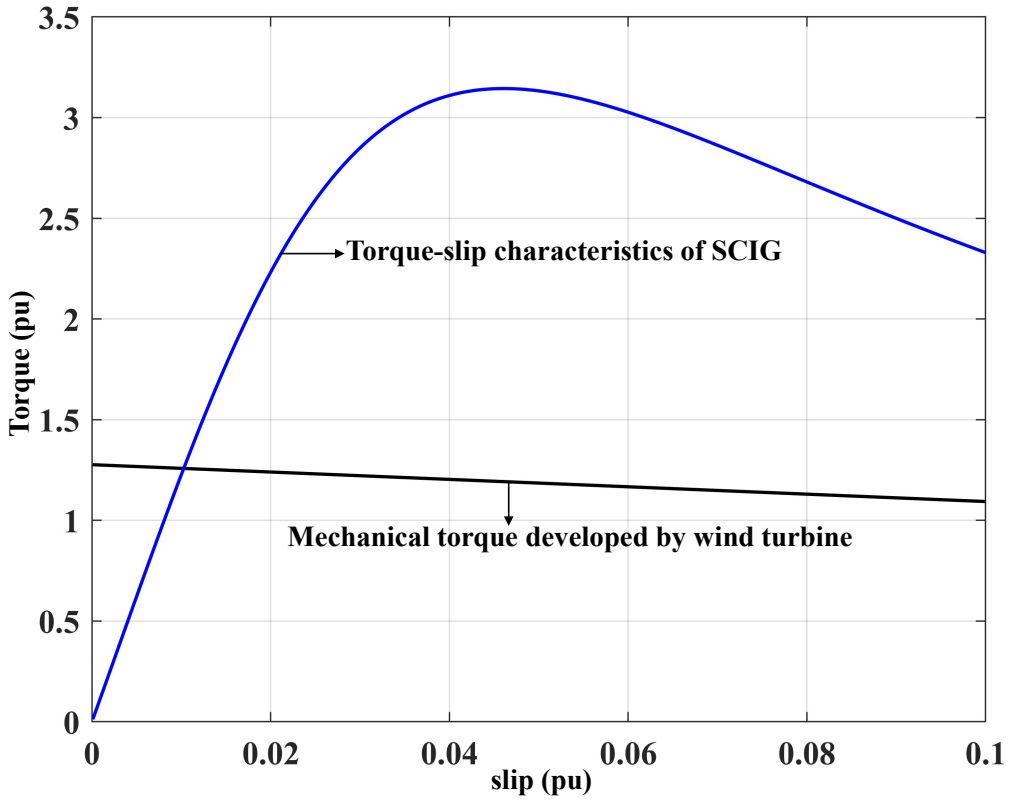

Fig. 3.2: Steady state characteristics of SCIG and wind turbine for 60% series compensation

Eigenvalues of the system are computed for a wind speed $V_w = 13.5$ m/s which corresponds to a rotor slip $s_g = -0.010724$ pu obtained from the intersection of the steady state characteristics of the induction generator and the wind turbine which is shown in Fig. 3.2. In Table 3.1, eigenvalues of the system are listed for a series compensation ($K_c = X_c/X_n$) of 60% when the X/R ratio (X_n/R_n) of the network is assumed to be 30. There are 5 oscillatory modes (λ_1 to λ_5) and 1 non-oscillatory mode (λ_6).

Among the oscillatory modes, λ_1, λ_2 and λ_3 have frequencies greater than 60 Hz and are designated as the supersynchronous modes which are found to have negative real parts and hence, are stable. Modes λ_4 and λ_5 have frequency less than 60 Hz which are the subsynchronous modes among which λ_4 has a positive real part making it unstable. This mode is a result of the participation of stator and rotor currents of the SCIG, line currents and the series capacitor voltage which shows that the system is unstable due to SSR.

Table 3.1: Eigenvalues of SCIG-WT for 60% series compensation and $s_g = 1\%$.

$\boldsymbol{\lambda_i}$	$\boldsymbol{-\sigma \pm j\omega}$	**Participating States**
λ_1	$-27.323 \pm j1466.5$	I_{ds},I_{qs},I_{dr},I_{qr},I_{dn},I_{qn},V_{ds},V_{qs},V_{dc},V_{qc}
λ_2	$-38.79 \pm j712.55$	I_{ds},I_{qs},I_{dr},I_{qr},I_{dn},I_{qn},V_{ds},V_{qs}
λ_3	$-12.548 \pm j627$	I_{ds},I_{qs},I_{dr},I_{qr},I_{dn},I_{qn},V_{ds},V_{qs},V_{dc},V_{qc}
λ_4	$0.584 \pm j125.45$	I_{ds},I_{qs},I_{dr},I_{qr},I_{dn},I_{qn},V_{dc},V_{qc}
λ_5	$-9.4524 \pm j21.922$	I_{ds},I_{qs},I_{dr},I_{qr},I_{dn},I_{qn},V_{ds},V_{qs},V_{qc},s_g
λ_6	-15.979	I_{ds},I_{qs},I_{dr},I_{qr},s_g

3.3.1 Eigenvalues for different generator slips

The eigenvalues of the system under study when the degree of compensation K_c is varied from 0.005 to 0.98 are calculated and plotted on the complex plane for 2 different generator slips $s_g = 1\%$ and $s_g = 3\%$ which correspond to low and high values wind speeds respectively as shown in Fig. 3.3. The X/R ratio of the network is assumed to be 30. The variations in torque input from the wind is assumed to be slow and hence is neglected in this analysis ($\Delta T_w \approx 0$). This greatly simplifies the computations as the operating slip s_g does not have to be calculated for each level of series compensation.

It was observed from Fig. 3.3 that the supersynchronous modes are all stable for the entire range of series compensation considered for s_g of 1% and 3%. The damping of the subsynchronous mode decreases with an increase in K_c and when K_c is between 0.575 and 0.58, a Hopf bifurcation occurs due to subsynchronous resonance when s_g was 1%. At a higher slip s_g of 3%, the system is unstable for a compensation level K_c from 0.5% due to the presence of a real eigenvalue on the right half of the complex plane resulting in the system being unstable. The equilibrium is called a 'saddle-focus' characterized by 3 leading eigenvalues given by $\lambda_{1,2} = -8.8894 \pm j16.957$ and $\lambda_3 = 3.5009$. Participation factors for these leading eigenvalues are presented in Table 3.3.

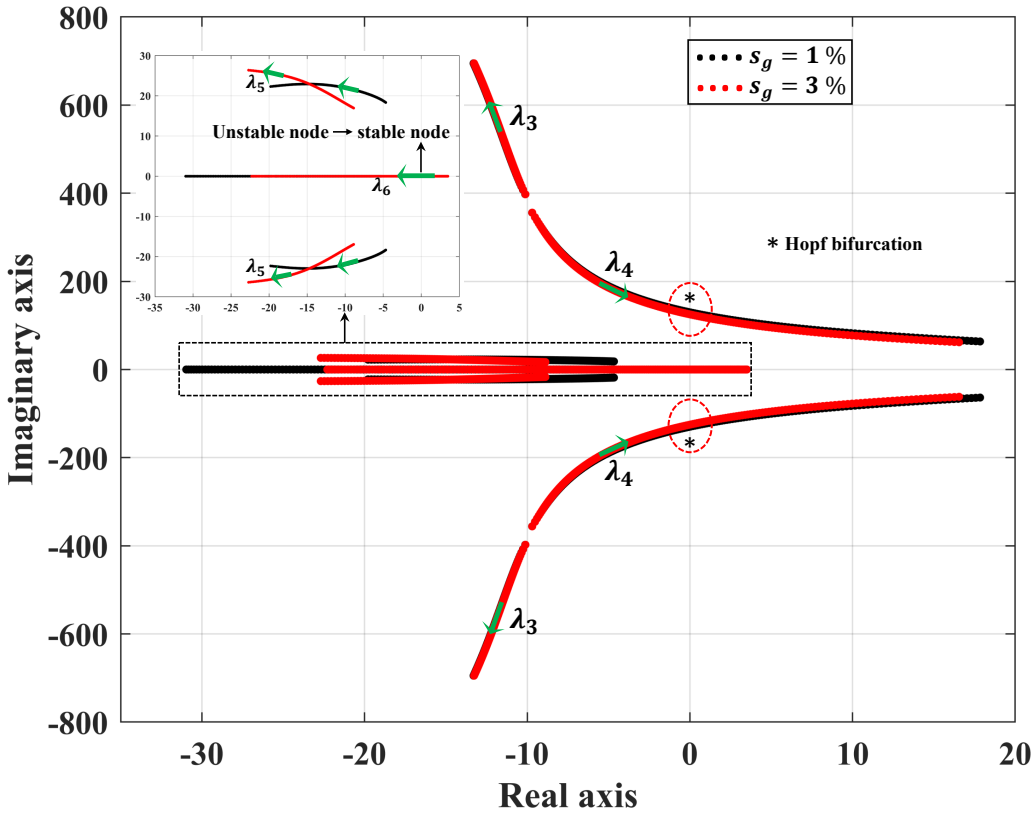

Fig. 3.3: Eigenvalues for low and high generator slips

Table 3.2: Participation factors of critical eigenvalue pair for $s_g = 1\%$ and 60% series compensation.

$\lambda = -\sigma \pm j\omega$	I_{ds}	I_{qs}	I_{dr}	I_{qr}	I_d	I_q	V_{dc}	V_{qc}
$0.584 \pm j125.38$	0.246	0.24	0.243	0.237	0.007	0.007	0.009	0.009

Table 3.3: Participation factors of leading eigenvalues for $s_g = 3\%$ at a compensation of 0.5%.

$\lambda = -\sigma \pm j\omega$	I_{ds}	I_{qs}	I_{qs}	I_{qs}	s_g
3.5009	0.103	0.307	0.119	0.376	0.093
$-8.8894 \pm j16.957$	0.250	0.181	0.310	0.223	0.033

As the compensation increased, the unstable eigenvalue moves to the left half of the complex plane and when $K_c > 31.5\%$, λ_{cr} mode crosses over from the right half to the left half of the complex plane resulting in a bifurcation making the system stable. The system remains stable as the compensation level increases to 60% beyond which a Hopf

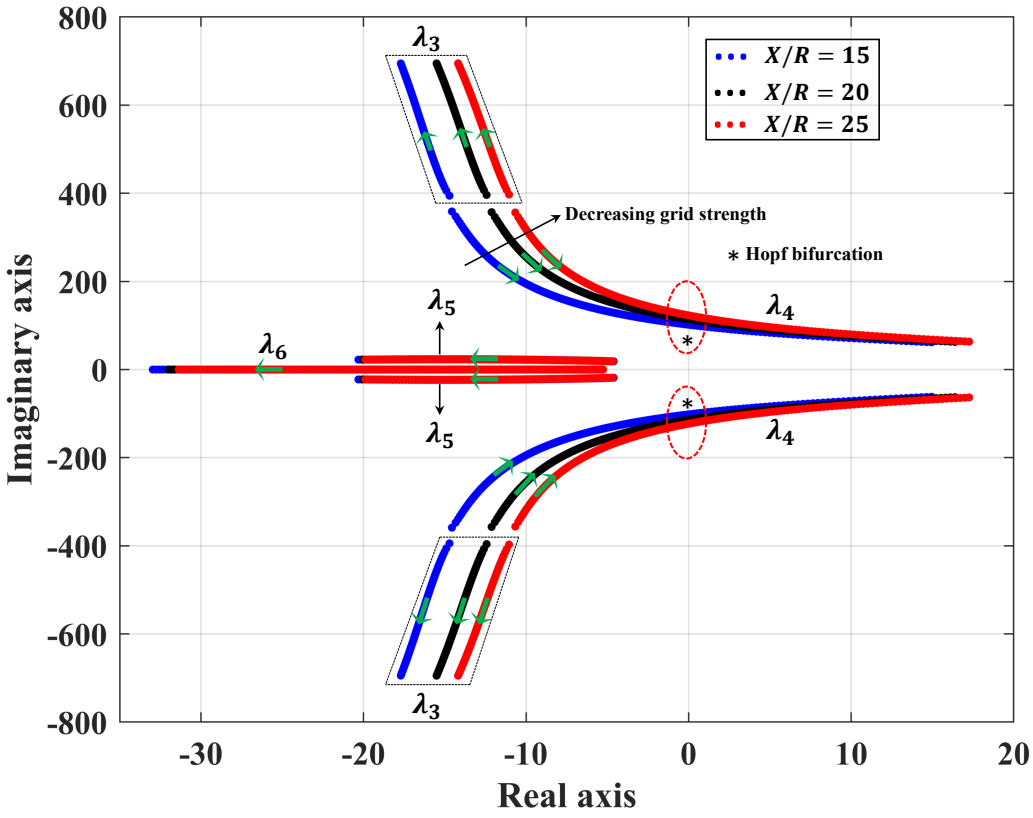

Fig. 3.4: Eigenvalues for different grid strengths

Table 3.4: Critical eigenvalues for different X/R ratios

X/R ratio	K_{cr}	$\lambda_{cr} = -\sigma \pm j\omega$	Participating states
15	72%	$0.146 \pm j101.19$	I_{ds},I_{qs},I_{dr},I_{qr},I_{dn},I_{qn},V_{dc},V_{qc}
20	65.5%	$0.009 \pm j114.05$	
25	61.5%	$0.122 \pm j122.25$	

bifurcation results making the system unstable due to subsynchronous resonance. The critical series compensation level at which instability due to Hopf bifurcation is observed is slightly larger for a higher operating slip of the induction generator.

3.3.2 Eigenvalues for different grid strengths

Increasing the X/R ratio of the line results in an increase in the line impedance for a given value of line resistance. This decreases the Short Circuit Ratio (SCR) at the point of

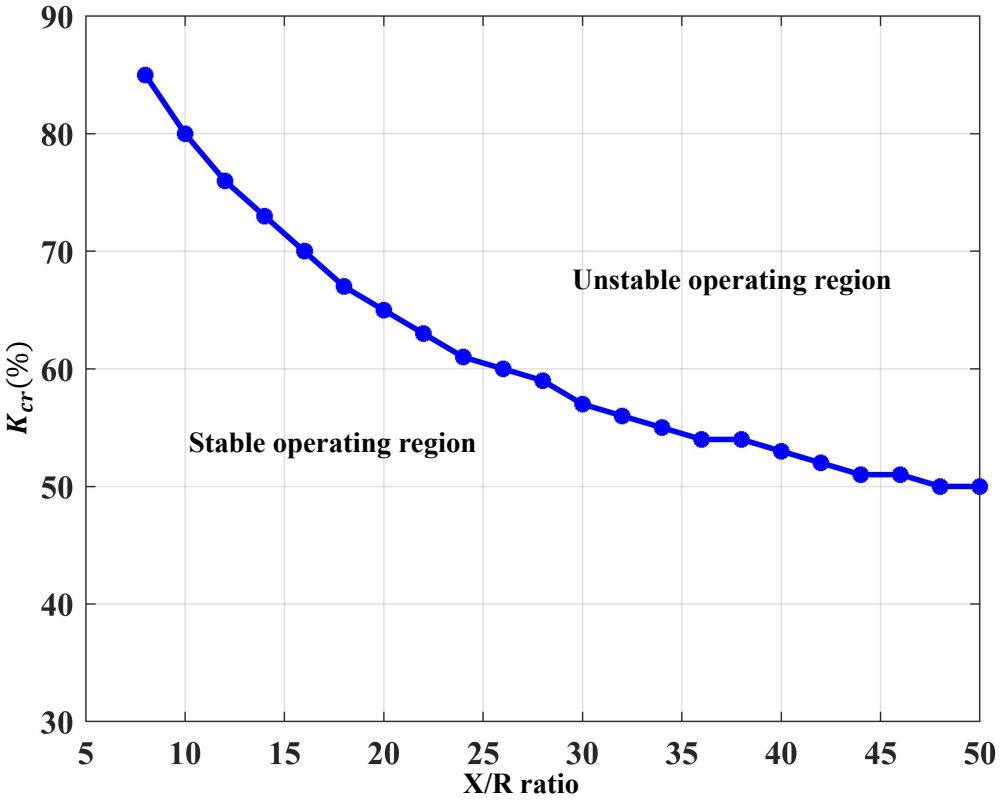

Fig. 3.5: Stability boundary with respect to X/R ratio of network.

interconnection (POI) as the Thevenin impedance of the system up to the POI increases as the impedance of the line increases which results in a weaker interconnection to the grid. The eigenvalues of the system for a generator slip of 1% are calculated for X/R ratios of 15, 20 and 25 and are plotted in Fig. 3.4. Supersynchronous modes and the non-oscillatory mode is observed to be stable for the entire range of series compensation considered but the subsynchronous mode becomes less damped as the series compensation level increases. Subsynchronous resonance occurs at compensation levels of 72%, 65.5% and 61.5% for X/R ratios of 15, 20 and 25 respectively which shows that as the grid becomes weaker, there is a higher possibility of SSR at lower values of series compensation. This is further evident in Fig. 3.5, where the critical value of series compensation is plotted as a function of X/R ratio of the network, which gives the stability boundary with respect to series compensation.

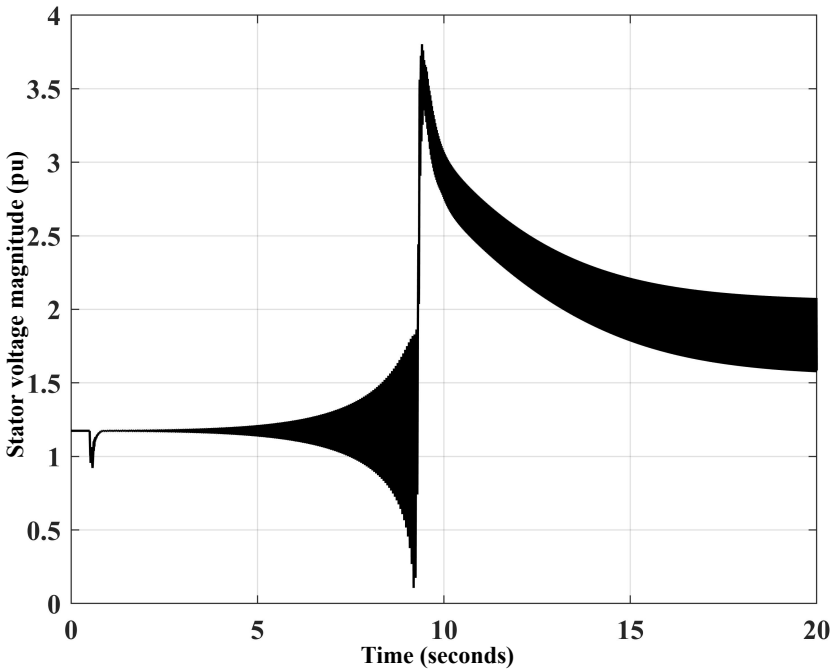

Fig. 3.6: Stator voltage response to a disturbance in grid voltage

3.4 Time domain simulations

In this section, the results of time domain simulations performed on the system under study are presented. The non-linear dynamic model of the system comprised of equations (2.30), (2.31), (2.38), (3.1), (3.8) and (3.10) is simulated using SIMULINK and the traces of various system state variables are observed. The series compensation level considered is 60% which is a practical value of series compensation level for an X/R ratio of 30.

A disturbance in the grid voltage is applied at 0.5 s when the voltage magnitude of the grid decreases from 1 pu to 0.8 pu and is restored to 1 pu again at 0.6 s. In a realistic system, this may be equivalent to a three phase fault occurring at a bus causing a reduction in bus voltages and the fault being cleared in 6 cycles (0.1 s) resulting in a restoration of the bus voltages. The stator voltage at the terminals of the SCIG and the line current magnitudes are shown in Figs. 3.6 and 3.7 respectively. The SCIG initially operates with a terminal voltage of 1.18 pu under equilibrium conditions. When the reduction in the

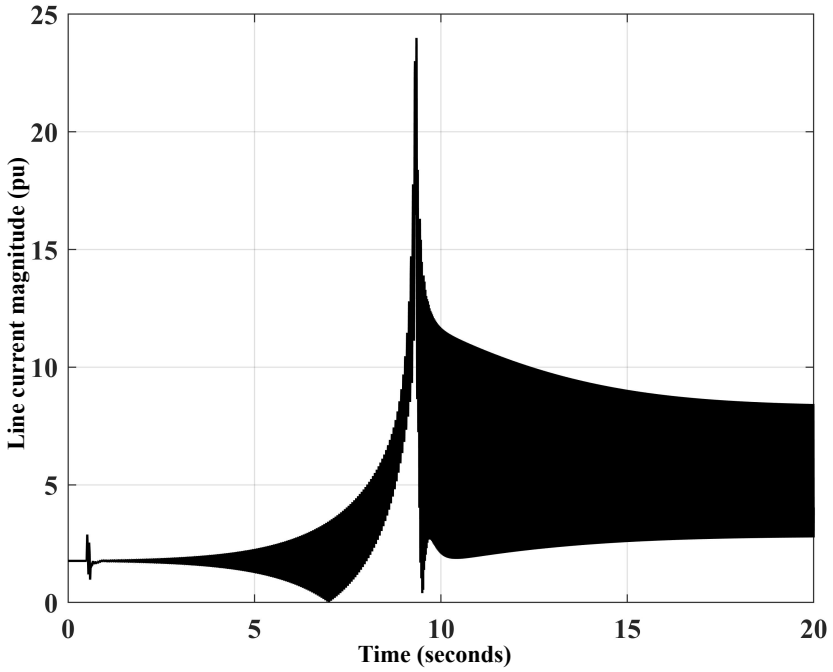

Fig. 3.7: Line current response to a disturbance in grid voltage

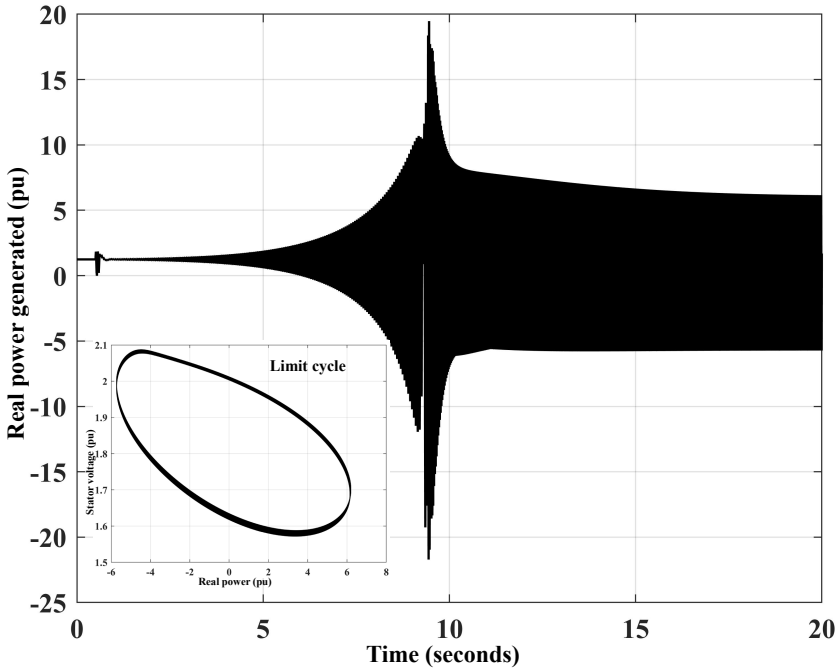

Fig. 3.8: Real power response to a disturbance in grid voltage

grid voltage takes place, there is a momentary decrease in the terminal voltage of the SCIG. Beyond 0.8 s, the voltage starts increasing up to 9.44 s. There is a significant spike

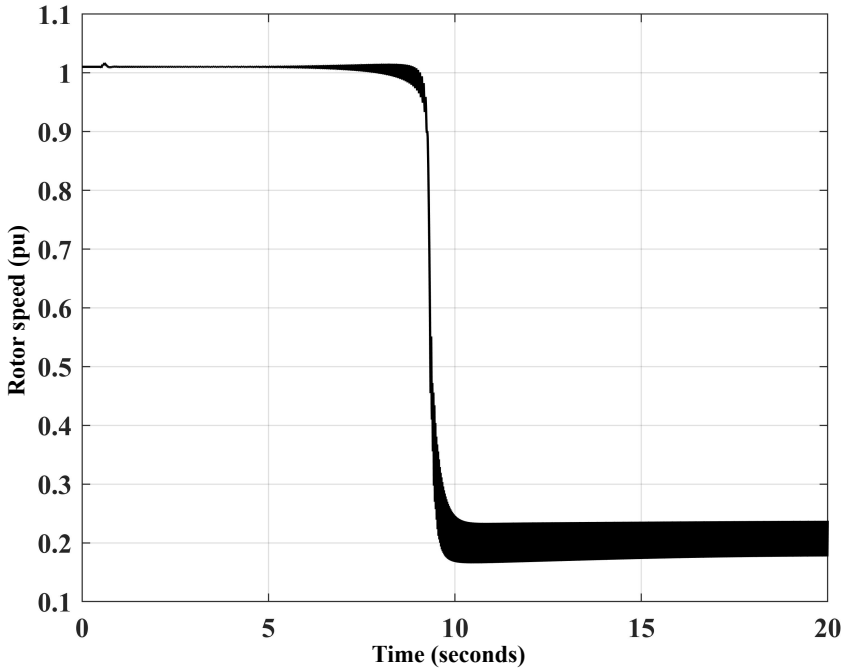

Fig. 3.9: Rotor speed response to a disturbance in grid voltage

in the voltage at 9.57 s where the magnitude almost becomes 3.8 pu and beyond this, the voltage starts decreasing. The voltage finally settles into an oscillatory state where the magnitude of voltage at the SCIG terminals oscillates between 1.5 and 2.1 pu.

The traces of real power generated by the SCIG and the speed of the induction generator are shown in Figs. 3.8 and 3.9 respectively. The responses of stator voltage and real power generated indicates that the system is unstable due to a Hopf bifurcation resulting from SSR. The rotor speed of the induction generator shows oscillations around the steady state value initially between 0.5 and 9.4 s. After this, the rotor speed drops rapidly causing the generator to stall. The reason for this is that there are voltages and currents induced at subsynchronous frequency which increase in magnitude as a result of self excitation due to SSR. This produces a magnetic field rotating at subsynchronous speed in the air gap which increases in strength beyond 9.4 s, as the magnitude of currents and voltages increase rapidly. Hence, the magnetic field induced by the subsynchronous currents dominates the main field and the rotor speed of the induction machine attempts

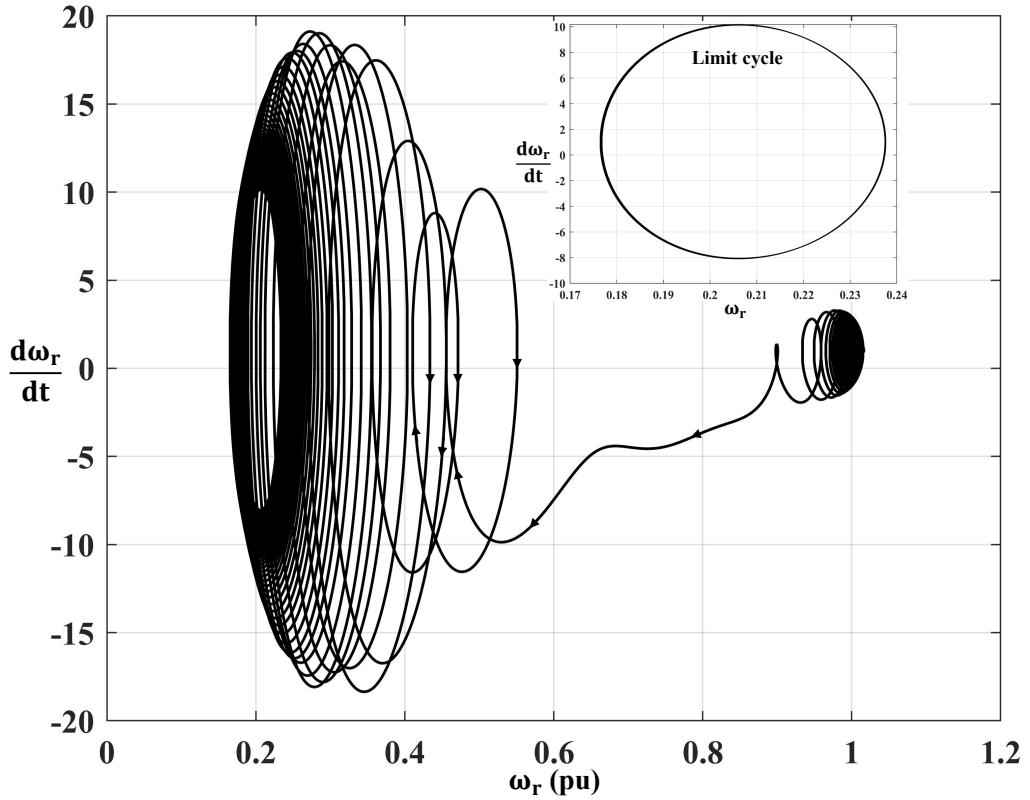

Fig. 3.10: Phase plane trajectory of rotor speed in response to a grid voltage disturbance

to catch up with the speed of the magnetic field rotating at subsynchronous speed as a result of which the speed starts decreasing beyond 9.4 s.

The phase-plane trajectory of the generator speed along with the limit cycle is shown in Fig. 3.10. The system appears to have an oscillatory response of fixed amplitude beyond 18 s as a result of a limit cycle generated due to the Hopf bifurcation. The generator speed shows oscillations between 0.17 pu and 0.24 pu which is far away from the equilibrium speed of 1.0103 pu. Hence, the nature of Hopf bifurcation can be concluded to be subcritical as the trajectory has diverged away from the equilibrium value significantly.

3.5 Conclusion

In this chapter, the dynamic analysis of an SCIG-WT supplying power to the grid through a weak interconnection has been presented. Eigenvalue analysis and participation factors reveal the main reason for instability in the system is the Hopf bifurcation which occurs due to subsynchronous resonance for smaller values of generator slips as the series compensation exceeds a certain critical percentage. However, for higher generator slip values, there is a possibility of non-oscillatory instability for small values of series compensation which is the characteristic of a saddle-focus equilibrium point. Series compensation has to be above a lower threshold value for the system to operate in a stable manner, however, above a certain upper limit, the system exhibits SSR causing the system to become unstable. From the time domain simulation results, it can be concluded that the nature of the Hopf bifurcation due to SSR is subcritical as the limit cycle generated is far away from the equilibrium point.

CHAPTER 4

Stability Domain Enhancement in a Radially Interconnected System with Squirrel Cage Induction Generator - Wind Turbines

In this chapter, stability domain enhancement in the modified IEEE First Benchmark Models (FBM) with a Squirrel Cage Induction Generator - Wind Turbine (SCIG-WT) has been explored. A Static Var Compensator (SVC) has been used in place of a fixed shunt capacitor to provide the needed reactive power for excitation at the terminals of the SCIG. The upper limit of percentage series compensation in practical systems is fixed at a value around 50% in order to avoid instabilities due to SSR. However, using an SVC with a Subsynchronous Damping Controller (SSDC) at the terminals of the SCIG in the place of a fixed shunt capacitor bank, the upper limit of percentage series compensation is enhanced to a value greater than 90%.

4.1 Design and mathematical model of SVC voltage regulator

The block diagram of voltage regulator for the SVC is presented in Fig. 4.1. The terminal voltage magnitude of the generator (V_t) is sensed through a transducer which has a time constant of T_1 seconds and the measured value of voltage magnitude (V_m) is compared with the reference voltage (V_{ref}). The voltage error is processed by a PI controller having proportional and integral gains K_{P1} and K_{I1} respectively. The output of the PI controller dictates the reactive power reference (Q_{ref}) for the shunt capacitor. This is compared with the actual value of reactive power injected by the shunt capacitor ($Q_{sh} = V_m^2 B_{sh}$) at the generator terminals which is measured (Q_m) by a transducer with time constant T_2 seconds.

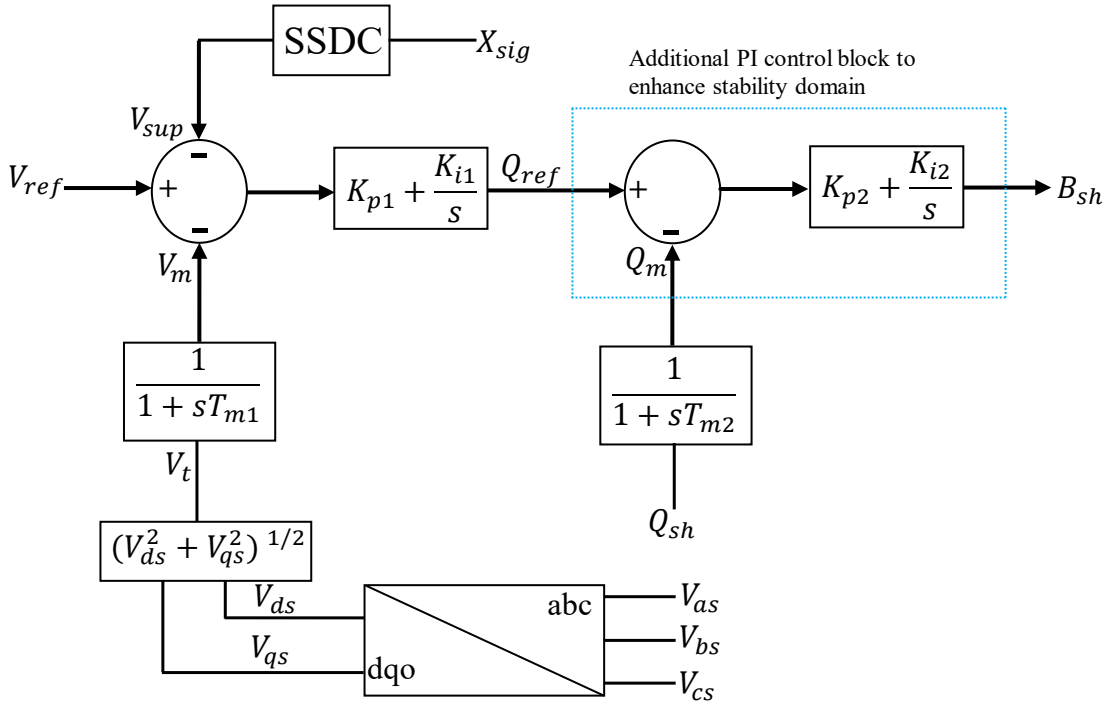

Fig. 4.1: Block diagram of voltage regulator for the SCIG

The reactive power error is processed by a second PI controller with proportional and integral gains K_{P2} and K_{I2} respectively. The susceptance of the SVC (B_{sh}) is determined by the second PI controller based on the reactive power error signal. A supplementary signal $-V_{sup}$ which is the output of a Subsynchronous Damping Controller (SSDC) is added to the signals V_{ref} and $-V_m$ at the first summing block of the voltage regulator which is used to control critical bifurcations in the system mainly due to SSR. The structure of the SSDC will be explained further in Section 4.2. The relationship between the input and output signal of the voltage measurement block in the laplace domain is given by equation (4.1).

$$\frac{V_m(s)}{V_t(s)} = \frac{1}{1+sT_1} \tag{4.1}$$

where s denotes a Laplace transform operation. Cross-multiplying and taking the inverse

Laplace transform, the equation (4.2) which describes the dynamics of the measurement block in the time domain is obtained.

$$T_1 \frac{dV_m}{dt} = -V_m + V_t \tag{4.2}$$

Using the same technique, equation (4.3) which describes the dynamics of the reactive power measurement transducer in the time domain is obtained.

$$T_2 \frac{dQ_m}{dt} = -Q_m + Q_{sh} \tag{4.3}$$

The input-output relationship of the first PI controller in the Laplace domain is expressed using equation (4.4).

$$\frac{Q_{ref}(s)}{V_{ref}(s) - V_m(s) - V_{sup}(s)} = K_{P1} + \frac{K_{I1}}{s} \tag{4.4}$$

Cross-multiplying the denominator of the left hand side in equation (4.4) and introducing an intermediate state variable W_1, equation (4.5) which defines the reactive power reference in the Laplace domain is obtained.

$$Q_{ref}(s) = K_{P1}(V_{ref}(s) - V_m(s) - V_{sup}(s)) + W_1(s) \tag{4.5}$$

where

$$W_1(s) = \frac{K_{I1}}{s}(V_{ref}(s) - V_m(s) - V_{sup}(s)) \tag{4.6}$$

Finally, obtaining the inverse Laplace transform of equations (4.5) and (4.6), equations (4.7) and (4.8) which describe the dynamics of the first PI controller are obtained.

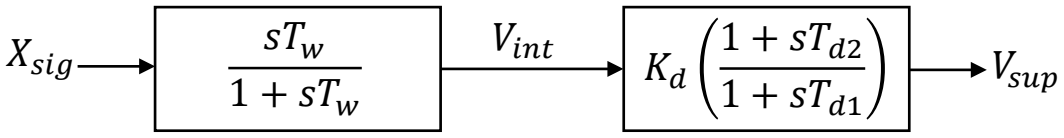

Fig. 4.2: Block diagram of the proposed SSDC

$$\frac{dW_1}{dt} = K_{I1}(V_{ref} - V_m - V_{sup}) \tag{4.7}$$

$$Q_{ref} = K_{P1}(V_{ref} - V_m - V_{sup}) + W_1 \tag{4.8}$$

The same method is used to obtain equations (4.9) and (4.10) which are used to describe the dynamics of the second PI controller which processes the reactive power error signal.

$$\frac{dW_2}{dt} = K_{I2}(Q_{ref} - Q_m) \tag{4.9}$$

$$B_{sh} = K_{P2}(Q_{ref} - Q_m) + W_2 \tag{4.10}$$

The dynamic equations of the series capacitor and line currents are the same as that of (3.8) and (3.10). However, in the equation describing the dynamics of the shunt capacitor shown in (3.1), $X_{sh} = B_{sh}^{-1}$ where B_{sh} is defined by equation (4.10).

4.2 Design and mathematical modeling of SSDC

The design of the subsynchronous damping controller (SSDC) consists of a washout block in series with a compensator which provides a phase lead. The structure of the SSDC is very similar to that of a power system stabilizer used in synchronous generators to eliminate negative damping introduced by high gain exciters ([60, 62]). The signals X_{sig} in Fig. 4.2 considered in this paper are the generator slip (s_g) and the real power at the stator terminals of the generator ($P_e = V_{ds}I_{ds} + V_{qs}I_{qs}$). The relationship between

the input and output signals of the washout block in the Laplace domain is given by the following equation:

$$\frac{sT_w}{1+sT_w} = \frac{V_{int}(s)}{X_{sig}(s)} \tag{4.11}$$

Cross-multiplying and taking the inverse Laplace transform and collecting the derivative terms on the left, equation (4.12) is obtained.

$$T_w(\frac{dX_{sig}}{dt} - \frac{dV_{int}}{dt}) = -X_{sig} \tag{4.12}$$

Similarly, the dynamic equation corresponding to the lead-compensator block in the time domain is obtained which is given below:

$$T_{d1}\frac{dV_{sup}}{dt} - K_d T_{d2}\frac{dV_{int}}{dt} = K_d V_{int} - V_{sup} \tag{4.13}$$

4.3 Eigenvalue analysis of the system with SVC

Eigenvalues of the system are computed for the Jacobian matrix $[J]$ for the linearized system which has been cast in the form $\Delta\dot{X} = [J]\Delta X$ with the fixed capacitor replaced by the SVC with the voltage regulator described in the previous section. In this section, the SSDC is assumed to be absent. The vector of linearized state variables for this system is given by equation (4.14) and the parameters of the voltage regulator of the SVC can be found in Table 4.1.

$$\Delta X = \{\Delta I_{ds}, \Delta I_{qs}, \Delta I_{dr}, \Delta I_{qr}, \Delta I_{dn}, \Delta I_{qn}, \Delta V_{ds}, \Delta V_{qs}, \Delta V_{dc}, \Delta V_{qc}, \Delta s_g, \Delta V_m, \Delta Q_m, \Delta W_1, \Delta W_2\}^T \tag{4.14}$$

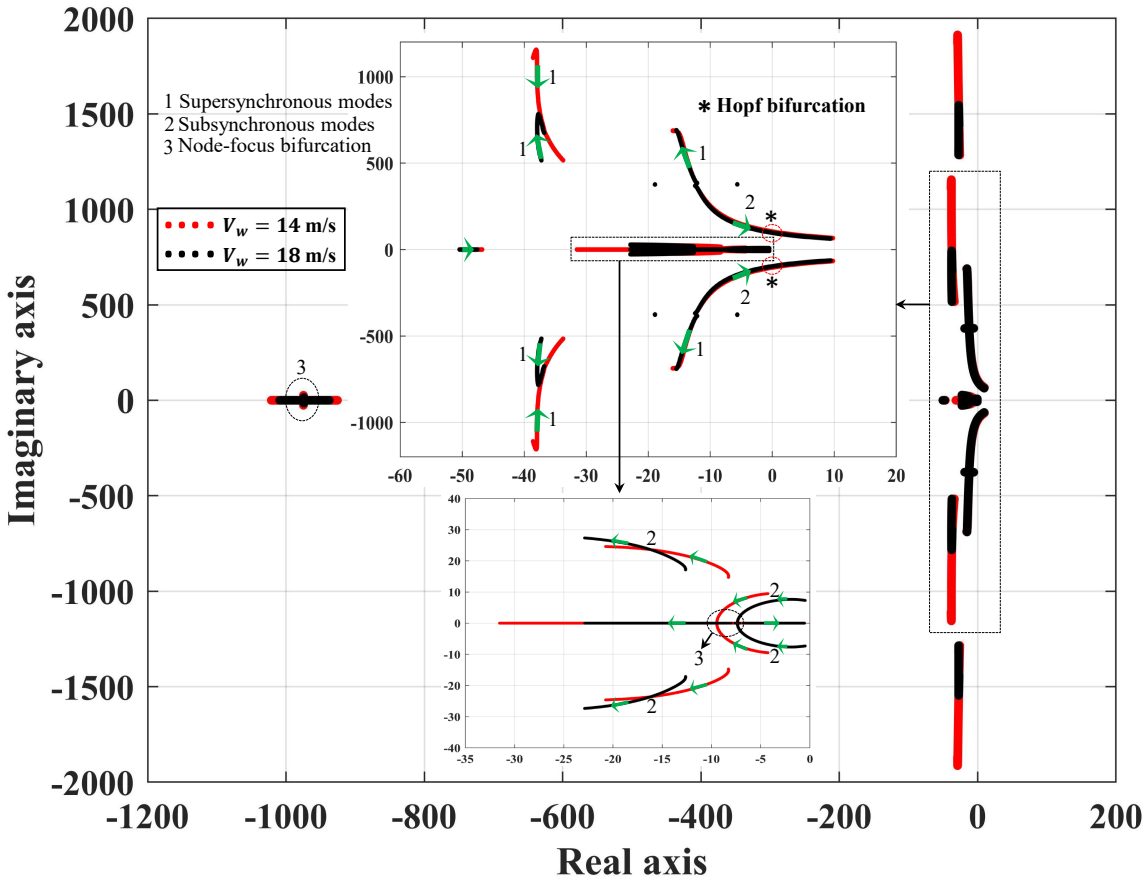

Fig. 4.3: Eigenvalue trajectories for $V_w = 14$ m/s and $V_w = 18$ m/s

Table 4.1: Parameters of SVC voltage regulator considered in Section 4.3.

V_{ref}	T_{m1}	T_{m2}	K_{p1}	K_{p2}	K_{i1}	K_{i2}
1.05 pu	1 ms	1 ms	0.1	0	40	40

4.3.1 Eigenvalues for different wind speeds

Eigenvalues of the system with an SVC at the SCIG terminal in the IEEE - FBM have been plotted in Fig. 4.3 for wind speeds of 14 and 18 m/s as the series compensation K_c is varied from 0.001 up to 0.98. Initially, X/R ratio of the system is assumed to be 20. These wind speeds are considered here as the slip at which the induction generator operates is close to 1% and 3% for wind speeds of 14 and 18 m/s respectively and the

performance can be compared with that of the system compensated with a fixed shunt capacitor as described in 3.3.1. From the eigevalue plot, it is observed that there are 2 kinds of bifurcations which occur. One is the node-focus bifurcation which does not result in a change in the stability of the system and hence is non-critical. However, Hopf bifurcations are also observed in the system due to SSR making it highly critical as the stability of the system is lost after the bifurcation occurs.

When the eigenvalues of the system for lower wind speed of 14 m/s are analyzed, 6 complex conjugate eigenvalue pairs (stable foci) and 3 stable nodes are observed. Among the 6 complex conjugate pairs, 3 are low frequency modes: $\lambda_1 = -4.2745 \pm j9.4714$, $\lambda_2 = -8.2775 \pm j14.712$ and $\lambda_3 = -18.917 \pm j376.28$. The 3 stable nodes are $\lambda_4 = -1021.3$, $\lambda_5 = -925.66$ and $\lambda_6 = -46.858$. As K_c is increased, λ_1 moves further into the left half of the complex plane and the frequency of oscillation decreases; at $K_c = 0.559$, $\lambda_1 = -9.4476 \pm j0.52247$, which is a stable focus, changes into 2 stable nodes: $\lambda_{11} = -9.6715$ and $\lambda_{12} = -9.2474$, which is the result of a node-focus bifurcation. Eigenvalue λ_2 moves further into the left half of the complex plane as K_c increases. When K_c changes from 0.703 to 0.704, $\lambda_3 = -0.0259 \pm j103.85$ crosses over to the right half of the complex plane and changes to $\lambda_2 = 0.0057 \pm j103.66$ as a result of a Hopf bifurcation due to SSR. When K_c increases, λ_4 and λ_5 move toward each other; when K_c changes from 0.938 to 0.939, $\lambda_4 = -979.87$ and $\lambda_5 = -968.33$ collide and transform into a pair of complex-conjugate eigenvalues $\lambda_{45} = -974.14 \pm j4.0936$ as the result of a node-focus bifurcation. It should be noted that the system is already unstable, due to the earlier Hopf bifurcation. Additionally, λ_6 starts moving along the real axis toward the right as K_c increases, but it still remains in the left half of the complex plane.

When the wind speed is 18 m/s, the operating slip of the SCIG is 3.051%. For a small value of compensation $K_c = 0.001$, 7 complex conjugate pairs of eigenvalues and one real eigenvalue all on the left half of the complex plane are observed. Among the complex

conjugate pairs of eigenvalues, 4 of them are of low frequency: $\lambda_1 = -974.04 \pm j14.893$, $\lambda_2 = -12.633 \pm j17.108$, $\lambda_3 = -0.4911 \pm j7.3045$ and $\lambda_4 = -18.911 \pm j376.28$, which follow different pathways on the complex plane as K_c is varied. As the series compensation is increased, λ_1 starts moving toward the right half of the complex plane, and its frequency of oscillation decreases as well. When K_c changes from 0.074 to 0.075, a node-focus bifurcation results from λ_1 splitting into 2 real eigenvalues: $\lambda_{11} = -975.15$, $\lambda_{12} = -972.57$, which then move in opposite directions as K_c is increased. However, these eigenvalues remain in the left half of the complex plane as K_c is increased to 0.95. As K_c changes from 0.697 to 0.698, a second node-focus bifurcation takes place where $\lambda_3 = -7.3577 \pm j0.51245$ transforms into 2 real eigenvalues: $\lambda_{31} = -7.6109$, $\lambda_{32} = -7.136$, and move in opposite directions. An increase in K_c also causes λ_4 to move toward the right half of the complex plane; a Hopf bifurcation occurs in the system when K_c changes from 0.742 to 0.743 as λ_4, which is now $-0.0118 \pm j97.353$, changes to $0.02075 \pm j97.166$, and the system becomes unstable due to SSR. The stability domain is slightly larger in the system with SVC as the critical percentage series compensation K_{cr} changes from 0.655 corresponding to the system without SVC to 0.704 for the system which uses an SVC for reactive power support at the SCIG terminals at a slip of approximately 1%. Similarly, K_{cr} increases from 0.681 to 0.743 for a slip close to 3%.

4.3.2 Eigenvalues for various grid strengths

Eigenvalues are computed for various levels of series compensation for 3 different grid strength which is indicated by the X/R ratio of the line and are traced on the complex plane as given in Fig. 4.4. The system is analyzed for a lower wind speed of $14\,m/s$ because it is observed from the previous section that subsynchronous oscillations occurs at low values of series compensation K_c when the power generated is low. The system with $X/R = 10$ has a node-focus bifurcation as K_c changes from 0.563 to 0.564 as the

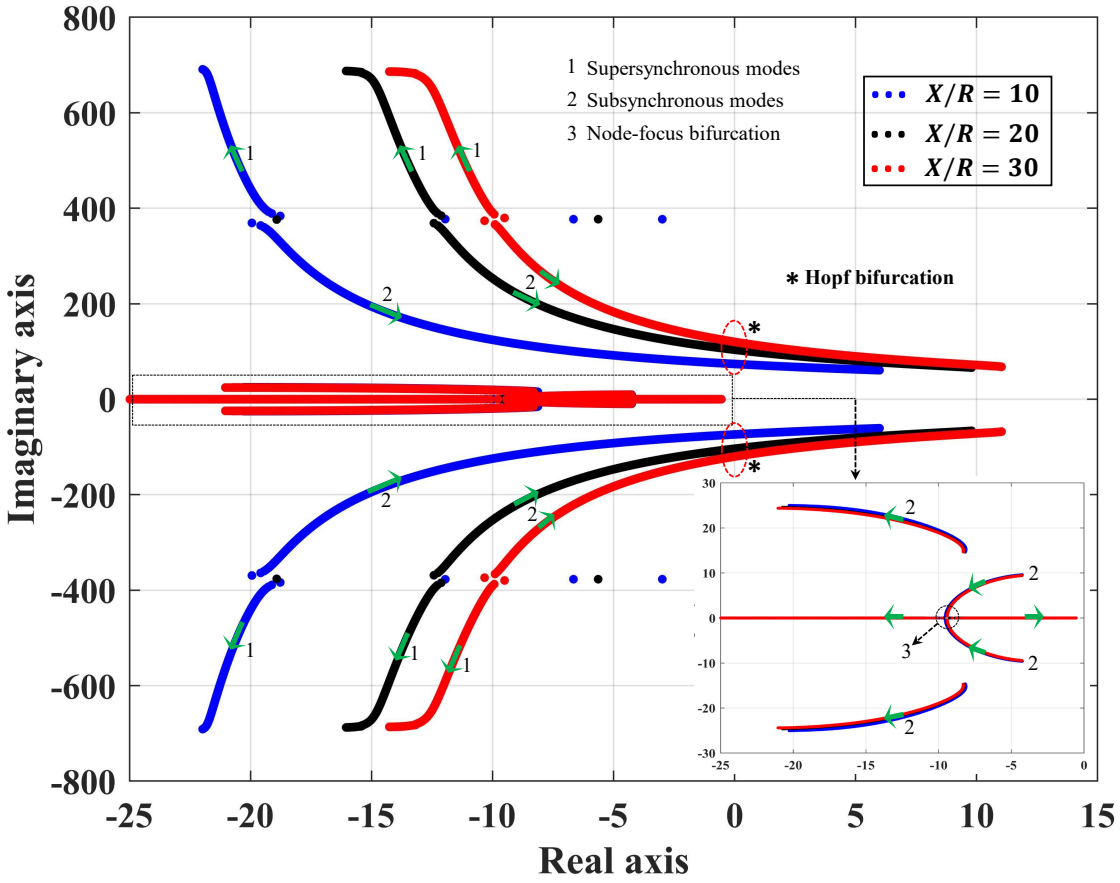

Fig. 4.4: Eigenvalue trajectories for various grid strengths

Table 4.2: Critical series compensation for system with and without SVC

X/R ratio	K_{cr} without SVC	K_{cr} with SVC
10	0.809	0.858
15	0.717	0.768
20	0.655	0.704
25	0.611	0.658
30	0.579	0.623

stable focus $\lambda = -9.5344 \pm j0.4132$ transforms into 2 stable nodes each moving in the opposite direction as K_c is increased. When K_c changes from 0.857 to 0.858, the complex conjugate eigenvalue pair $\lambda_{cr} = -0.0528 \pm j73.976$ crosses over to the right half of the complex plane and becomes $\lambda_{cr} = 0.0069 \pm j73.81$ as a result of a Hopf bifurcation which

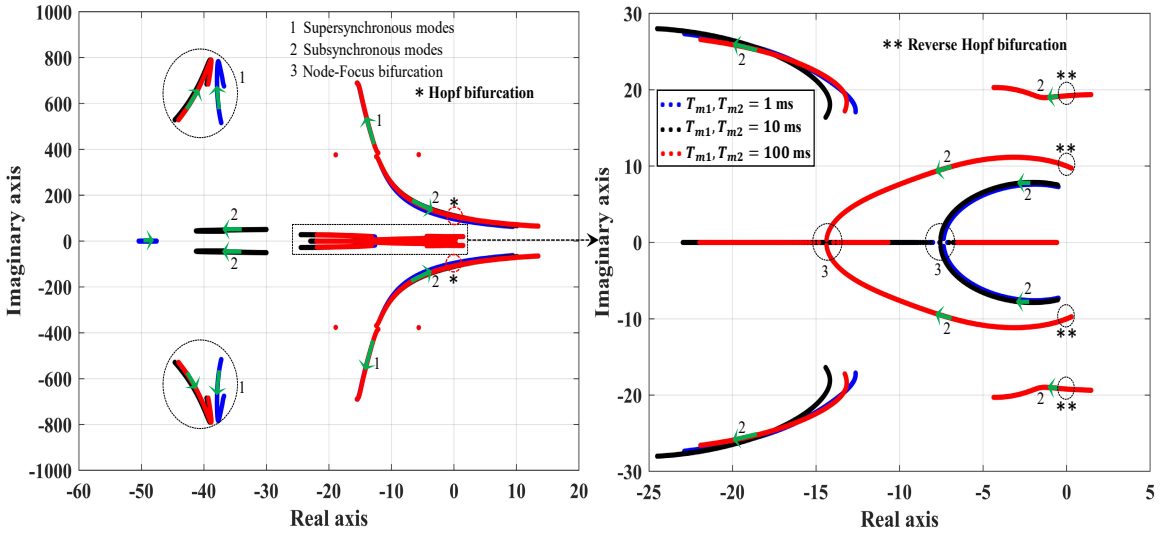

Fig. 4.5: Eigenvalue trajectories for various measurement delays

gives rise to unstable oscillations at subsynchronous frequency.

Similar behavior is encountered in the system for higher X/R ratios but at lower values of K_c. The node-focus bifurcation occurs when K_c changes from 0.558 to 0.559 and 0.557 to 0.558 for X/R ratios of 20 and 30 respectively. The system undergoes a Hopf bifurcation when K_c is close to 0.704 and 0.623 with $\lambda_{cr} = 0.0057 \pm j103.66$ and $\lambda_{cr} = 0.0085 \pm j120.02$ for X/R ratios of 20 and 30 respectively. Table 4.2 shows the critical value of series compensation for the systems with and without SVC for various X/R ratios. The system with SVC has a slightly larger stability domain than the system without SVC. Also, as the strength of the grid decreases, the compensation level at which Hopf bifurcation occurs becomes smaller making it crucial to implement a damping controller in order to be able to mitigate this phenomenon causing instability.

4.3.3 Eigenvalues for different measurement time delays

In control systems, the reference value of a quantity is compared against the actual value which is measured using a transducer. Measurement transducers have finite time constants which are usually ignored. However, these time constants have an effect on

the stability domain of the system with respect to series compensation which would be studied in this section. Time delays in measurement of voltage magnitude and reactive power have been modeled using a first order transfer function. Eigenvalues of the system are traced when K_c is varied from 0.001 to 0.95 and are plotted on the complex plane for 3 different measurement time delays in the voltage regulator. The system is analyzed for higher wind speed $V_w = 18$ m/s because certain unique bifurcations occur in this system for this wind speed. When the measurement time delay is 1 ms, the system undergoes a node-focus bifurcation at $K_c = 0.075$ and $K_c = 0.704$ and a Hopf bifurcation due to SSR at $K_c = 0.743$. With a measurement delay of 10 ms, the system undergoes a Hopf bifurcation at $K_c = 0.679$ and a node-focus bifurcation at $K_c = 0.691$ as a stable focus transforms into 2 stable nodes but the system is already unstable at $K_c = 0.679$.

As the measurement time delay is increased to 100 ms, for $K_c = 0.001$, there are 2 pairs of complex conjugate eigenvalues $\lambda_1 = 1.4651 \pm j19.368$ and $\lambda_2 = 0.2911 \pm j9.7375$ on the right half of the complex plane which results in the system being unstable. When K_c increases, these two pairs move towards the left half of the complex plane and when $K_c = 0.038$, $\lambda_1 = 1.1153 \pm j19.34$ and $\lambda_2 = -0.0075 \pm j10.014$. Though the real part of λ_2 is negative, the system still is unstable as λ_1 has a positive real part. When K_c approaches 0.172, λ_1 changes to $-0.0068 \pm j19.208$ which means all the eigenvalues of the system have negative real parts indicating a stable system. Since the system changes from an unstable state to a stable state because of the movement of a complex conjugate pair of eigenvalues to the left half of the complex plane from the right, the system undergoes a reverse Hopf bifurcation.

The reason for this phenomenon can be explained as follows: the system is unstable for small values of series compensation due to increased time delays in measurement. When the series compensation is increased, the system becomes more and more stable because increasing the series capacitive reactance decreases the effective line reactance which

decreases the time constant of the electrical circuit thus compensating for measurement delays. Hence, the system can be stabilized by increasing the series compensation above a certain threshold when instability due to large measurement delays are experienced. The upper limit of K_c is determined by the Hopf bifurcation which occurs due to SSR at $K_c = 0.683$ where $\lambda_{cr} = 0.0223 \pm j108.57$. Finally, a node-focus bifurcation takes place at $K_c = 0.865$ where a stable focus changes into 2 stable nodes but the system has already become unstable due to SSR.

4.4 Eigenvalues of the system with SVC and SSDC

In this section, the performance of the designed damping controllers based on slip signal (SSDC-A) and real power (SSDC-B) is analyzed through computing eigenvalue trajectories as K_c is varied from 0.001 to 0.95 for various X/R ratios, wind speeds and measurement time delays. The controller gains of the SVC and SSDC are tuned for the various scenarios considered to obtain a stable system characterized by all eigenvalues on the left half of the complex plane up to a series compensation of 95%. The parameters of the network and wind speeds are the same as those considered in Section 4.3.

4.4.1 Eigenvalues for low and high wind speeds

Eigenvalue trajectories of the system for an X/R ratio of 20 with SSDC-A are computed for wind speeds V_w of 14 and 18 m/s and are presented in Figure 4.6 on the left. The subsynchronous mode starts moving toward the right half of the complex plane but even for a compensation of $K_c = 0.95$, the corresponding eigenvalue pairs are $\lambda_{sub} = -3.2013 \pm j79.178$ and $\lambda_{sub} = -8.2223 \pm j72.016$ for wind speeds of 14 and 18 m/s, respectively, which have negative real parts. The eigenvalue closest to the imaginary axis is $\lambda = -0.00276$, which corresponds to $V_w = 18$ m/s.

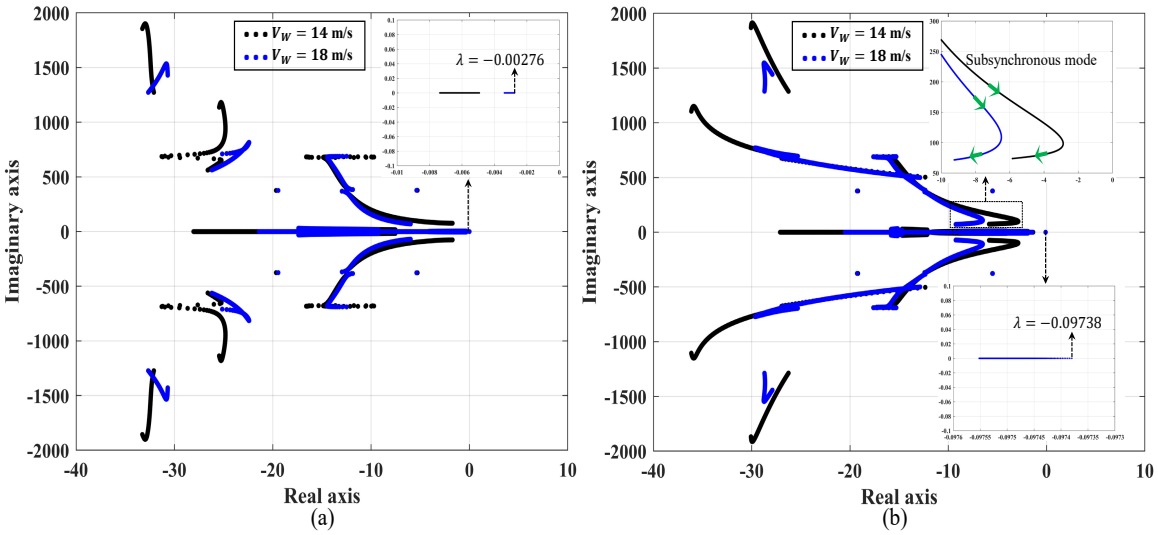

Fig. 4.6: Eigenvalues for low and high wind speeds with (a) SSDC - A (b) SSDC - B

Table 4.3: SVC control gains and SSDC considered in Section 4.4.1.

SSDC	K_{p1}	K_{p2}	K_{i1}	K_{i2}	K_d	T_{d1}	T_{d2}	T_w
A	0.5	0.1	1	1	450	10 ms	150 ms	10 s
B	0.1	0	100	100	0.1	10 ms	100 ms	10 s

Similarly, for the system with SSDC-B, eigenvalue trajectories are computed for wind speeds of 14 and 18 m/s and are plotted in Figure 4.6 to the right. It is observed that the damping of the subsynchronous mode starts reducing as the amount of series compensation K_c is increased from 0.001 up to 0.793; beyond that, the damping starts increasing as the compensation is increased. A similar phenomenon is observed for $V_w =$ 18 m/s, except that the damping of the subsynchronous mode decreases for K_c up to 0.725; beyond this, the damping increases. However, all the eigenvalues of the system for both low and high wind speeds lie on the left half of the complex plane, which shows that the Hopf bifurcation is eliminated for the entire range of series compensation considered. The parameters of the SVC voltage regulator and SSDC-A and B are listed in Table 4.3.

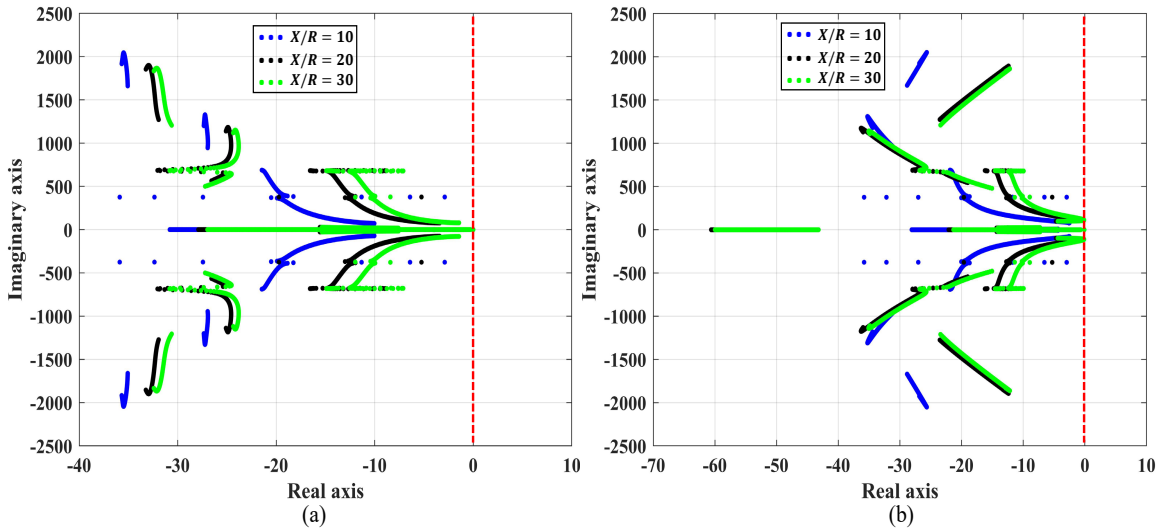

Fig. 4.7: Eigenvalues for various grid strengths with (a) SSDC - A (b) SSDC - B

4.4.2 Eigenvalues for varying grid strengths

Eigenvalues of the system with SSDC-A and SSDC-B are traced on the complex plane for varying grid strengths, which is a function of the X/R ratio. It was shown in Section 4.3.2 that as the strength of the grid decreases, the percentage series compensation at which the system becomes unstable due to SSR becomes smaller. In Figure 4.7, it is shown that with SSDC-A and SSDC-B, the eigenvalues of the system are all found to lie on the left half of the complex plane, thus eliminating the Hopf bifurcation due to SSR. In SSDC-B, with controller gains $K_{p1}, K_{p2} = 0.1$ and $K_{i1}, K_{i2} = 50$ and a stabilizer gain K_{SS} of 0.3, all the modes are found to be well damped for X/R ratios to about 15. Beyond that, the stabilizer gain is increased to 0.7 and all the modes are found to be well damped for $X/R = \{10, 20, 30\}$, and those are shown in Figure 4.7b. The values of control gains of the SVC and SSDC are presented in Table 4.4. Re-tuning of the stabilizer and PI controllers in the voltage regulator are not needed with SSDC-A for all the X/R ratios considered here.

Table 4.4: SVC control gains and SSDC parameters considered in Section 4.4.2.

SSDC	K_{p1}	K_{p2}	K_{i1}	K_{i2}	K_d	T_{d1}	T_{d2}	T_w
A	0.55	0.1	1	1	450	10 ms	150 ms	10 s
B	0.1	0	50	50	0.7	10 ms	100 ms	10 s

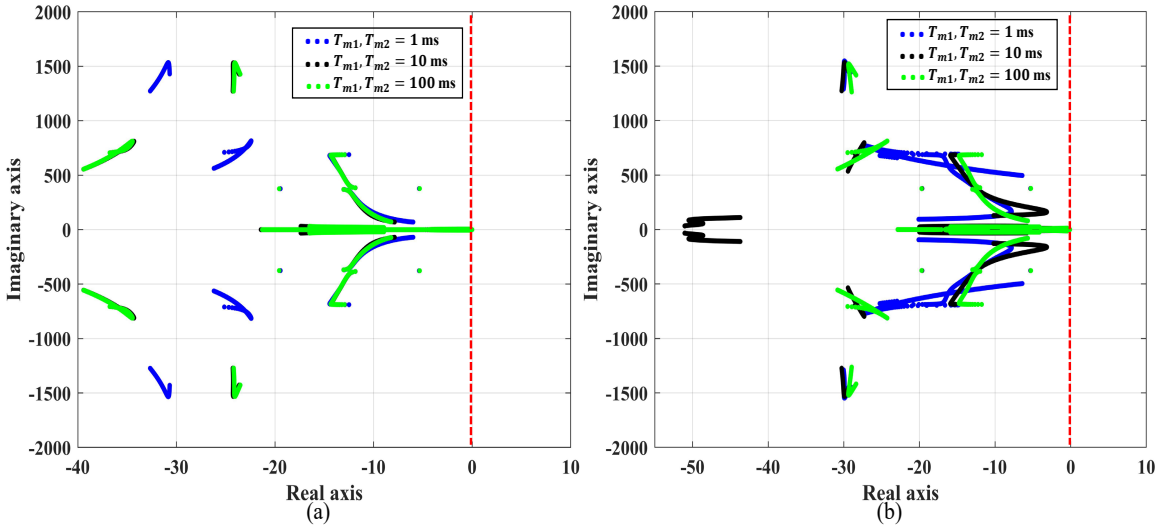

Fig. 4.8: Eigenvalues for different measurement delays with (a) SSDC - A (b) SSDC - B

4.4.2.1 Eigenvalue trajectories for varying measurement time delays in the SVC

Eigenvalues of the system with SSDC for 3 values of measurement delays (1, 10 and 100 ms) are plotted on the complex plane and are presented in Figure 4.8. The parameters of SSDC-A and -B and that of the SVC with SSDC-A are same as those presented in Table 4.3. For the system with SSDC-A, all the modes are damped and no re-tuning of the PI controls of the voltage controller is needed. However, with SSDC-B, the controller gains of the SVC have to be re-tuned in order to obtain a stable system up to 95% series compensation for each of the time delays considered here; those values are presented in Table 4.5. Hence, it is shown that both SSDC-A and SSDC-B are able to mitigate subsynchronous oscillations as well as the unstable low frequency modes, which appear for a time delay of 100 ms in the system without the damping controller.

Table 4.5: SVC control gains with SSDC-B considered in Section 4.4.2.1.

T_{m1}, T_{m2}	K_{p1}	K_{p2}	K_{i1}	K_{i2}
1 ms	0.1	0	200	100
10 ms	0.1	0.2	100	100
100 ms	0.1	0.3	300	10

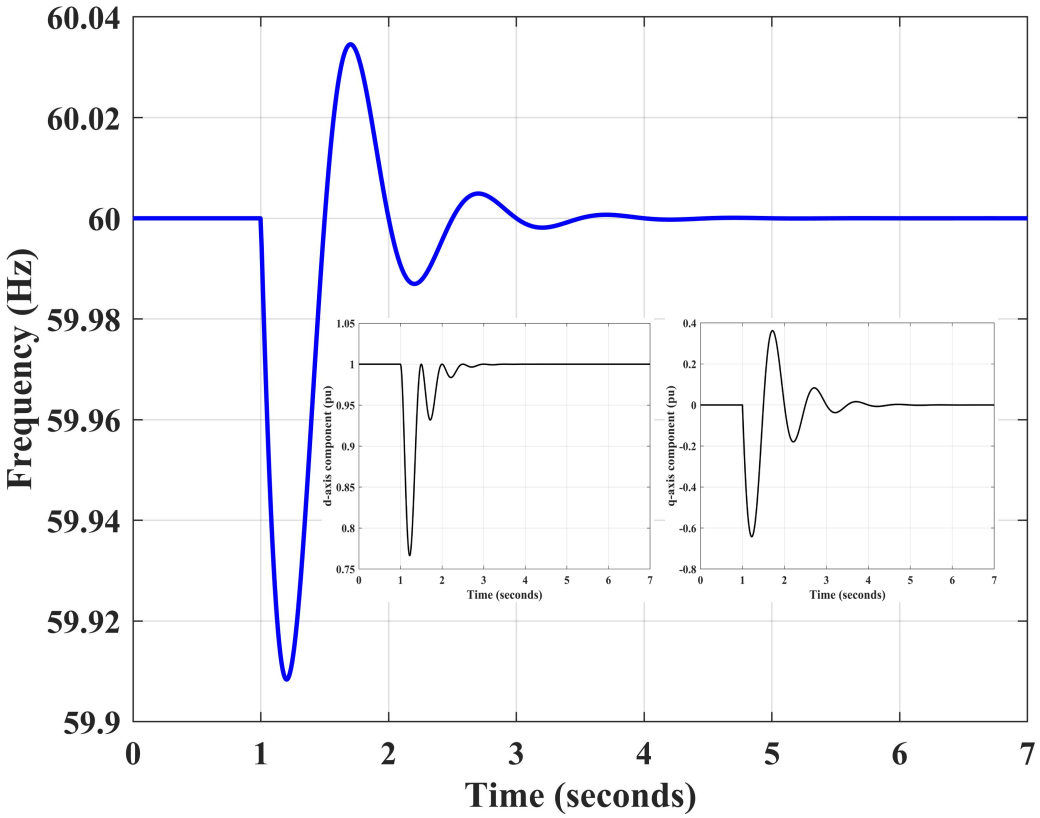

Fig. 4.9: Disturbance simulation in grid frequency

4.5 Time domain simulations

The dynamic responses of the system are presented in this section to disturbances in grid voltage and frequency. The disturbance with respect to the grid voltage involves a reduction in the voltage magnitude by 15% for about 0.1 s and then the voltage is restored to 1 pu. In real time, this may occur due to a three phase fault at a bus resulting in a reduction in all the surrounding bus voltages and the fault is assumed to be cleared in 6

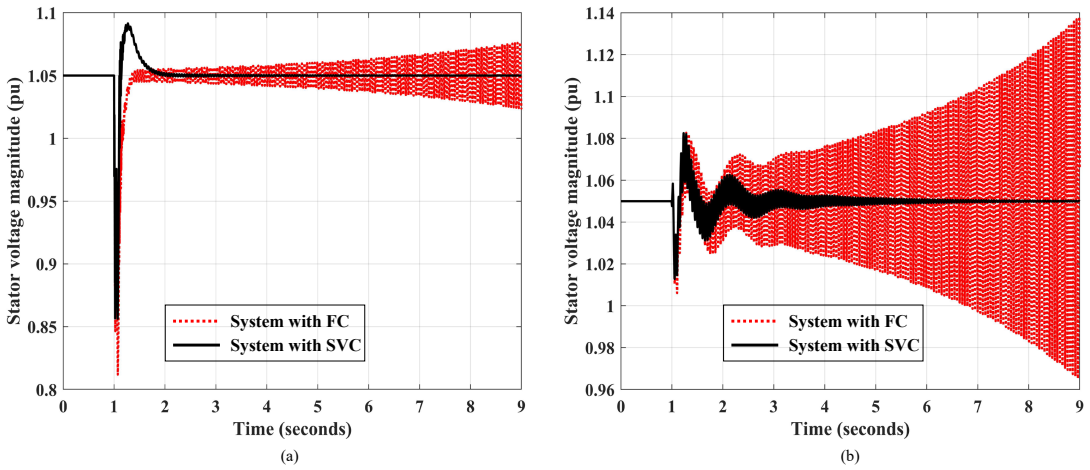

Fig. 4.10: Stator voltage magnitude response to a (a) Grid voltage disturbance, and (b) Grid frequency disturbance

cycles (0.1 seconds). A frequency disturbance is simulated using a mathematical function given by

$$f(t) = f_o - exp(-\tau t)\sin(\omega_n t) \tag{4.15}$$

where τ is the damping term and ω_n is the frequency of the disturbance. Here, $\tau = 2.5$ and $\omega_n = 2$ rad/s which is of the order of frequency involving electromechanical oscillations in the grid. This mimics the frequency changes in the grid due to the response of speed governors to disturbances in the grid. As the frequency of the is perturbed, the d and q components of the grid voltage change accordingly which are shown in Fig. 4.9.

The dynamic responses of the system with SVC are plotted in Figs. 4.10 to 4.12 for an X/R ratio of 30 and a wind speed of 14 m/s and 60% series compensation. The controller parameters of SVC are chosen as $K_{P1} = 0.1$, $K_{P2} = 0$, $K_{I1} = K_{I2} = 40$. In this system, the damping controller is absent. The dynamic responses of the system without SVC described in Chapter 3 are also plotted for comparison. It can be observed from the plots that the system with SVC has a damped response to the disturbance in grid voltage and frequency. However, the system with fixed capacitors at the SCIG terminals is unstable as the dynamic responses show growing oscillations with respect to time.

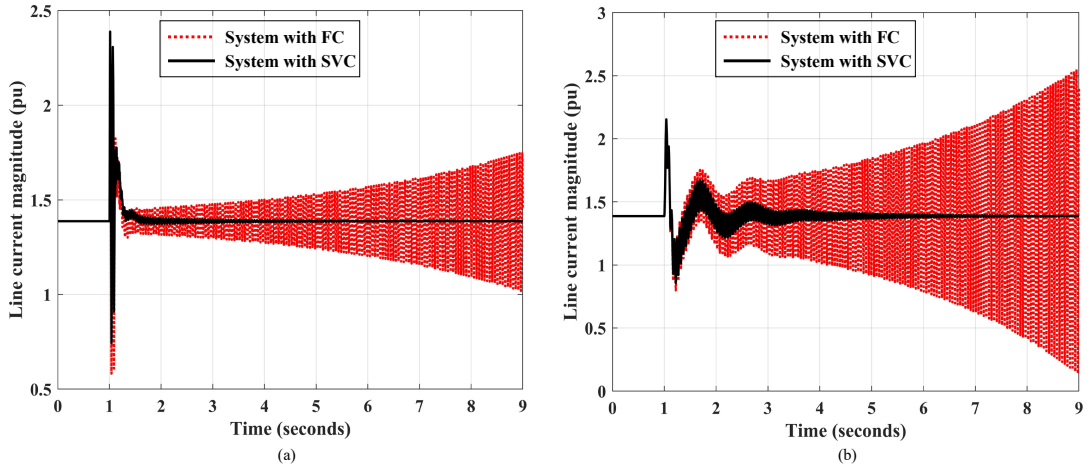

Fig. 4.11: Line current magnitude response to a (a) Grid voltage disturbance, and (b) Grid frequency disturbance

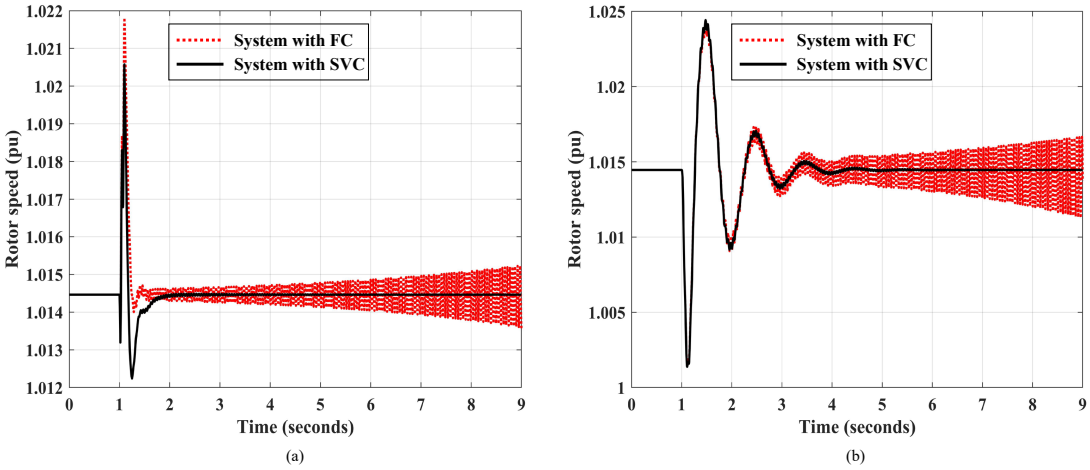

Fig. 4.12: Rotor speed response to a (a) Grid voltage disturbance, and (b) Grid frequency disturbance

The dynamic responses of the system with SVC but without the SSDC and the system with the SVC equipped with an SSDC based on the induction generator slip and the real power at the terminals of the SCIG are presented. The system is simulated for a wind speed of 14 m/s and an X/R ratio of 20 with a series compensation level of 71%. Responses of the voltage magnitude, real power and reactive power delivered at the stator terminals of the SCIG show oscillations of increasing amplitude for the case with SVC and without the SSDC due to SSR. The system equipped with the SSDC results in an

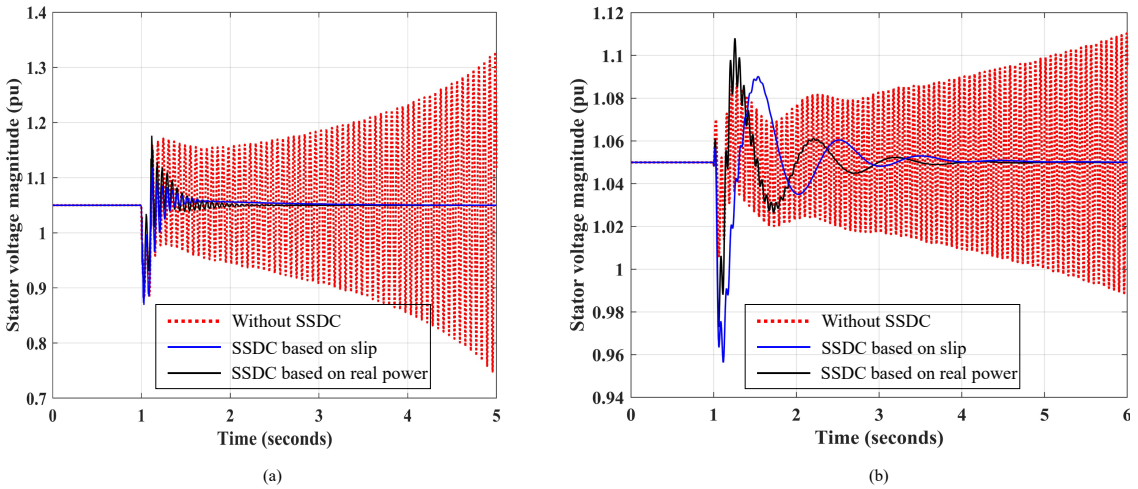

Fig. 4.13: Stator voltage magnitude response to a (a) Grid voltage disturbance, and (b) Grid frequency disturbance

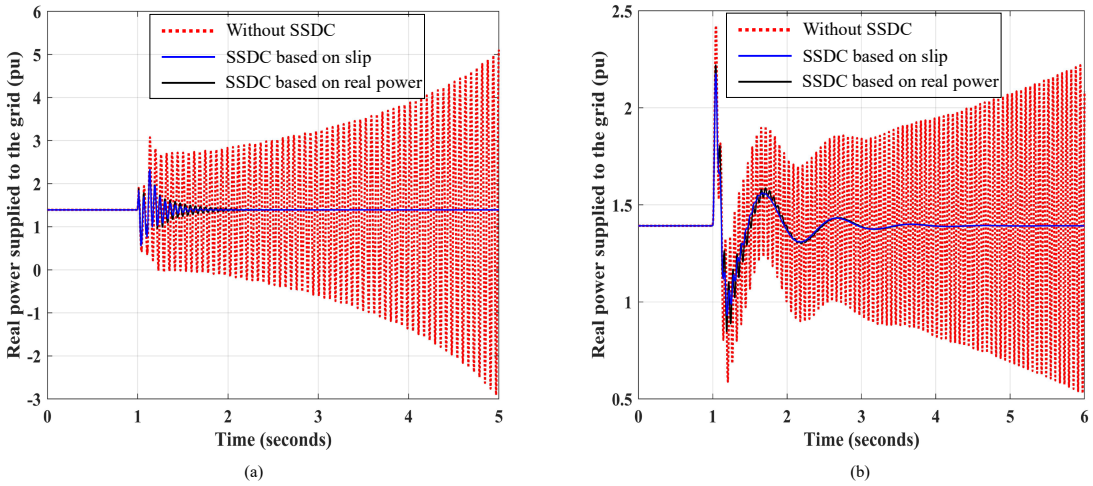

Fig. 4.14: Real power delivered in response to a (a) Grid voltage disturbance, and (b) Grid frequency disturbance

oscillatory response which is well-damped.

Oscillations in the stator and rotor currents result in growing oscillations in the electrical torque produced which causes a mismatch in the mechanical torque input from the wind and the electrical torque output of the generator which is manifested as oscillations of increasing magnitude in the speed of the rotor. However, the system with SSDC returns to the same operating point after a few cycles which can be observed from the phase-plane

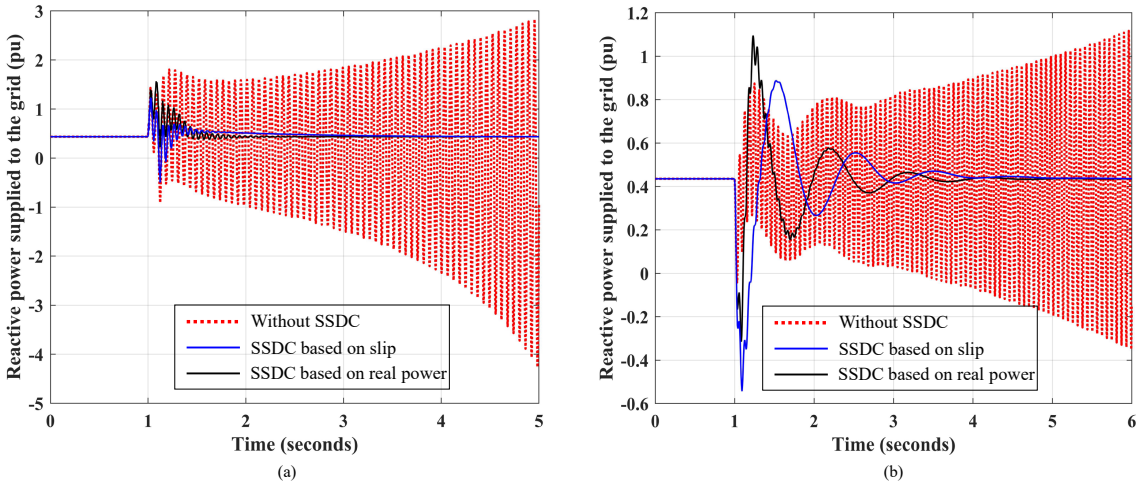

Fig. 4.15: Reactive power delivered in response to (a) Grid voltage disturbance, and (b) Grid frequency disturbance

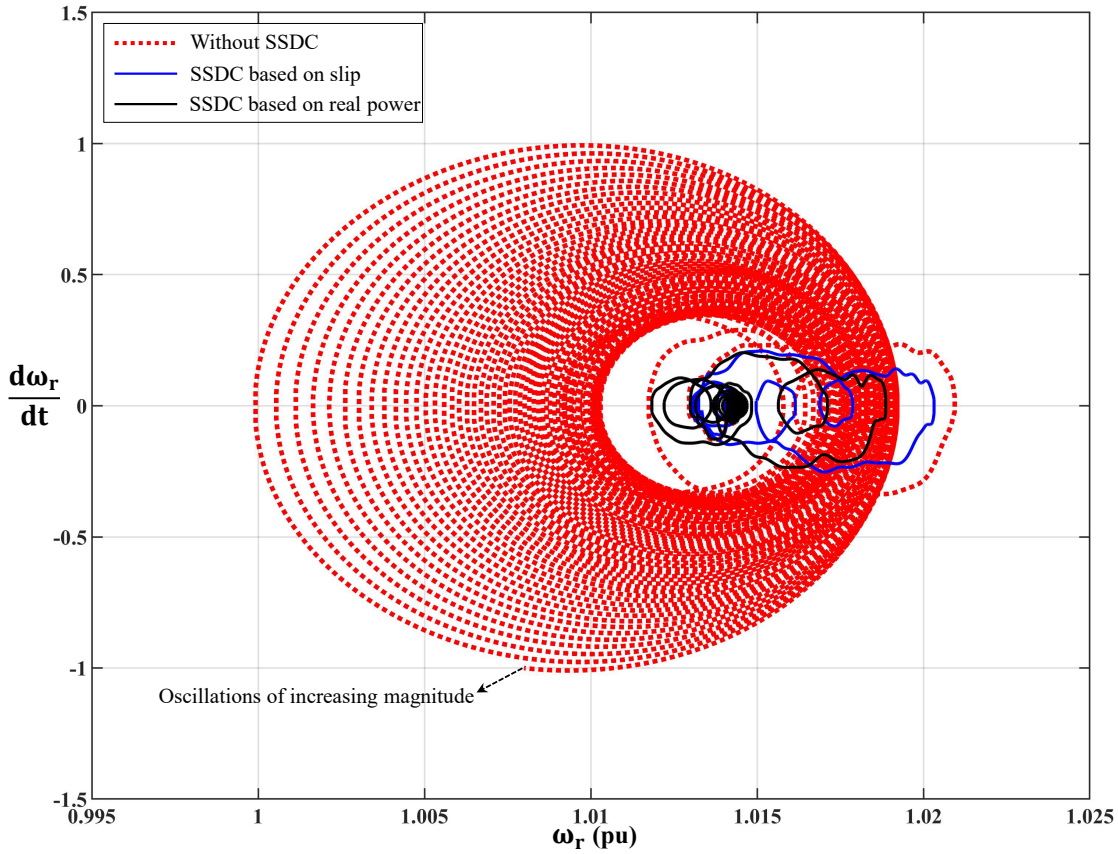

Fig. 4.16: Dynamic torque-speed characteristics in response to a grid voltage disturbance

trajectory with respect to rotor speed shown in Figs. 4.16 and 4.17 when the system is subjected to a disturbance in the grid voltage and grid frequency respectively.

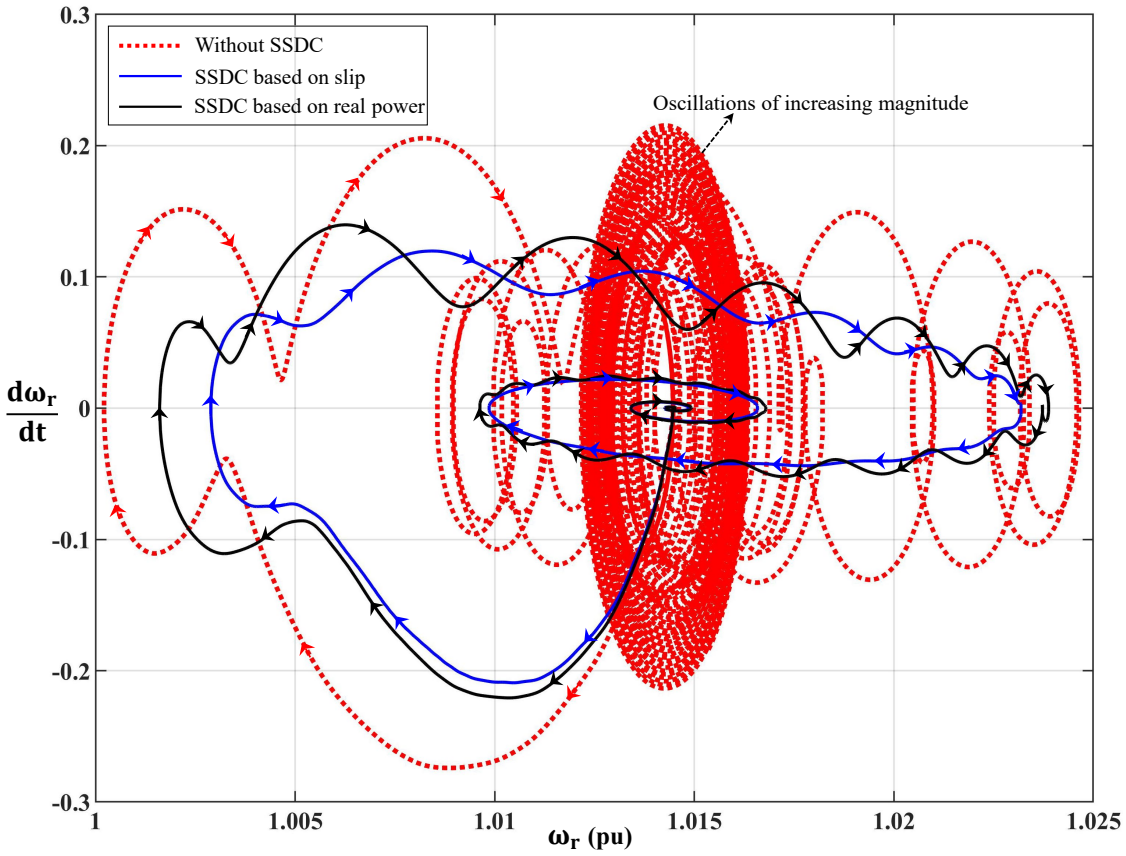

Fig. 4.17: Dynamic torque-speed characteristics in response to a grid frequency disturbance

4.6 Conclusion

An SVC used in the place of a fixed capacitor is able to eliminate the unstable node at small values of series compensation. In addition to a Hopf bifurcation, a node-focus bifurcation is also introduced into the system which may not affect the stability of the system. Also, the series compensation level at which SSR occurs is increased with the SVC. The Hopf bifurcation point is affected by the strength of the grid in systems with fixed capacitors as well as an SVC equipped with a voltage regulator. As the strength of the grid decreases, the system becomes unstable for smaller values of series compensation due to SSR due to a decrease in the resonant frequency as the X/R ratio of the line increases. However, the Hopf bifurcation point can be shifted in the system with SVC by

proper adjustment of controller parameters in the voltage regulator.

With higher time delays, there is a possibility of unstable low frequency oscillations which are eliminated by higher levels of series compensation. Hence, stable operation of a system with higher measurement delays might not be possible without a minimum level of series compensation. A supplementary damping controller is needed for stable operation of the system for high levels of series compensation. The proposed SVC voltage regulator with the supplementary damping controller based on the generator slip signal as well as the real power at the terminals is able to successfully damp subsynchronous oscillations when tuned properly.

CHAPTER 5

Dynamic analysis of Squirrel Cage Induction Generator - Wind Turbine with a Non-Radial Interconnection to the Grid

In this chapter, the modeling and analysis of an SCIG - WT in the modified IEEE Second Benchmark consisting of an induction generator coupled to the grid through a double circuit line is presented. The previous chapter dealt with the analysis of bifurcations in SCIG-WTs coupled to the grid through a series compensated radial interconnection. The goal of this chapter is to examine the impact of network topology along with other parameters on the stability domain with respect to series compensation in a weak grid. Research presented in [63] claims that a double-cage induction generator based wind farm may not experience instability due to subsynchronous resonance in the presence of a non-radial interconnection to the grid. In this chapter, it has been shown through eigenvalue calculations and time domain simulations that instability via Hopf bifurcations due to subsynchronous resonance are inevitable in SCIG-WTs even in the absence of a radial interconnection.

5.1 Modeling of network

The single line diagram of the modified IEEE second benchmark system is shown in Fig. 5.1. It consists of a SCIG-WT connected to the grid through a step-up transformer followed by a double circuit line which is then coupled to the grid through a short line. Reactive power needed by the SCIG is provided by shunt capacitor banks at the stator terminals. The equations used to model the dynamics of the induction generator have been derived in Chapter 2. The matrices given below are used to develop the dynamic

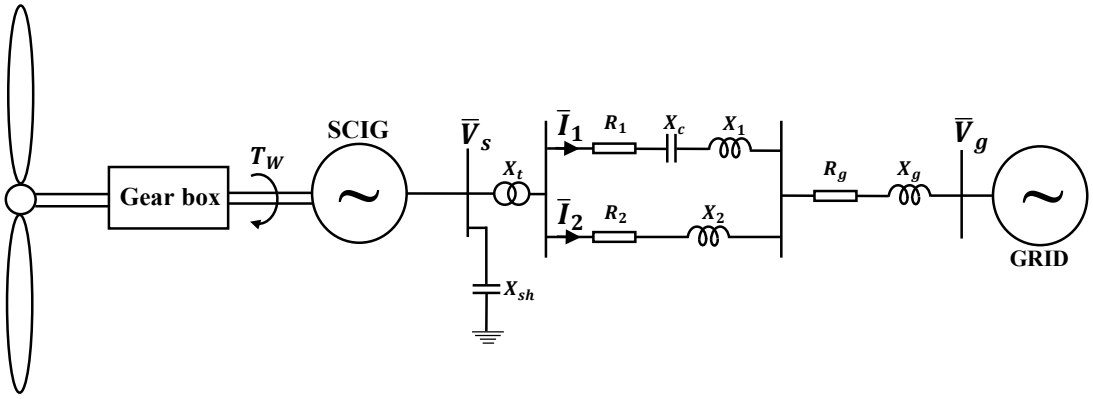

Fig. 5.1: Single line diagram of modified IEEE Second Benchmark Model

model of the network:

$$[Z_T] = \begin{bmatrix} R_t & -X_t \\ X_t & R_t \end{bmatrix}, [Z_G] = \begin{bmatrix} R_g & -X_g \\ X_g & R_g \end{bmatrix}, [Z_1] = \begin{bmatrix} R_1 & -X_1 \\ X_1 & R_1 \end{bmatrix}, [Z_2] = \begin{bmatrix} R_2 & -X_2 \\ X_2 & R_2 \end{bmatrix}$$

The following reactances are defined: $X_{n1} = X_t + X_g + X_1$, $X_{n2} = X_t + X_g$, $X_{n3} = X_t + X_g + X_2$. Also, define matrices: $[Z_{N1}] = [Z_T + Z_1 + Z_G]$, $[Z_{N2}] = [Z_T + Z_G]$ and $[Z_{N3}] = [Z_T + Z_2 + Z_G]$. Using the quantities defined, the currents in the electrical network are modeled using the following differential equations:

$$\frac{X_{n1}}{\omega_s}[U]\frac{d}{dt}\{I_{n1}\} + \frac{X_{n2}}{\omega_s}[U]\frac{d}{dt}\{I_{n2}\} = -[Z_{N1}]\{I_{n1}\} - [Z_{N2}]\{I_{n2}\} - \{V_c\} - \{V_g\} + \{V_s\} \tag{5.1}$$

$$\frac{X_{n2}}{\omega_s}[U]\frac{d}{dt}\{I_{n1}\} + \frac{X_{n3}}{\omega_s}[U]\frac{d}{dt}\{I_{n2}\} = -[Z_{N2}]\{I_{n1}\} - [Z_{N3}]\{I_{n2}\} - \{V_g\} + \{V_s\} \tag{5.2}$$

The elements of vectors $\{I_{n1}\}$, $\{I_{n2}\}$, $\{V_s\}$ and $\{V_c\}$ are given by:

$$\{I_{n1}\} = [I_{d1} \quad I_{q1}]^T \tag{5.3}$$

$$\{I_{n2}\} = [I_{d2} \quad I_{q2}]^T \tag{5.4}$$

$$\{V_s\} = [V_{ds} \quad V_{qs}]^T \tag{5.5}$$

$$\{V_c\} = [V_{dc} \quad V_{qc}]^T \tag{5.6}$$

The voltage across the series capacitor in line 1 is modeled using equation given below:

$$\frac{1}{\omega_s}[U]\frac{d}{dt}\{V_c\} = [Z_{se}]\{I_{n1}\} + [N_1]\{V_c\} \tag{5.7}$$

where $[Z_{se}] = X_c[U]$.

The dynamics of the shunt capacitor voltage at the terminals of the SCIG are described by the following equation:

$$\frac{1}{\omega_s}[U]\frac{d}{dt}\{V_s\} = [Z_{sh}]\{I_s - I_{n1} - I_{n2}\} + [N_1]\{V_s\} \tag{5.8}$$

where $[Z_{sh}] = X_{sh}[U]$.

5.2 Linearization of mathematical model

The dynamic equations of the network presented in Section 5.1 are linearized and presented in this section. Linearized versions of equations (5.1) and (5.2) are given below:

$$\frac{X_{n1}}{\omega_s}[U]\frac{d}{dt}\{\Delta I_{n1}\} + \frac{X_{n2}}{\omega_s}[U]\frac{d}{dt}\{\Delta I_{n2}\} = -[Z_{N1}]\{\Delta I_{n1}\} - [Z_{N2}]\{\Delta I_{n2}\} - \{\Delta V_c\} + \{\Delta V_s\} \tag{5.9}$$

$$\frac{X_{n2}}{\omega_s}[U]\frac{d}{dt}\{\Delta I_{n1}\} + \frac{X_{n3}}{\omega_s}[U]\frac{d}{dt}\{\Delta I_{n2}\} = -[Z_{N2}]\{\Delta I_{n1}\} - [Z_{N3}]\{\Delta I_{n2}\} + \{\Delta V_s\} \tag{5.10}$$

Since the voltage of the grid is assumed to be fixed under equilibrium conditions, $\{\Delta V_{dqg}\} =$

0 and hence, it does not appear in the linearized equations (5.9) and (5.10). Linearized expressions for equations (5.7) and (5.8) can be found below:

$$\frac{1}{\omega_s}[U]p\{\Delta V_c\} = [Z_{se}]\{\Delta I_{n1}\} + [N_1]\{\Delta V_c\} \tag{5.11}$$

$$\frac{1}{\omega_s}[U]p\{\Delta V_s\} = [Z_{sh}]\{\Delta I_s - \Delta I_{n1} - \Delta I_{n2}\} + [N_1]\{\Delta V_s\} \tag{5.12}$$

The various vectors used in equations (5.9) to (5.12) are defined below:

$$\{\Delta I_{n1}\} = [\Delta I_{d1} \quad \Delta I_{q1}]^T \tag{5.13}$$

$$\{\Delta I_{n2}\} = [\Delta I_{d2} \quad \Delta I_{q2}]^T \tag{5.14}$$

$$\{\Delta V_s\} = [\Delta V_{ds} \quad \Delta V_{qs}]^T \tag{5.15}$$

$$\{\Delta V_c\} = [\Delta V_{dc} \quad \Delta V_{qc}]^T \tag{5.16}$$

Table 5.1: Subset of parameters of the electrical network (all parameters are specified in per unit on a common base).

$\boldsymbol{R_t}$	$\boldsymbol{X_t}$	$\boldsymbol{R_g}$	$\boldsymbol{X_g}$	$\boldsymbol{X_{sh}}$	$\boldsymbol{V_g}$
0	0.05	0	0.05	1.2	1

5.3 Eigenvalue analysis of IEEE SBM with SCIG-WT

The linearized model of the system under study consists of equations (2.44), (2.45), (2.50), (5.9), (5.10), (5.11) and (5.12). The complete list of linearized state variables of the system is given below:

$$\Delta X = \{\Delta I_{ds}, \Delta I_{qs}, \Delta I_{dr}, \Delta I_{qr}, \Delta I_{d1}, \Delta I_{q1}, \Delta I_{d2}, \Delta I_{q2}, \Delta V_{ds}, \Delta V_{qs}, \Delta V_{dc}, \Delta V_{qc}, \Delta s_g\}^T \tag{5.17}$$

Table 5.2: Eigenvalues of modified IEEE-SBM with IG1 for 60% series compensation.

$\boldsymbol{\lambda_i}$	$\boldsymbol{-\sigma \pm j\omega}$	**Participating States**
λ_1	$-30.963 \pm j1835.9$	I_{ds}, I_{qs}, I_{dr}, I_{qr}, I_{d1}, I_{q1}, I_{d2}, I_{q2}, V_{ds}, V_{qs}
λ_2	$-39.772 \pm j1082$	I_{ds}, I_{qs}, I_{dr}, I_{qr}, I_{d1}, I_{q1}, I_{d2}, I_{q2}, V_{ds}, V_{qs}
λ_3	$-12.999 \pm j658.23$	I_{ds}, I_{qs}, I_{dr}, I_{qr}, I_{d1}, I_{q1}, I_{d2}, I_{q2}, V_{ds}, V_{qs}, V_{dc}, V_{qc}
λ_4	$-24.067 \pm j376.67$	I_{ds}, I_{qs}, I_{dr}, I_{qr}, I_{d2}, I_{q2}
λ_5	$-7.5794 \pm j94.595$	I_{ds}, I_{qs}, I_{dr}, I_{qr}, I_{d1}, I_{q1}, I_{d2}, I_{q2}, V_{dc}, V_{qc}, s_g
λ_6	$-5.8228 \pm j17.499$	I_{ds}, I_{qs}, I_{dr}, I_{qr}, I_{d1}, I_{q1}, V_{qc}, s_g
λ_7	-11.297	I_{ds}, I_{qs}, I_{dr}, I_{qr}

Table 5.3: Eigenvalues of modified IEEE-SBM with IG2 for 60% series compensation.

$\boldsymbol{\lambda_i}$	$\boldsymbol{-\sigma \pm j\omega}$	**Participating States**
λ_1	$-36.005 \pm j1557.7$	I_{ds}, I_{qs}, I_{dr}, I_{qr}, I_{d1}, I_{q1}, I_{d2}, I_{q2}, V_{ds}, V_{qs}, V_{dc}, V_{dc}
λ_2	$-60.742 \pm j802.89$	I_{ds}, I_{qs}, I_{dr}, I_{qr}, I_{d1}, I_{q1}, I_{d2}, I_{q2}, V_{ds}, V_{qs}
λ_3	$-14.089 \pm j650.26$	I_{ds}, I_{qs}, I_{dr}, I_{qr}, I_{d1}, I_{q1}, I_{d2}, I_{q2}, V_{ds}, V_{qs}, V_{dc}, V_{qc}
λ_4	$-21.495 \pm j375.84$	I_{ds},I_{qs},I_{dr},I_{qr},I_{d2},I_{q2}
λ_5	$\mathbf{3.081 \pm j105.54}$	I_{ds}, I_{qs}, I_{dr}, I_{qr}, I_{d1}, I_{q1}, I_{d2}, I_{q2}, V_{ds}, V_{qs}, V_{dc}, V_{dc}, s_g
λ_6	$-23.434 \pm j25.302$	I_{ds}, I_{qs}, I_{dr}, I_{qr}, I_{d1}, I_{q1}, V_{qc}, s_g
λ_7	-39.378	I_{ds}, I_{qs}, I_{dr}, I_{qr}, I_{d1}, I_{q1}, V_{dc}, V_{qc}, s_g

The linearized equations were cast in the form $[M_c][\Delta\dot{X} = [A_c]\Delta X$ and the Jacobian matrix $[J]$ is computed as $[J] = [Mc]^{-1}[A_c]$. Eigenvalues of the Jacobian matrix are computed and plotted on the complex plane to observe the movement of eigenvalues of the system when the degree of series compensation K_c given by equation (5.18) is chosen as the bifurcation parameter.

$$K_c = \frac{X_c}{X_t + X_1 + X_g} \tag{5.18}$$

Two different induction generators are considered in this study. The first generator will be denoted by IG1 which has the same parameters as that of the SCIG considered in Chapter 3. A second induction generator (which will be referred to as IG2) with a different set of

Table 5.4: Participation factors of λ_{cr} with IG2 at 60% compensation.

I_{ds}	I_{qs}	I_{dr}	I_{qr}	I_{d1}	I_{q1}	V_{dc}	V_{qc}
0.229	0.212	0.227	0.208	0.026	0.026	0.032	0.032

parameters is also considered in this analysis. Parameters of IG1 and IG2 are listed in Tables A.1 and A.2 respectively in A. Parameters of the electrical network except that of the double circuit line can be found in Table 5.1. Eigenvalues of the system under study with IG1 and IG2 for an X/R ratio of 15 for lines 1 and 2 in the double circuit ($X_1/R_1 = X_2/R_2 = 15$) with $R_1 = R_2 = 0.04$ pu and a wind speed of 10 m/s have been listed in Tables 5.2 and 5.3 respectively. The series compensation considered is 60% which is realistic for a weak interconnection. From Table 5.2, it is obvious that the system is stable with IG1 as all eigenvalues have negative real parts. However, in Table 5.3, λ_5 is found to have a real part which is positive resulting in an unstable system. This makes λ_5 the critical mode λ_{cr} and the participation factors corresponding to the dominant states for λ_{cr} are listed in Table 5.4.

Among the 13 eigenvalues of the system, there are 6 complex conjugate pairs (λ_1 to λ_6) and 1 real eigenvalue (λ_7). The frequencies of λ_1 to λ_3 are greater than system frequency among which λ_1 and λ_2 correspond to the modes which arise due to the interaction of induction generator currents with the shunt capacitor voltage. The other eigenvalue pair which has a frequency greater than the system frequency (λ_3) corresponds to the modes produced due to interactions of generator currents with the series capacitor voltage. There is one mode which has a frequency very close to the system frequency (λ_4) which has highest participation from the generator currents and currents flowing in line 2 (uncompensated line) of the double circuit. There are 2 modes in the subsynchronous frequency range (λ_5,λ_6) among which λ_5 is the critical mode as it becomes unstable as the compensation exceeds a certain limit. The other subsynchronous mode (λ_6) is dominated by the d-axis components of the generator currents and slip while the real eigenvalue (λ_7)

has highest participation from the q-axis components of the generator currents and slip of the induction generator.

5.3.1 Eigenvalues of the system for low and high wind speeds

Table 5.5: Critical eigenvalues for different wind speeds

V_w	K_{cr}	$\lambda_{cr} = -\sigma \pm j\omega$	Participating States
9	82%	$0.413 \pm j45.958$	I_{ds},I_{qs},I_{dr},I_{qr},I_{d1},I_{q1},V_{dc},V_{qc},s_g
10	82%	$0.3079 \pm j45.832$	
11	82%	$0.1695 \pm j45.690$	
12	83%	$0.8255 \pm j43.600$	

Table 5.6: Critical eigenvalues for different wind speeds

V_w	K_{cr}	$\lambda_{cr} = -\sigma \pm j\omega$	Participating States
9	52%	$0.2996 \pm j123.37$	I_{ds},I_{qs},I_{dr},I_{qr},I_{d1},I_{q1},I_{d2},I_{q2},V_{dc},V_{qc},s_g
10	52%	$0.1147 \pm j123.26$	
11	53%	$0.2095 \pm j120.82$	
12	54%	$0.2212 \pm j118.37$	

Critical eigenvalues of the system at wind speeds from 9 to 12 m/s for the system with IG1 and IG2 are listed in Tables 5.5 and 5.6 respectively. The X/R ratio of the system for both lines was chosen to be 15. The system with IG1 loses stability when compensation exceeds 81% for $V_w = 9, 10, 11$ m/s and 82% for $V_w = 12$ m/s. However, for $V_w = 9, 10$ m/s, the system with IG2 loses stability when the compensation exceeds 51% which is much smaller than the critical value of series compensation compensation of the system with IG1 which means the stability domain of the system with IG2 is smaller. The dominant states in the critical modes are the stator and rotor currents of the induction generator. Since the critical mode arises due to the interaction of generator currents, network currents and the series capacitor voltage, the reason for instability is identified to be SSR. Hence, from the eigenvalue analysis for low and high wind speeds, it is inferred

that the critical value of series compensation depends on the parameters of the generator and in the system with non-radial interconnection to the grid whereas wind speed does not have much influence over the critical value of series compensation.

5.3.2 Eigenvalue analysis for low, medium and high X/R ratios

Eigenvalues are computed for the system with IG1 and IG2 as the series compensation is varied from 1% to 95% and are plotted on the complex plane as shown in Fig. 5.2 for various X/R ratios. The parameters of the network except for the double circuit line are listed in Table 5.1. The resistance of lines 1 and 2 is assumed to be equal to 0.04 pu and the wind speed considered here is 10 m/s. Here, it is assumed that the X/R ratios of lines 1 and 2 are equal ($X_1/R_1 = X_2/R_2$). It can be seen from Fig. 5.2 that for an X/R ratio of 5 which signifies a relatively strong grid, the system with IG1 loses stability at 90% series compensation whereas the system with IG2 remains completely stable as the percentage series compensation is increased from 1% to 95%. When the eigenvalue trajectory of the system is computed for X/R ratio of 10 , the system with IG1 loses stability through a Hopf bifurcation when the compensation exceeds 85%. Similarly, as the X/R ratio of the system was changed to 15, the system with IG1 loses stability as the percentage series compensation becomes greater than 82%.

When the same analysis was performed for the system with IG2, the system loses stability when the compensation percentage exceeds 65% and 52% for X/R ratios of 10 and 15 respectively. Although the stability domain for the system with IG2 was slightly larger than that of the system with IG1 for an X/R ratio of 5 for lines 1 and 2, the system with IG1 has a larger stability domain as the X/R ratio was increased to 10 and then to 15. It has been observed that in the system with an SCIG-WT with IG1 using non-radial interconnection to the grid, a Hopf bifurcation due to SSR still occurs although the stability domain with the non-radial interconnection is larger compared to the system

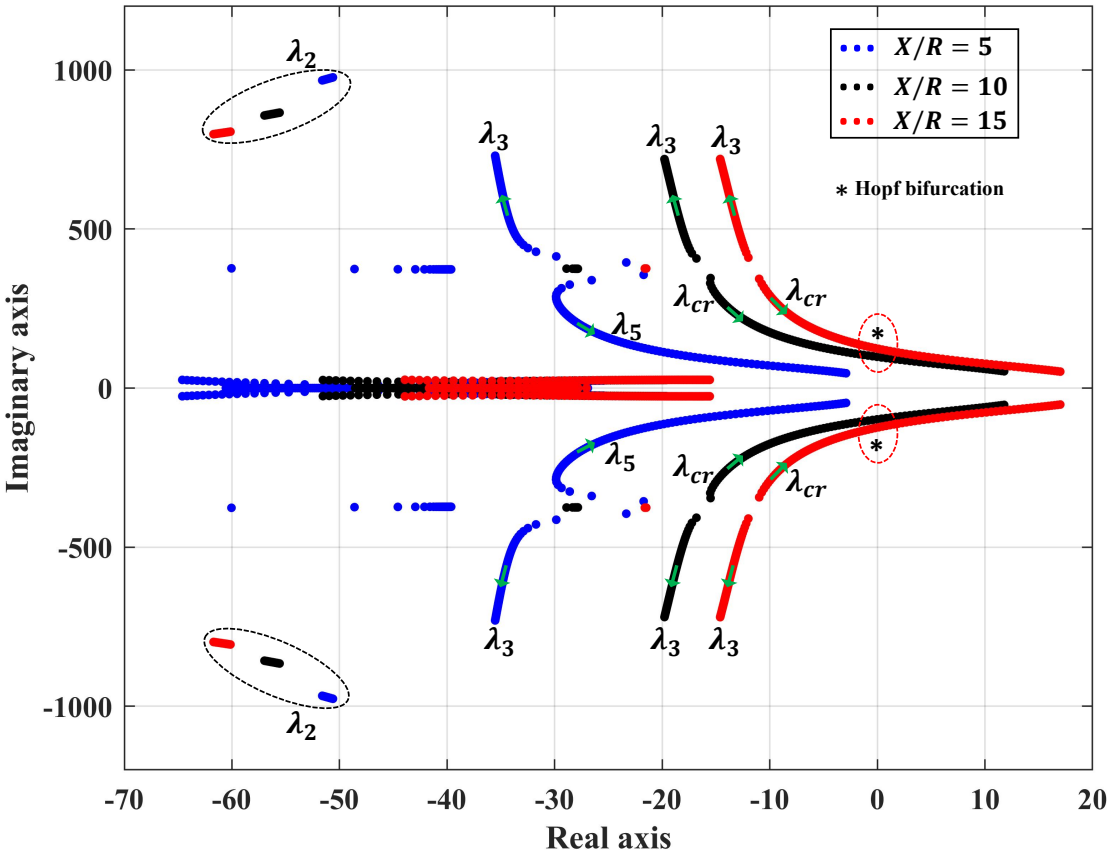

Fig. 5.2: Eigenvalue trajectories for equal X/R ratios with IG2

Table 5.7: Critical eigenvalues of IG1 for equal X/R ratios

X/R ratio	K_{cr}	$\lambda_{cr} = -\sigma \pm j\omega$	Participating states
5	90%	$0.325 \pm j26.94$	I_{ds},I_{qs},I_{dr},I_{qr},I_{d1},I_{q1},I_{d2},I_{q2},V_{dc},V_{qc},s_g
10	85%	$0.152 \pm j39.256$	I_{ds},I_{qs},I_{dr},I_{qr},I_{d1},I_{q1},V_{dc},V_{qc},s_g
15	82%	$0.308 \pm j45.832$	

using a radial interconnection. It has also been observed that the stability domain with respect to series compensation depends on the generator parameters as well since the system with IG2 has a smaller stability domain compared to that of the system with IG1 when connected to the same network for X/R ratios of 10 and 15.

Table 5.8: Critical eigenvalues of IG2 for equal X/R ratios

X/R ratio	$\boldsymbol{K_{cr}}$	$\boldsymbol{\lambda_{cr} = -\sigma \pm j\omega}$	**Participating states**
5	–	–	–
10	65%	$0.388 \pm j96.347$	I_{ds},I_{qs},I_{dr},I_{qr},I_{d1},I_{q1},I_{d2},I_{q2},V_{dc},V_{qc},s_g
15	52%	$0.115 \pm j123.23$	

5.4 Time domain simulations

The non-linear dynamic model of the system described by equations (2.30), (2.31), (2.38) and (5.1) to (5.8) is programmed using MATLAB-SIMULINK and the responses of various system variables are observed when the system is subject to disturbances. Two kinds of disturbances are considered here - the first one is a momentary decrease in the grid voltage to 0.85 pu from 1 pu lasting for 0.1 seconds and the other disturbance is the loss of the uncompensated line in the double circuit. A wind speed of 10 m/s is considered and $\frac{X_1}{R_1} = \frac{X_2}{R_2} = 15$ for a line resistance $R_1 = R_2 = 0.04$ pu. The values of other parameters of the network can be found in Table 5.1 and the parameters of IG2 listed in Table A.2 are considered for the SCIG. Series compensation K_c (defined in equation (5.18)) of 55% is considered.

5.4.1 Response to a disturbance in the grid voltage

The responses of stator voltage magnitude, line current magnitude, real power at the generator terminals and the rotor speed of the induction generator to a momentary decrease in the grid voltage are shown in Figs. 5.3 to 5.6. The system is observed to be unstable as K_c is greater than the critical value for the given operating conditions which confirms the findings from the eigenvalue analysis. Stator voltage magnitude plotted in Fig. 5.3 shows a decrease between 1 and 1.1 seconds as the disturbance persists. As the disturbance is removed at 1.1 seconds, the stator voltage gradually starts building up and

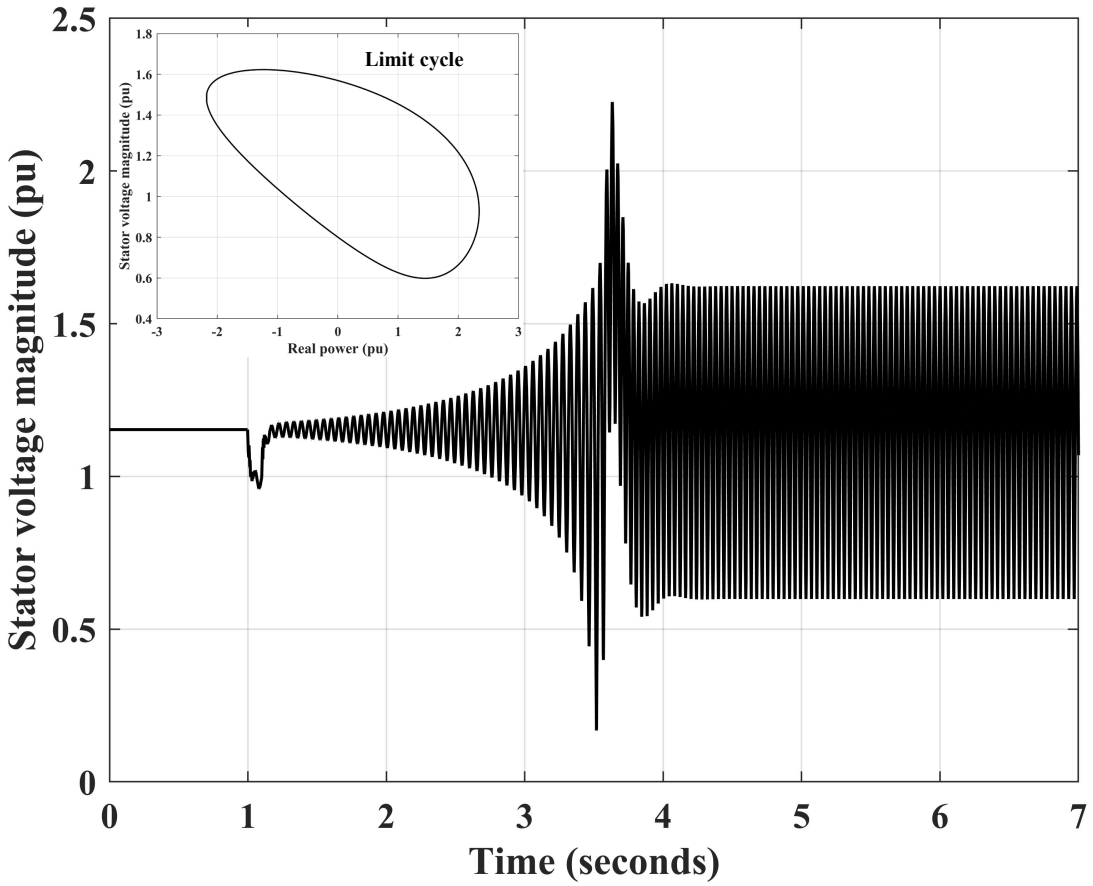

Fig. 5.3: Stator voltage response to a disturbance in grid voltage

reaches a high value of almost 2.22 pu at 3.63 seconds followed by which the oscillations start reducing in amplitude till 3.8 seconds. Beyond 3.8 seconds, there is a slight increase in the magnitude of oscillations lasting for a few cycles as the system transitions to an oscillatory state where the oscillations in the stator voltage are bounded between 0.6 pu and 1.6 pu past 4.2 seconds. This is a result of the limit cycle as a consequence of the Hopf bifurcation due to SSR. These bounded oscillations (between 1.38 pu and 3.08 pu) are also observed in the magnitude of line current in Fig. 5.4. Bounded oscillations between -2.19 pu and 2.85 pu are observed in the real power transmitted from the stator terminals to the grid which implies that power is continuously being transferred back and forth between the stator terminals and the grid when the system enters an oscillatory state.

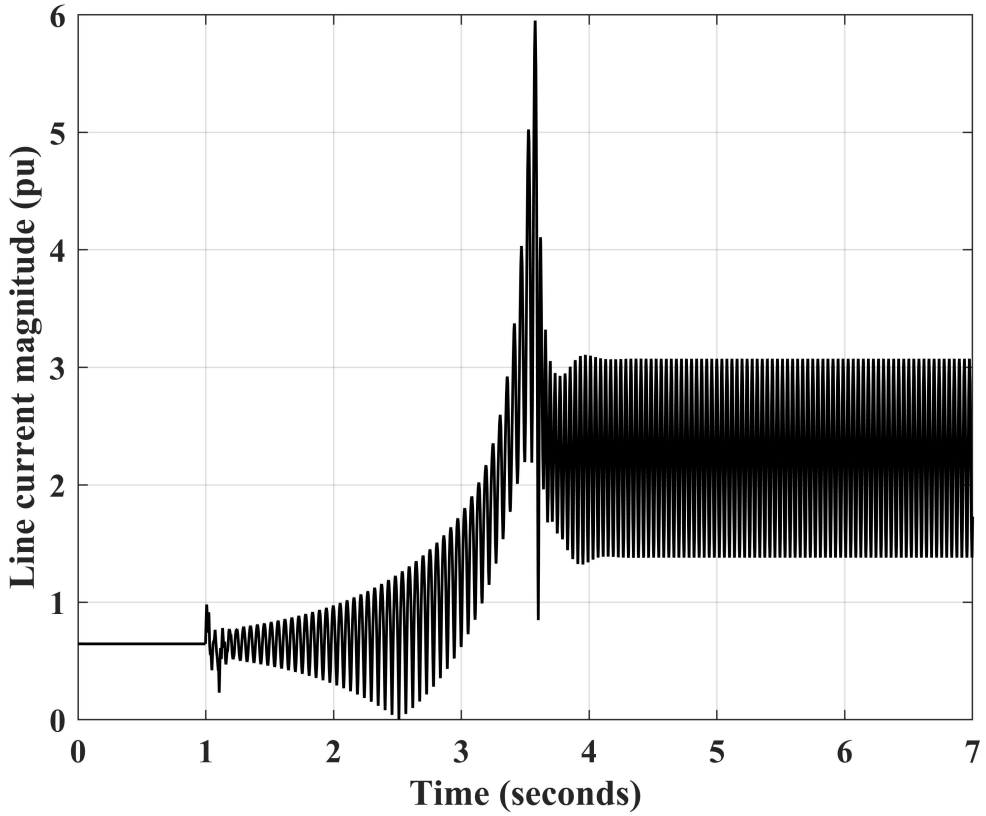

Fig. 5.4: Line current response to a disturbance in grid voltage

Rotor speed of the induction generator in Fig. 5.6 shows oscillations of small amplitude around the equilibrium point (1.014 pu) intially. However, between 3.5 and 3.6 seconds, the rotor speed of the induction generator reduces rapidly causing it to stall. Beyond 3.6 seconds, the speed of the generator recovers slightly before entering an oscillatory state where generator speed oscillates between 0.57 pu and 0.63 pu beyond 4.2 seconds. These bounded oscillations in the system states are manifested as a limit cycle in the phase-plane of the rotor speed shown in Fig. 5.7 and in the characteristics of the voltage plotted with respect to real power at the stator terminals of the SCIG which can be seen in 5.3.

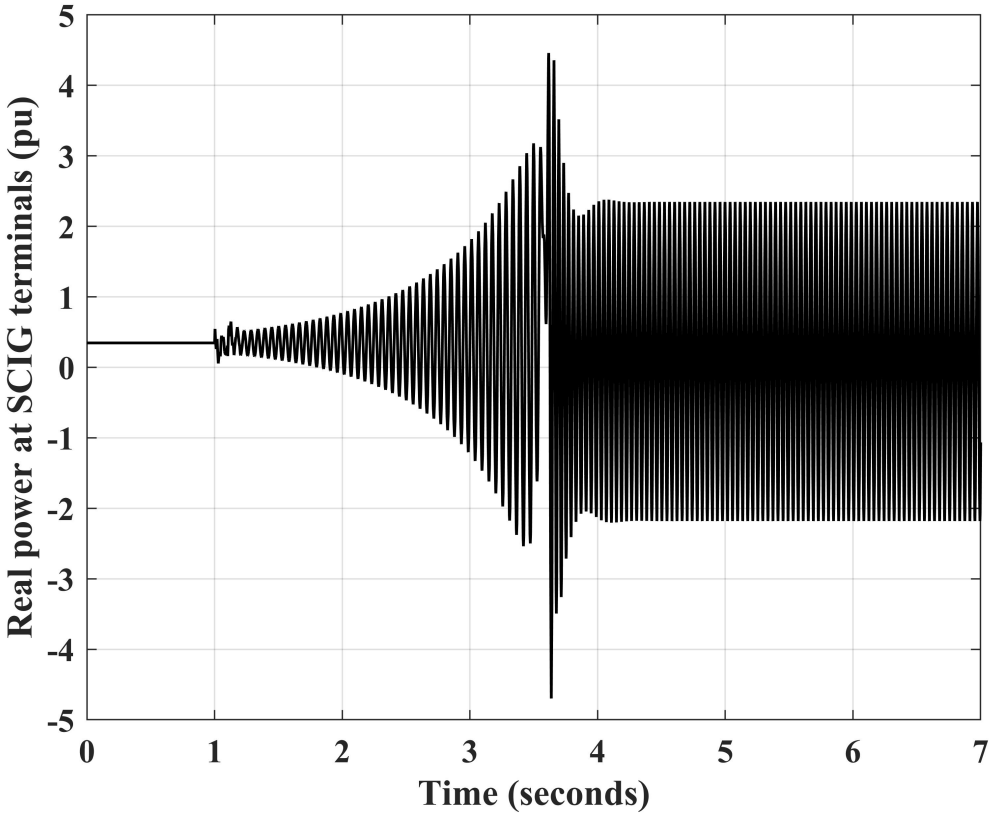

Fig. 5.5: Real power response to a disturbance in grid voltage

5.4.2 Response to a loss of a line in the double circuit

The phase - plane trajectory of the rotor speed when the system is subjected to the loss of the uncompensated line in the double circuit at 1 second is shown in 5.8. The response is similar to that of the previous case where stalling of the SCIG occurs after undergoing a few cycles of oscillations around the equilibrium point. The rotor speed goes slightly below synchronous speed at 1.35 seconds beyond which it decreases rapidly. After about 3 seconds, the system enters an oscillatory state where the oscillations in the rotor speed are bounded between 0.2 and 0.4 pu. On the phase plane, the trajectory starts spiraling outwards from the equilibrium point and is pulled towards the limit cycle shown in Fig. 5.8.

The plot of the stator voltage at the SCIG terminals with respect to time (Fig. 5.9) reveal

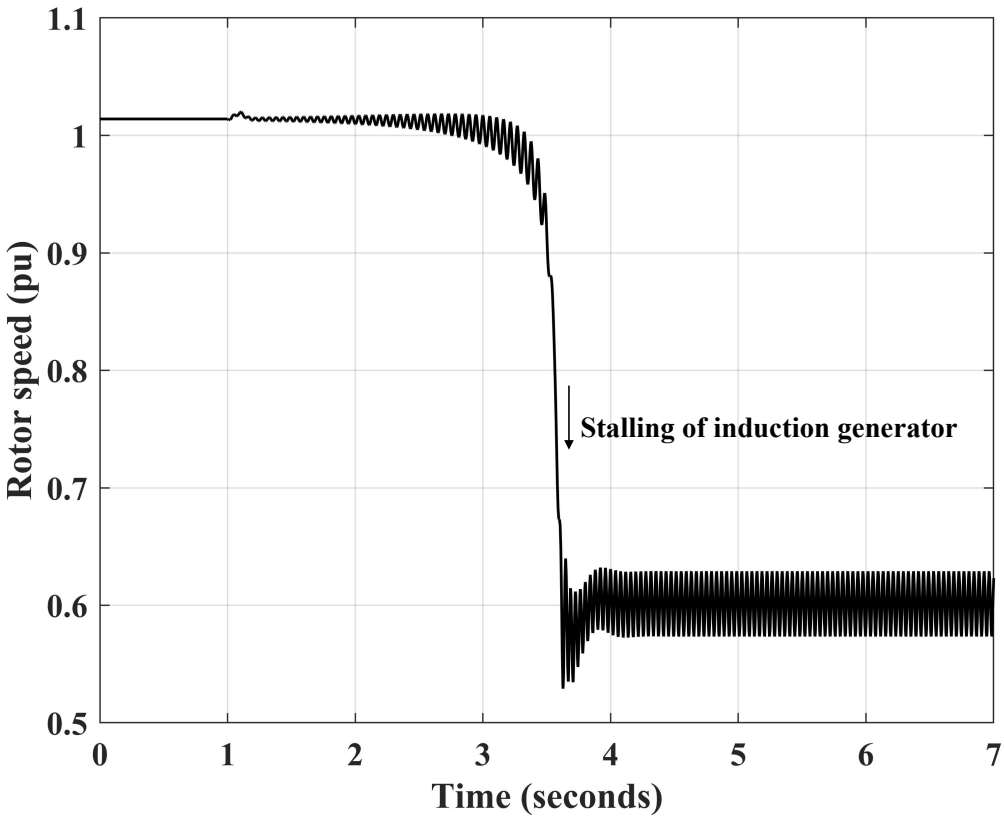

Fig. 5.6: Rotor speed response to a disturbance in grid voltage

a much larger overvoltage when the system enters the oscillatory state as the oscillations in the voltage are bounded between 2.34 pu and 3.05 pu between 3.5 and 4 seconds. In practice, the protection system would be triggered immediately within a few cycles when the voltage oscillations start when the disturbance is encountered resulting in tripping of the SCIG. The dynamic P-V characteristics reveal that the trajectory starting at the equilibrium point diverges away from it, moving towards the limit cycle when the system undergoes the loss of the uncompensated line which is shown in Fig. 5.10. The periodic solutions of the stator voltage with respect to the reactive and real power at the stator terminals are also shown in Figs. 5.9 and 5.10.

The instantaneous stator voltage of phase A along with it's frequency spectrum is computed for the case when the system is subjected to a momentary disturbance in the grid voltage as well as when the system is subjected to the loss of the uncompensated line

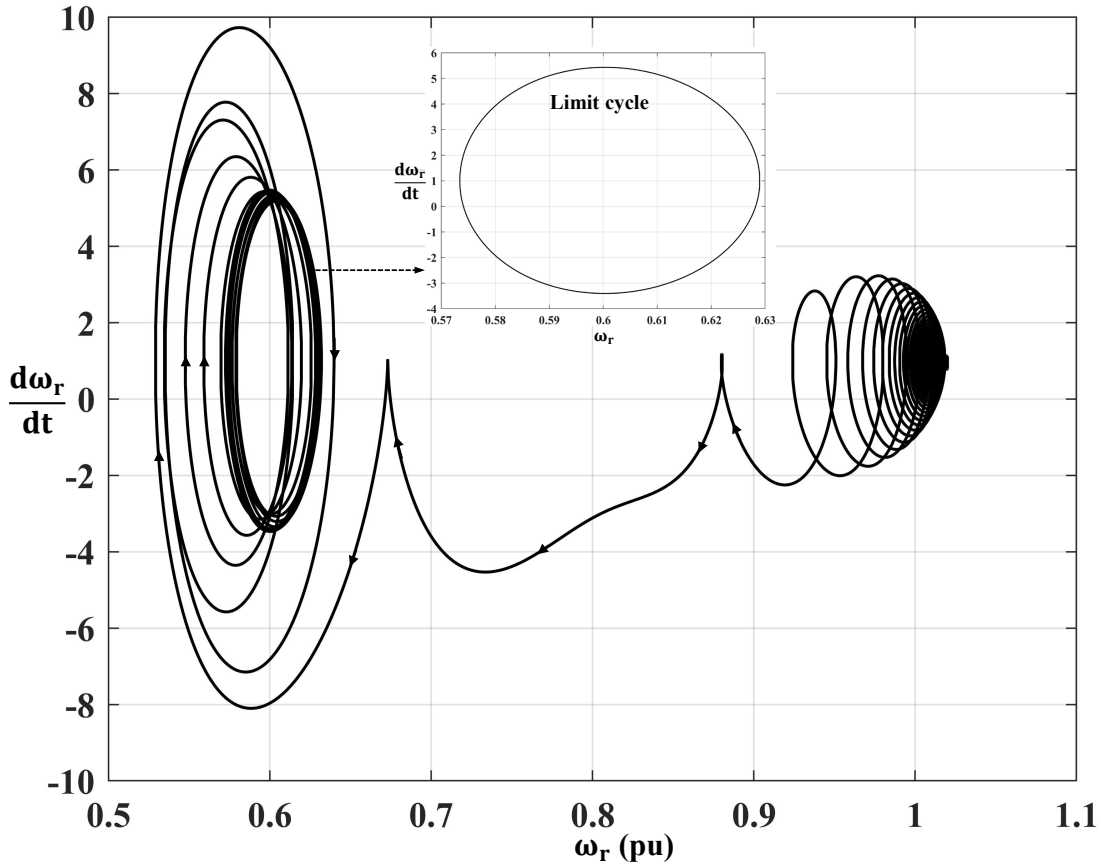

Fig. 5.7: Phase plane trajectory when subjected to a disturbance in grid voltage

in the double circuit. The waveforms are shown past 5 seconds which corresponds to the time past which the system enters an oscillatory state due to the limit cycle. From Fig. 5.11, 35 Hz component is observed to be dominant followed by a 60 Hz component and the maximum amplitude of the voltage is found to be almost 1.7 pu. However, an instantaneous voltage of approximately 3 pu can be observed when the system is subjected to the loss of the uncompensated line. The frequency spectrum in this case shows a dominant 18 Hz component. This is followed by small contributions from 25 Hz and 60 Hz components. Hence, in both cases, a subsynchronous frequency component dominates the stator voltage when the system exhibits oscillatory behavior. The frequency spectrum of the line current in phase A shown in Fig. 5.12 reveals a dominant 60 Hz component for both types of disturbances considered followed by a 35 Hz component

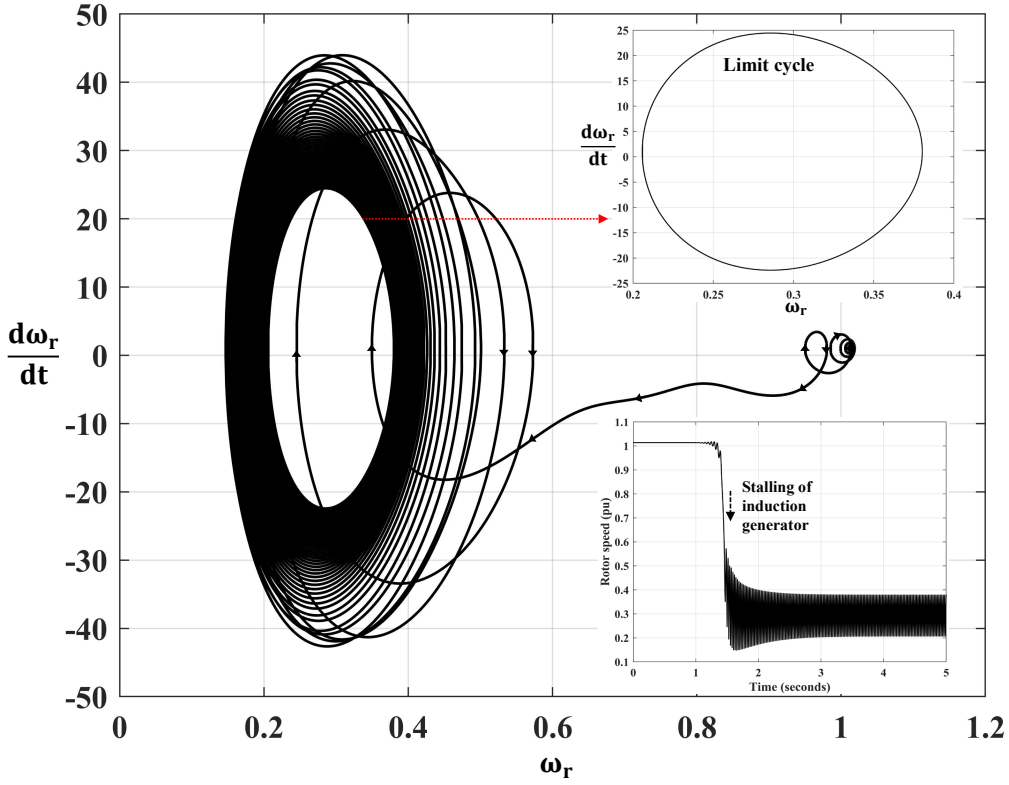

Fig. 5.8: Phase - plane trajectory with respect to rotor speed for the loss of a line

when the system undergoes a disturbance in the grid voltage momentarily and an 18 Hz component when the uncompensated line is lost. The frequency components depend on the type of disturbance which the system is subject to.

5.5 Conclusion

In this chapter, the dynamic modeling, eigenvalue analysis and detailed time domain simulation results for the IEEE second benchmark model has been presented. For systems with non-radial interconnections as this, it was concluded that there is no possibility of subsynchronous resonance in [63]. However, this cannot be generalized for systems with non-radial interconnections as in this chapter, an SCIG-WT connected to the grid through a double circuit line still experiences instabilities due to subsynchronous resonance. An SCIG-WT with a non-radial interconnection may possess a larger stability domain with

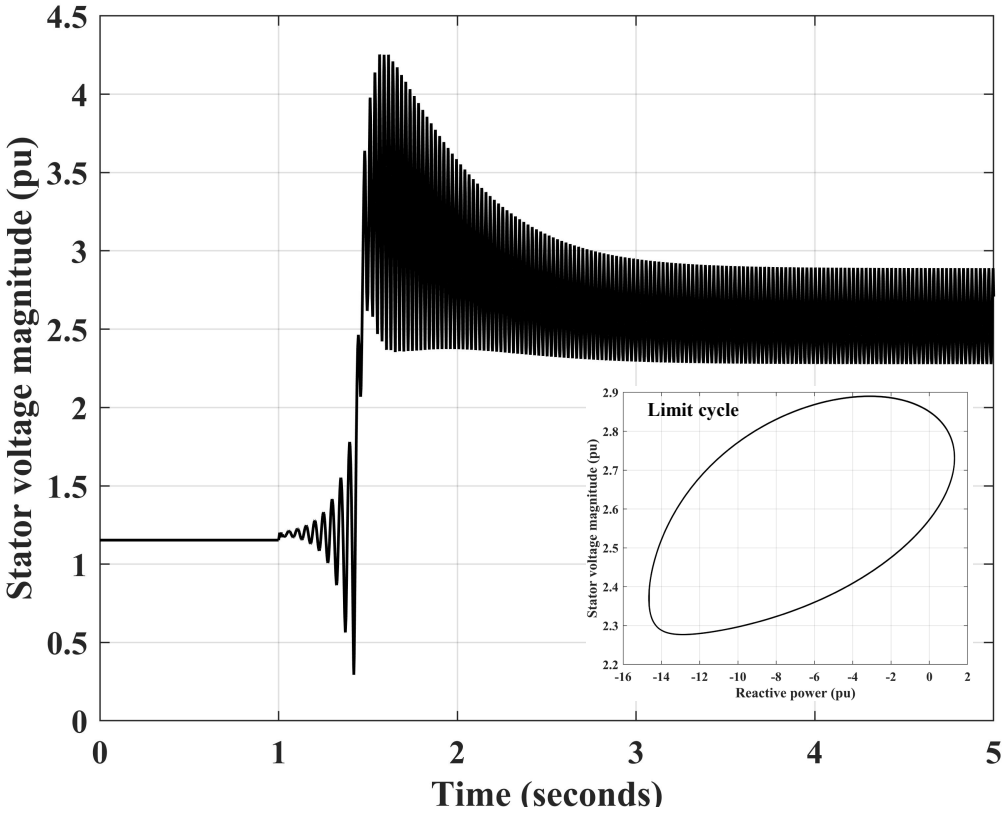

Fig. 5.9: Stator voltage response when system experiences loss of a line

respect to series compensation compared to the same SCIG-WT in a radial interconnection to the grid. As the grid becomes weaker for higher X/R ratios, the system loses stability through a Hopf bifurcation for smaller values of percentage series compensation. The Hopf bifurcation point also depends on the parameters of the induction generator but is not affected very much for different wind speeds. Time domain simulations are performed using SIMULINK software considering a momentary reduction in the grid voltage and loss of the uncompensated line in the double circuit. From the results of the time domain simulation, the nature of the Hopf bifurcation is found to be sub-critical as the system significantly diverges away from the equilibrium point. The frequency components in the periodic solutions of various system variables depends on the type of disturbance which the system undergoes. Hence, network topologies have a significant impact on the stability domain of series compensated systems which makes detailed dynamic modeling

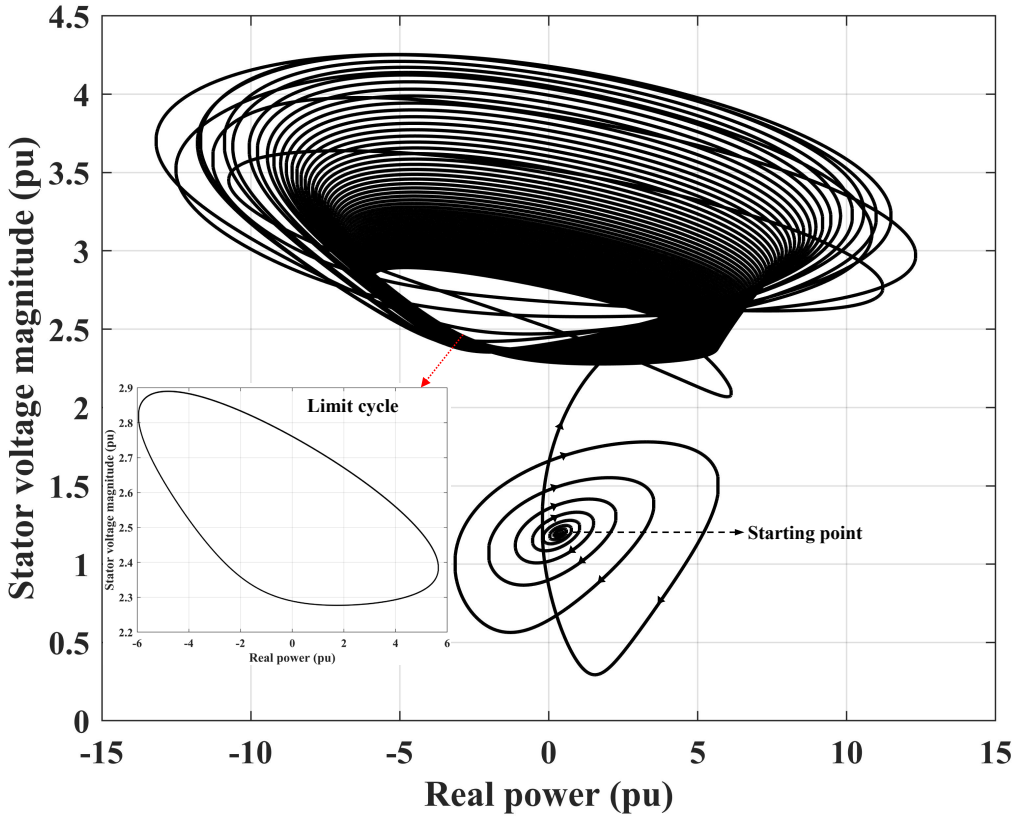

Fig. 5.10: P-V characteristics when system experiences loss of a line

and stability studies highly important while planning a power system. In the next 2 chapters, the impact of series compensation on dynamic loads namely induction motors will be explored.

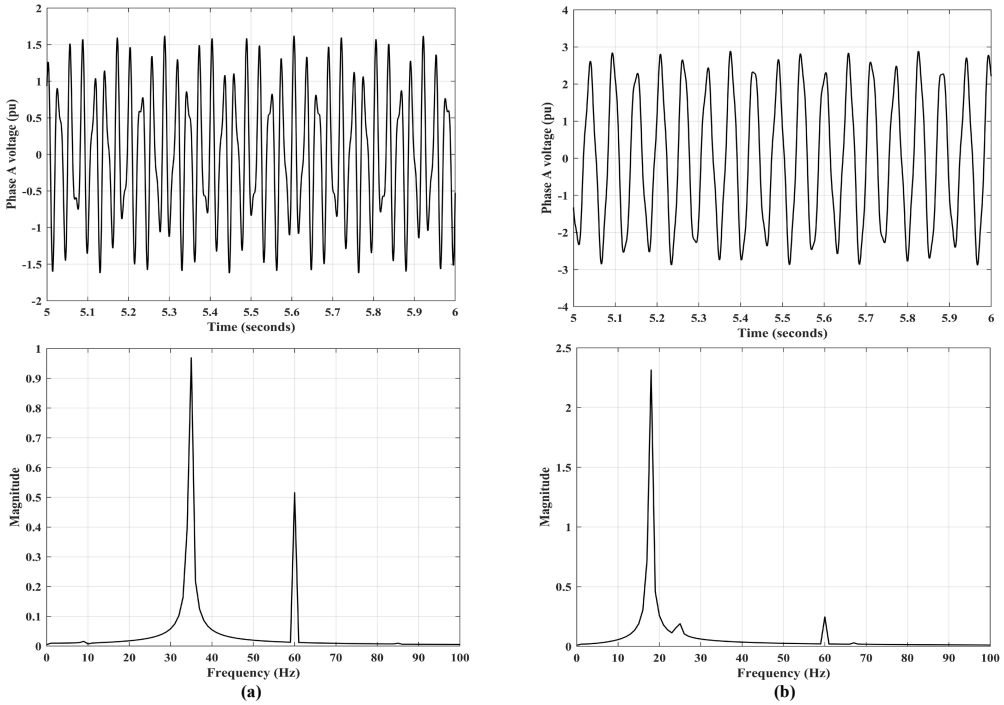

Fig. 5.11: Instantaneous stator voltage of phase A with the corresponding frequency spectrum for the system with (a) Grid voltage disturbance (b) Loss of uncompensated line

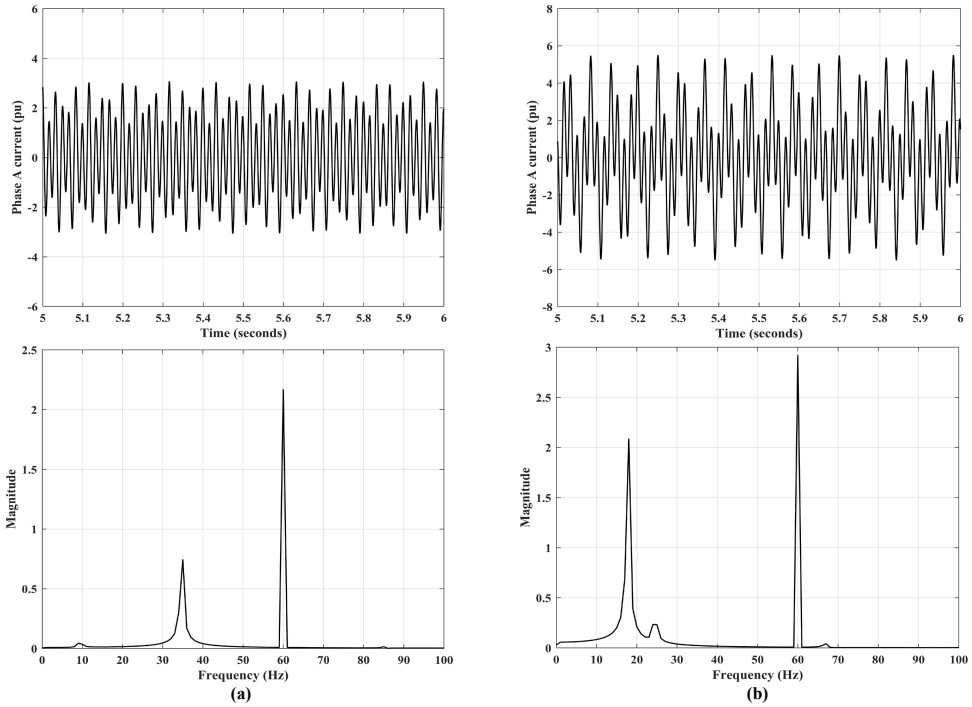

Fig. 5.12: Instantaneous stator voltage of phase A with the corresponding frequency spectrum for the system with (a) Grid voltage disturbance (b) Loss of uncompensated line

CHAPTER 6

Stability Domain Analysis of Power Systems with Induction Motor Loads supplied through Weak Interconnections

In this chapter, the dynamic modeling and stability domain analysis of a system consisting of an induction motor load supplied supplied through a series compensated feeder has been presented. The topology of the network is affected by the presence of dynamic loads such as induction motors which impacts the stability of the system. Induction motors are utilized in a wide variety of industrial applications like steel rolling mills, compressors, elevators, etc due to it's rugged construction, high efficiency and low maintenance ([64], [65]). These motor loads are supplied using soft starters to minimize the effects like high starting currents in the system leading to higher voltage drops. However, as the motor picks up speed, the starter is bypassed and full line voltage appears across the motor terminals under steady state. In this chapter, the stability of the system with induction motor loads supplied through a series compensated network is studied when the motor is perturbed from it's steady state operating point.

It is very important to understand the impact of these loads on the performance of the power system especially if the interconnection is weak. The steady state stable operating region on the torque-slip characteristics of the induction motor is limited by the impedance of the network in addition to the motor parameters. Series capacitors can be used to enhance the stable operating range of the motor by compensating a part of the reactance of the feeder, thus enabling the motor to operate at a higher slip to supply greater load torques. However, series compensation impacts the dynamic stability of the system when the motor is perturbed from its steady state operation leading to

instabilities. The main goal of this work is to reveal bifurcations which arise in these systems as a result of the weak interconnection between the source and load. The impact of X/R ratio of the feeder and induction motor loading on the stability domain with respect to series compensation has been examined through eigenvalue analysis.

6.1 Mathematical modeling of system

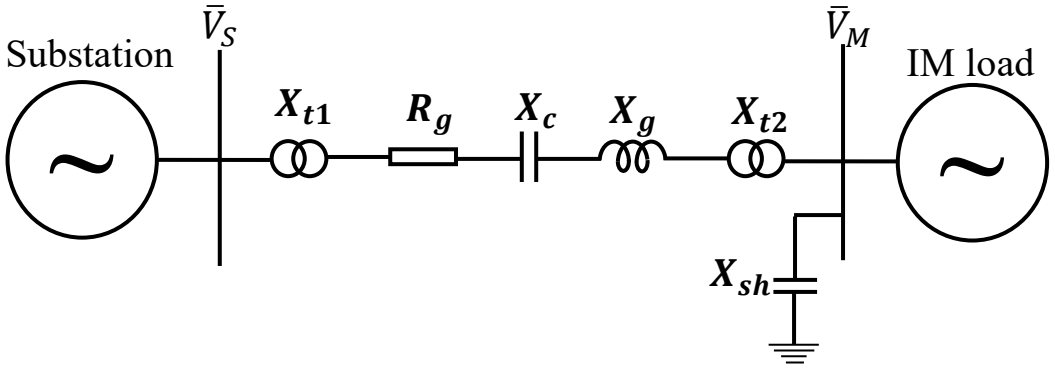

Fig. 6.1: Single line diagram of system

The single line diagram of system under study is shown in Fig. 6.1. The induction motor load is fed from a substation directly through a series compensated feeder. The induction motor also has a shunt capacitor at its terminals to provide reactive power compensation. The dynamic equations of the d and q components of the network currents are given by:

$$\frac{X_{net}}{\omega_s}\frac{d}{dt}\{I_n\} = -[Z_N]\{I_n\} - \{V_c\} - \{V_s\} + \{V_g\} \tag{6.1}$$

where $[Z_N] = [Z_{T1} + Z_G + Z_{T2}]$, $X_{net} = X_{t1} + X_g + X_{t2}$ and

$$[Z_{T1}] = \begin{bmatrix} R_{t1} & -X_{t1} \\ X_{t1} & R_{t1} \end{bmatrix}, [Z_G] = \begin{bmatrix} R_g & -X_g \\ X_g & R_g \end{bmatrix}, [Z_{T2}] = \begin{bmatrix} R_{t2} & -X_{t2} \\ X_{t2} & R_{t2} \end{bmatrix}$$

.

The elements of vectors $\{I_n\}$, $\{V_s\}$ and $\{V_c\}$ are given by:

$$\{I_n\} = [I_{dn} \quad I_{qn}]^T \tag{6.2}$$

$$\{V_s\} = [V_{ds} \quad V_{qs}]^T \tag{6.3}$$

$$\{V_c\} = [V_{dc} \quad V_{qc}]^T \tag{6.4}$$

$$\{V_g\} = [V_{dg} \quad V_{qg}]^T \tag{6.5}$$

The dynamics of the voltage across the series capacitor is modeled using the equation given below:

$$\frac{1}{\omega_s}\frac{d}{dt}\{V_c\} = [Z_{se}]\{I_n\} + [N_1]\{V_c\} \tag{6.6}$$

where $[Z_{se}] = X_c[U]$.

The dynamics of the shunt capacitor voltage at the terminals of the induction motor are described by the following equation:

$$\frac{1}{\omega_s}\frac{d}{dt}\{V_s\} = [Z_{sh}]\{I_n - I_s\} + [N_1]\{V_s\} \tag{6.7}$$

where $[Z_{sh}] = X_{sh}[U]$ and $\{I_s\} = [I_{ds} \quad I_{qs}]^T$ are the d and q components of the stator current of the induction motor.

6.2 Linearization of mathematical model

Linearized versions of dynamic equations (6.1), (6.6) and (6.7) are presented below:

$$\frac{1}{\omega_s}[U]p\{\Delta V_s\} = [N_1]\Delta V_s + [Z_{sh}]\{\Delta I_n - \Delta I_s\} \tag{6.8}$$

$$\frac{1}{\omega_s}[U]p\{\Delta V_c\} = [N_1]\Delta V_c + [Z_{se}]\{\Delta I_n\} \tag{6.9}$$

$$\frac{X_{net}}{\omega_s}[U]p\{\Delta I_n\} = -[Z_{nw}]\{\Delta I_n\} - \{\Delta V_c\} - \{\Delta V_s\} + \{\Delta V_g\} \tag{6.10}$$

In equation (6.10), $\{\Delta V_g\} = 0$ since the voltage of the substation is assumed to be fixed under equilibrium conditions.

6.3 Eigenvalue analysis of system

The complete linearized system model comprises of equations (6.8), (6.9), (6.10) along with (2.39), (2.40) and (2.49). The state variables of the system under study are listed below:

$$\Delta X = \{\Delta I_{ds}, \Delta I_{qs}, \Delta I_{dr}, \Delta I_{qr}, \Delta I_{dn}, \Delta I_{qn}, \Delta V_{ds}, \Delta V_{qs}, \Delta V_{dc}, \Delta V_{qc}, \Delta s_m\}^T \tag{6.11}$$

In this section, eigenvalues of the linearized system are presented for various operating conditions and system parameters as the percentage series compensation $K_c = X_c/X_{net}$ is varied from 1% to 98% where network reactance $X_{net} = X_{t1} + X_g + X_{t2}$ and X_c is the reactance of the series capacitor.

6.3.1 Eigenvalues for base case

For the system under study, eigenvalues are calculated for a slip of 1% for the induction motor and for a feeder of X/R ratio of 15 and are plotted on the complex plane as the percentage series compensation is increased from 1% to 98% which can be seen in Fig.

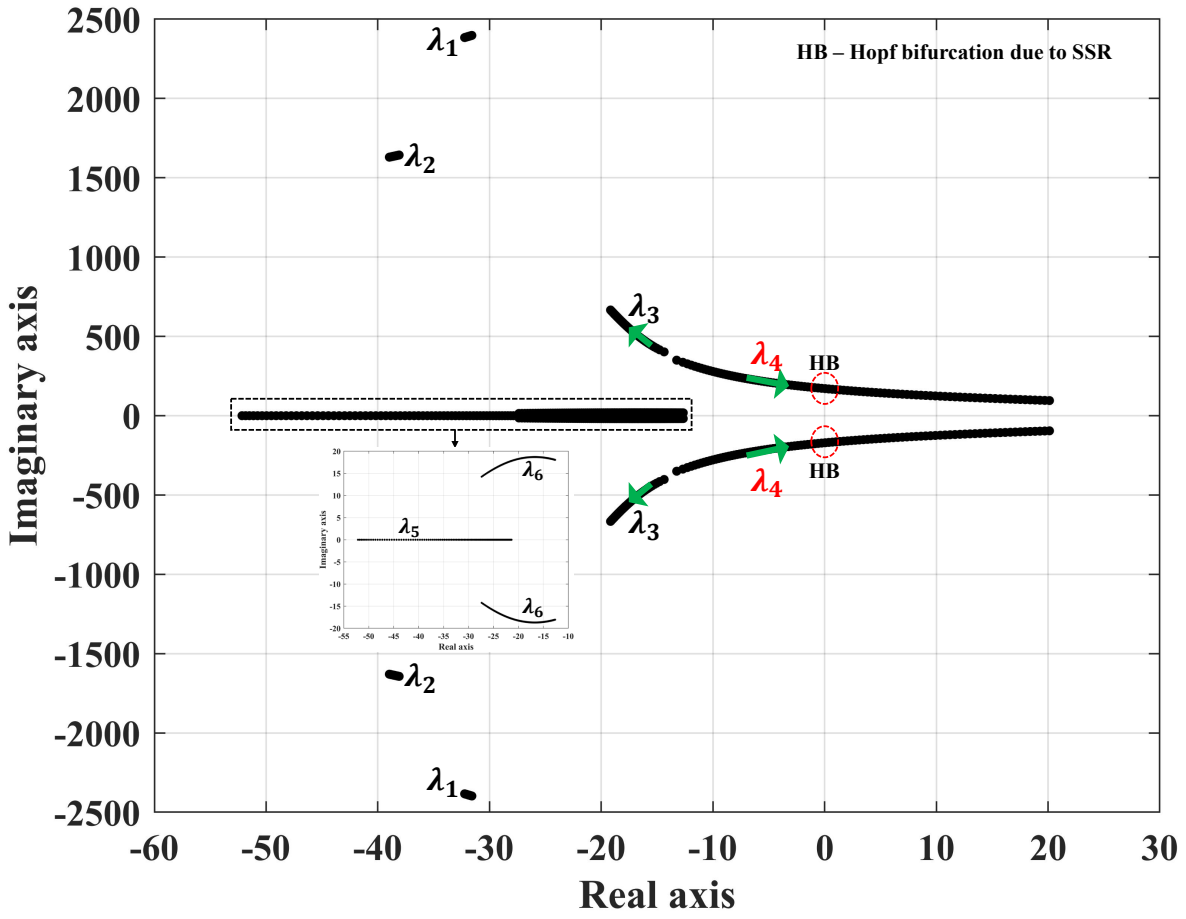

Fig. 6.2: Eigenvalue trajectories for base case

6.2. From the figure, it is observed that there are 5 oscillatory modes (λ_1, λ_2, λ_3, λ_4 and λ_6) characterized by complex conjugate eigenvalues and one non-oscillatory mode (λ_5) characterized by a real eigenvalue. Among the oscillatory modes, 3 modes (λ_1, λ_2, λ_3) have frequencies greater than 60 Hz and 2 modes (λ_4, λ_6) less than 60 Hz. For the entire range of percentage series compensation considered, modes λ_1, λ_2, λ_3, λ_5 and λ_6 are stable. However, mode λ_4 starts moving towards the right half of the complex plane as the percentage series compensation increases. The system loses stability due to a Hopf bifurcation which occurs as a result of λ_4 crossing over from the left to the right half of the complex plane when the percentage series compensation is between 48% and 49%. This makes λ_4 the critical mode which will be referred to as λ_{cr}. Table 6.1 lists the

Table 6.1: Eigenvalues of induction motor load for base case

$\boldsymbol{\lambda_i}$	$\boldsymbol{-\sigma \pm j\omega}$	**Participating States**
λ_1	$-31.904 \pm j2390.8$	I_{dn},I_{qn},I_{ds},I_{qs},I_{dr},I_{qr},V_{ds},V_{qs}
λ_2	$-38.527 \pm j1636.7$	I_{dn},I_{qn},I_{ds},I_{qs},I_{dr},I_{qr},V_{ds},V_{qs}
λ_3	$-18.02 \pm j583.89$	I_{dn},I_{qn},I_{ds},I_{qs}, I_{dr},I_{qr},V_{dc},V_{qc}
λ_4	$0.3674 \pm j168.60$	I_{dn},I_{qn},I_{ds},I_{qs},I_{dr},I_{qr},V_{dc},V_{qc}
λ_5	-32.065	I_{ds},I_{qs},I_{dr},I_{qr}
λ_6	$-18.042 \pm j18.618$	I_{ds},I_{qs},I_{dr},I_{qr},s_m

Table 6.2: Participation factors of λ_{cr} 50% compensation

$\boldsymbol{I_{ds}}$	$\boldsymbol{I_{qs}}$	$\boldsymbol{I_{dr}}$	$\boldsymbol{I_{qr}}$	$\boldsymbol{I_{dn}}$	$\boldsymbol{I_{qn}}$	$\boldsymbol{V_{dc}}$	$\boldsymbol{V_{qc}}$
0.246	0.241	0.242	0.237	0.007	0.006	0.011	0.011

Table 6.3: Critical eigenvalues for different X/R ratios at 1% slip

X/R ratio	$\boldsymbol{K_{cr}}$	$\boldsymbol{\lambda_{cr} = -\sigma \pm j\omega}$	**Participating states**
10	54%	$0.130 \pm j170.2$	I_{dn},I_{qn},I_{ds},I_{qs},I_{dr},I_{qr},V_{dc},V_{qc}
20	46%	$0.094 \pm j170.26$	
30	42%	$0.072 \pm j170.29$	

eigenvalues of the system at 50% series compensation and the participation factors for λ_{cr} have been listed in Table 6.2. Observing the participation factors corresponding to the critical mode, it is obvious that the instability in the system is due to SSR as there is participation from the stator and rotor currents of the motor and the series capacitor voltage.

6.3.2 Eigenvalues at different X/R ratios of the radial feeder

An increase in X/R ratio for a given vaue of resistance reduces the short circuit capacity of the system due to an increase in the impedance of the network as a result of which the strength of the interconnection decreases. Presence of a series capacitor improves the

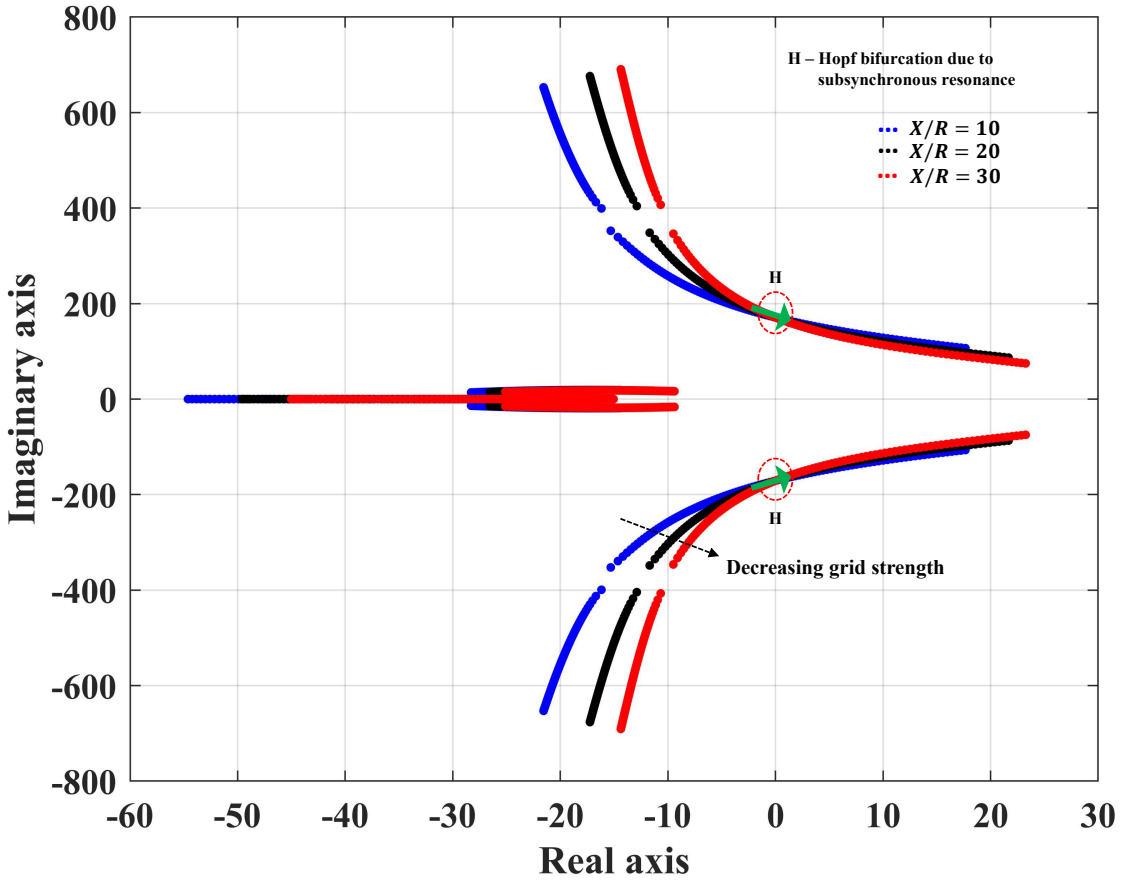

Fig. 6.3: Eigenvalue trajectories at different X/R ratios

Table 6.4: Critical eigenvalues for different X/R ratios at 3% slip

X/R ratio	K_{cr}	$\lambda_{cr} = -\sigma \pm j\omega$	Participating states
10	52%	$0.153 \pm j174.19$	I_{dn},I_{qn},I_{ds},I_{qs},I_{dr},I_{qr},V_{dc},V_{qc}
20	44%	$0.017 \pm j174.9$	
30	41%	$0.247 \pm j172.91$	

short circuit ratio by increasing the short circuit capacity by reducing the net reactance of the system thereby resulting in an increase in the system strength while simultaneously extending the steady state stable operating range of the motor. However, the upper limit of percentage series compensation is determined by the Hopf bifurcation point which is influenced by the X/R ratio of the feeder. Eigenvalues of the linearized system are calculated and plotted on the complex plane which is shown in Fig. 6.3 when the series

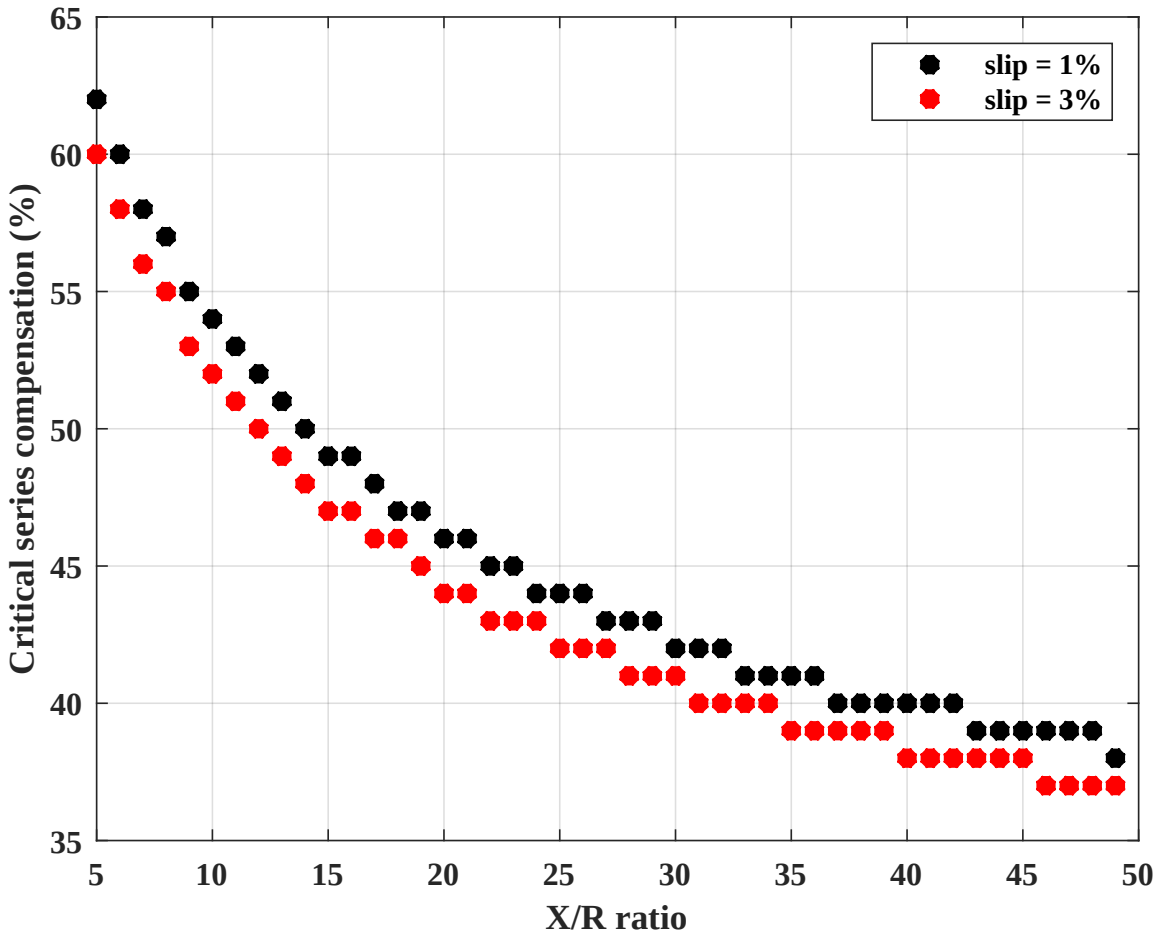

Fig. 6.4: Hopf bifurcation points at different X/R ratios

compensation is varied for X/R ratios of 10, 20 and 30 with the induction motor operating at a slip of 1%. The system with an X/R ratio of 30 becomes unstable at a smaller value of K_c. This means the stability domain of the system with respect to series compensation shrinks as the system becomes weaker due to high values of line impedance. Critical eigenvalues of the system are listed in Table 6.3. When eigenvalue analysis was conducted for a higher slip of 3%, the critical series compensation at which the system becomes unstable is slightly lower for the same X/R ratios considered and this can be observed from Table 6.4 and from Fig.6.4.

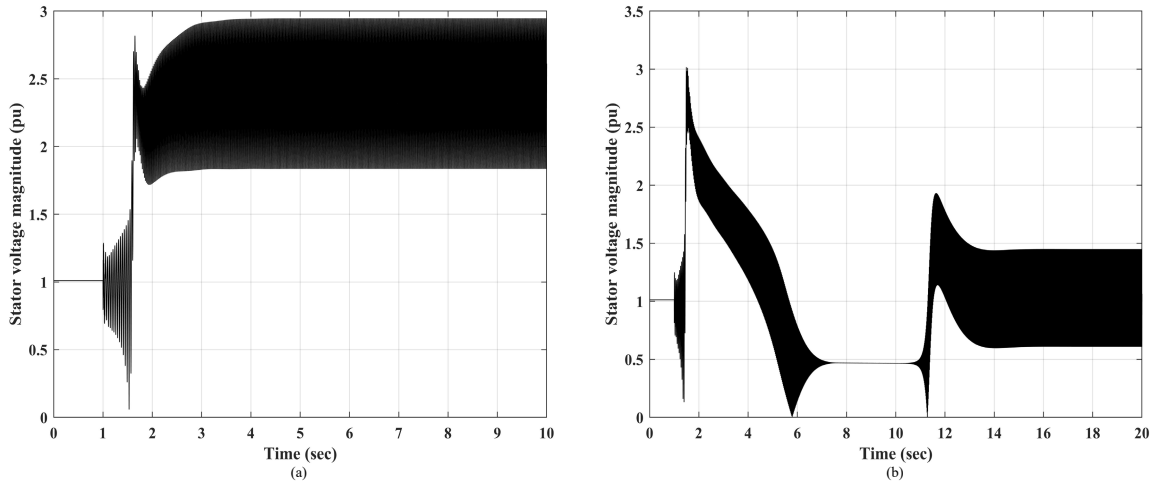

Fig. 6.5: Stator voltage response to a disturbance in grid frequency for (a) X/R ratio of 20 (b) X/R ratio of 30

6.4 Time domain simulation results

The non-linear dynamic equations of the system ((6.1), (6.6), (6.7), (2.24), (2.25) and (2.36)) are programmed in SIMULINK. responses of the system are plotted for a disturbance in the grid frequency injected in the same way as described in Chapter 4 using the exponential function $f(t) = f_o - exp(-\tau t)\sin(\omega_n t)$ where $f_o = 60$ Hz, $\tau = 1.95$, $f_n = 1.2$ Hz and $\omega_n = 2\pi f_n$ rad/s. The series compensation of the system is set at 50% and a slip of 1% is considered for the induction motor. The time responses of the system to a step change in the grid voltage was very similar in shape and hence are not shown here.

The rotor speed of the induction motor is shown in Fig. 6.7 from which it can be observed that when X/R ratio is 20, the rotor speed oscillates around 0.2 pu. However, as the grid becomes weaker with a higher X/R ratio of 30, the rotor speed of the induction motor oscillates at a negative speed of around -0.2 pu. The phase-plane trajectories for the X/R ratios considered are shown in Fig. 6.8. Oscillations in electric torque produced by the motor attain dangerously high values as the motor stalls as a result of subsynchronous oscillations.

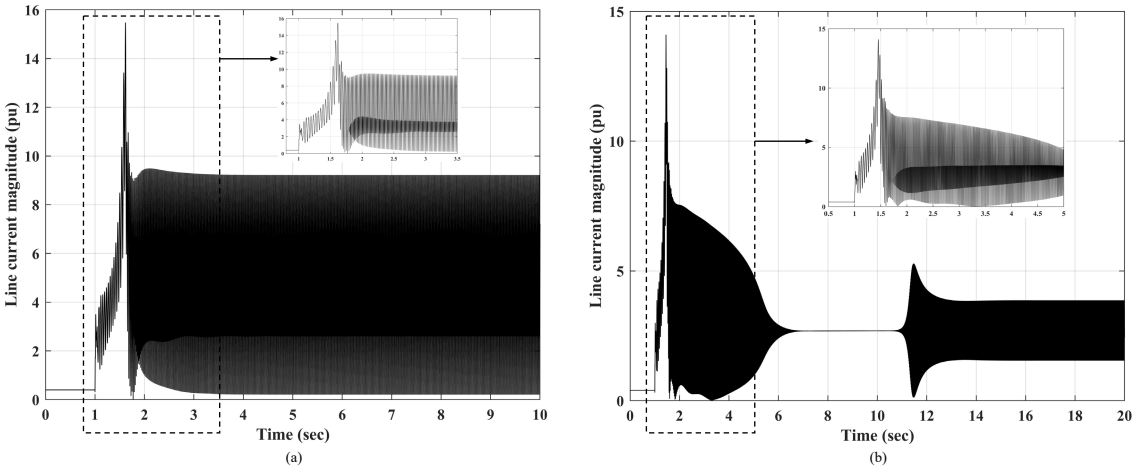

Fig. 6.6: Line current response to a disturbance in grid frequency for (a) X/R ratio of 20 (b) X/R ratio of 30

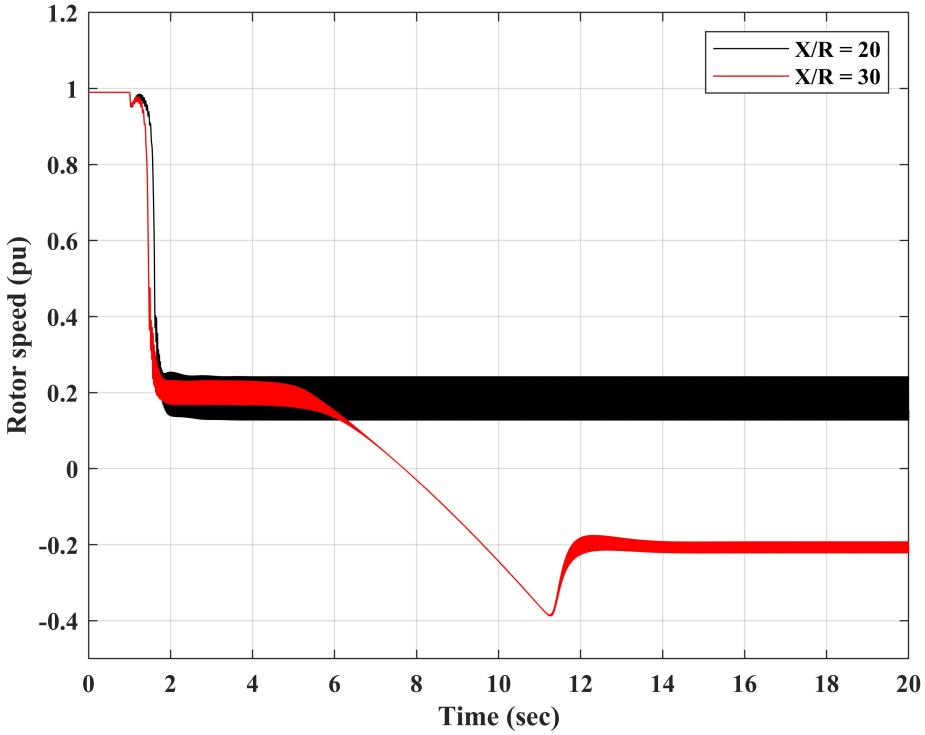

Fig. 6.7: Induction motor speed response to a disturbance in grid frequency

When simulated for a longer period of time, the system was found to enter a state of undamped oscillations which are bounded in magnitude which is the result of the emergence of a limit cycle as a consequence of the Hopf bifurcation. The size of the limit cycle is found to be a function of the X/R ratio of the feeder which is shown in Fig. 6.9.

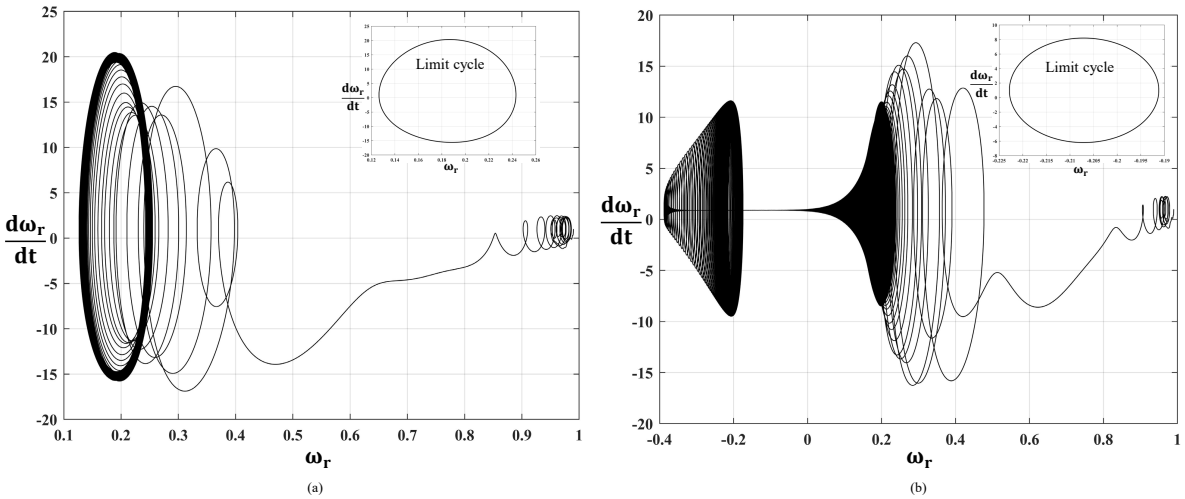

Fig. 6.8: Phase plane trajectory of motor speed in response to a disturbance in grid frequency

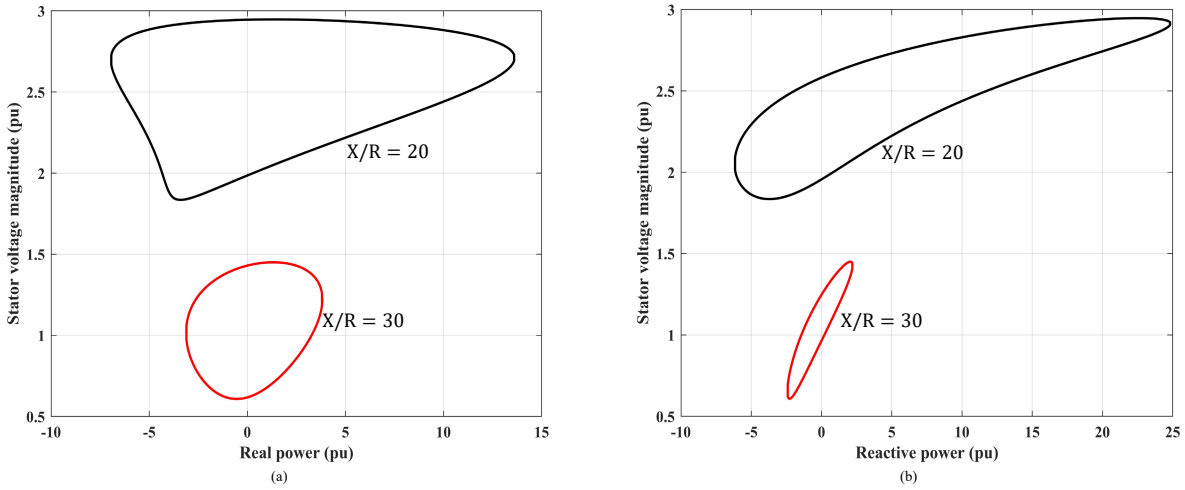

Fig. 6.9: Periodic solutions of P,Q and V for a grid frequency disturbance

The limit cycle was the smallest for the system with X/R ratio of 30 which may be due to a higher voltage drop owing to a greater value of feeder reactance.

The responses of line currents of the system for X/R ratios of 20 and 30 are shown in Fig. 6.6. For both loading conditions, an current magnitude of almost 16 pu has been observed close to 1 second. For a smaller X/R ratio of 20, the line current undergoes oscillations between 0 and 9 pu past 1 second. A double frequency component of the current is seen in the line current waveform during the entire simulation. When the simulation was repeated

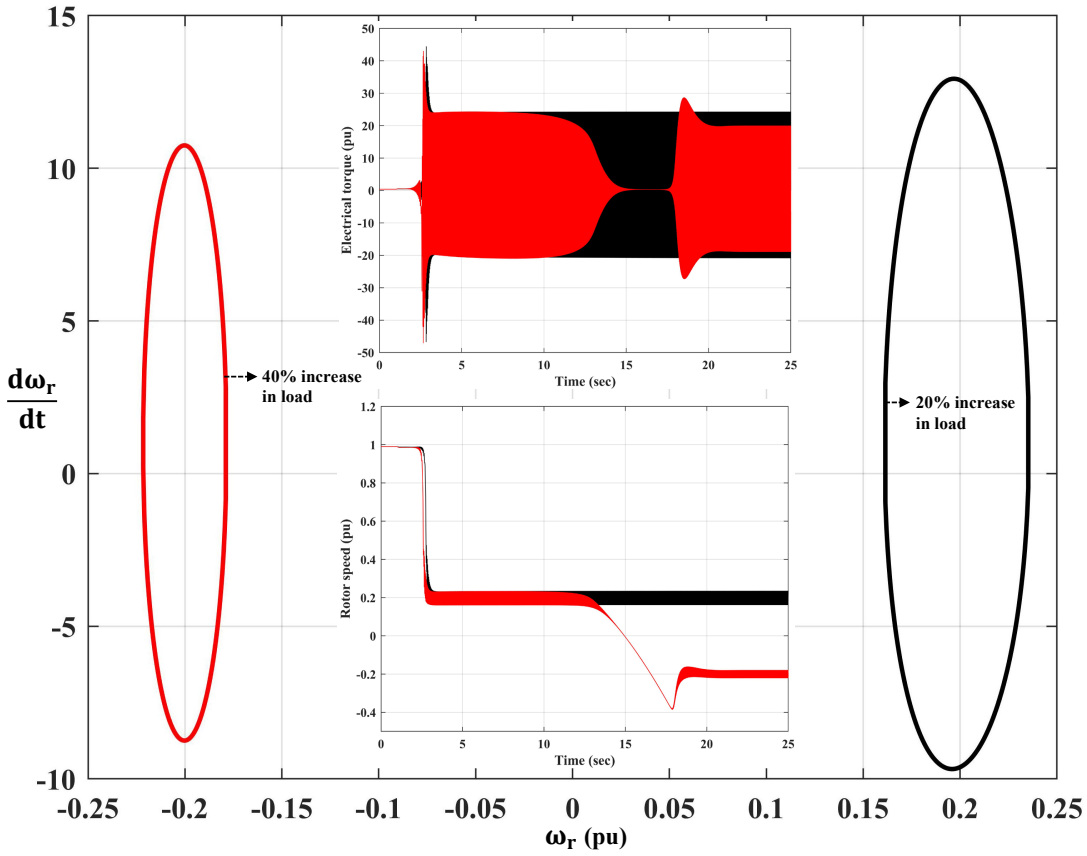

Fig. 6.10: Rotor speed and electrical torque response to a load step change

for a higher X/R ratio of 30, the line current approaches a value of almost 14.2 pu close to 1.45 seconds. The oscillations start decreasing in magnitude till around 6.8 seconds. Between 6.8 and 10.9 seconds, the oscillations appear to have disappeared, however, beyond 10.96 seconds, they reappear and start increasing in magnitude gradually. Beyond 15 seconds, the oscillations are bounded in magnitude between 1.5 and 4 pu and this can be attributed to a limit cycle. Also, it should be noted that the double frequency component in the line current exists only till about 6 seconds beyond which it disappears.

The system was also subjected to a step change in the load torque for an X/R ratio of 20, operating slip of 1% and series compensation of 60% and the dynamic responses of the variables were observed. The system variables followed the same wave shape as those corresponding to a frequency disturbance in the system with X/R ratio of 20 for a load

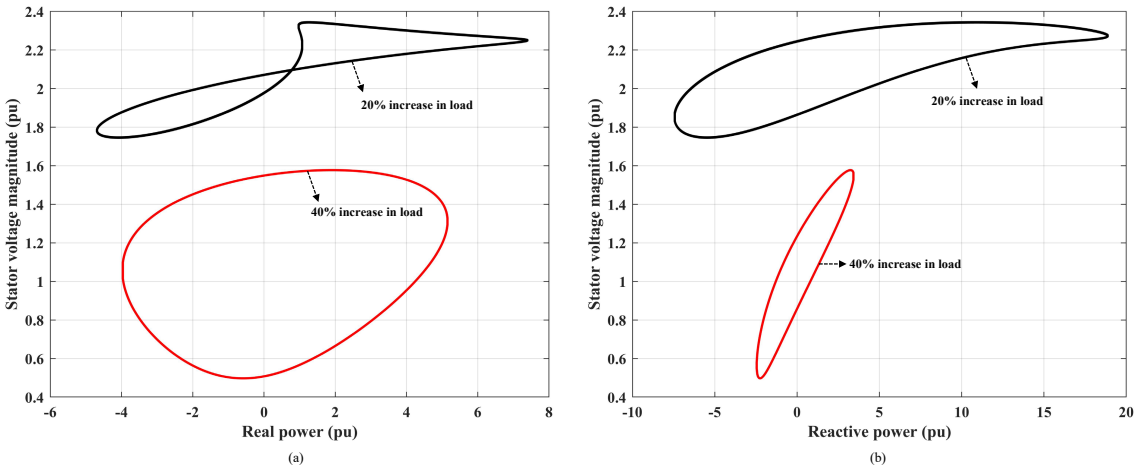

Fig. 6.11: Limit cycles with respect to real and reactive power and motor terminal voltage for a load step change

step change of 20% on the induction motor. However, when the load torque disturbance was increased to 40%, the time responses of the variables are very similar to the case when the system with X/R ratio of 30 was subjected to a frequency disturbance. The rotor speed, torque with respect to time and the limit cycle with respect to rotor speed and torque are shown in Fig. 6.10. The limit cycles with respect to real power and voltage magnitude and reactive power and voltage magnitude are shown in Fig. 6.11. The reason for the reversal of induction motor may be explained as follows: when the system is subjected to a disturbance, there are self-excited oscillations of increasing magnitudes as a result of induction generator effect of SSR. This results in voltages and currents at subsynchronous frequencies induced in the stator winding of the induction motor in addition to the applied voltage at supply frequency. The resultant emfs induced in the stator winding may result in an opposite phase sequence resulting in a magnetic field rotating in the opposite direction and the induction motor follows the direction of the resultant magnetic field and starts rotating in the opposite direction.

6.5 Conclusions

Eigenvalue analysis of an induction motor load fed from the substation through a series compensated weak network exhibits Hopf bifurcations which can be attributed to sub-synchronous resonance. As the load on the induction motor increases, the operating slip increases. This has little influence on the percentage series compensation level at which the Hopf bifurcation occurs. However, for decreasing grid strengths due to increase in the impedance of the feeder, the stability domain with respect to series compensation decreases as SSR occurs at lower levels of percentage series compensation. Size of limit cycles generated as a result of Hopf bifurcation due to SSR depends on the grid strength. Limit cycles are smallest when the interconnection is the weakest. Motor stalling is observed as a result of SSR. However, the direction of rotation of the motor during the limit cycle is dependent on the grid strength as well as the magnitude of disturbance. There is a possibility of reversal in the direction of rotation for lower grid strengths and disturbances of higher magnitudes. In this analysis, the substation voltage is assumed to be at a constant value which in practice is possible only if there is a voltage regulating device like a STATCOM or SVC installed. Hence, to mitigate harmful oscillations in the system due to Hopf bifurcations, a supplementary damping controller is needed.

CHAPTER 7

Dynamic Interactions of Synchronous Generators with Induction Motor Loads in Series Compensated Systems

Dynamic modeling and stability domain analysis of a system consisting of a synchronous generator supplying an induction motor load through a series compensated weak network has been carried out in this chapter. In the previous chapter, the induction motor load is supplied from a stiff voltage source at the substation. However, the assumption of a stiff voltage source is eliminated by considering the complete dynamic model of the generator and it's control system. The impact of X/R ratio of the feeder and generation control system parameters on the stability domain with respect to series compensation has been examined through eigenvalue calculations and time domain simulations to reveal new bifurcations in the system.

7.1 Mathematical modeling of system

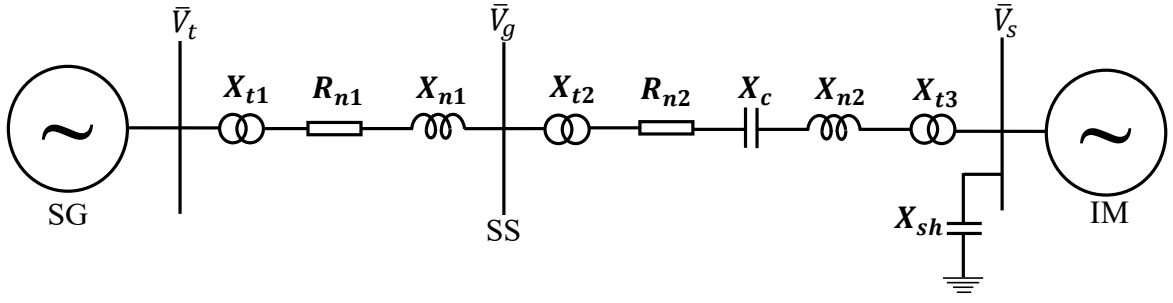

Fig. 7.1: Single line diagram of system under study

The single line diagram of the system under study is shown in Fig. 7.1. It consists of a Synchronous Generator (SG) supplying power to a substation (SS) through a transformer

and a short line. The substation is connected to an induction motor load through a series compensated long feeder. Traditionally, studies related to subsynchronous resonance have been performed in system consisting of a generator connected to an infinite bus through a series compensated line. Here, this study is extended to study the effect of series compensation on an induction motor load supplied through a series compensated feeder from the substation. This is a more realistic study as the effect of series compensation on the network beyond the substation is studied in very little detail in the past. The influence of large dynamic loads on power system stability has been studied in [66]. Although the exciter gain and direct axis time constant of the induction motor has been found to impact stability of the system, the influence of time constants of the measurement transducer and the exciter has not been modeled. In this paper, the exciter and measurement transducers have been modeled using first order transfer functions in order to study the influence of these time constants on the stability domain of the system with respect to series compensation.

7.1.1 Modeling of network

The dynamics of the terminal voltage of the synchronous machine is given by the following equation:

$$\{V_t\} = \frac{1}{\omega_s} X_{nw}[U]\frac{d}{dt}\{I_n\} + [Z_{nw}]\{I_n\} + \{V_c\} + \{V_m\} \tag{7.1}$$

where $[Z_{nw}] = [Z_{T1} + Z_{L1} + Z_{T2} + Z_{L2} + Z_{T3}]$, $X_{nw} = X_{t1} + X_{n1} + X_{t2} + X_{n2} + X_{t3}$ and

$$[Z_{T1}] = \begin{bmatrix} R_{t1} & -X_{t1} \\ X_{t1} & R_{t1} \end{bmatrix}, [Z_{L1}] = \begin{bmatrix} R_{n1} & -X_{n1} \\ X_{n1} & R_{n1} \end{bmatrix}, [Z_{T2}] = \begin{bmatrix} R_{t2} & -X_{t2} \\ X_{t2} & R_{t2} \end{bmatrix},$$

$$[Z_{L2}] = \begin{bmatrix} R_{n2} & -X_{n2} \\ X_{n2} & R_{n2} \end{bmatrix}, [Z_{T3}] = \begin{bmatrix} R_{t3} & -X_{t3} \\ X_{t3} & R_{t3} \end{bmatrix}, \tag{7.2}$$

The elements of vectors $\{I_n\}$, $\{V_m\}$, $\{V_c\}$ and $\{V_t\}$ are given by:

$$\{I_n\} = [I_{dn} \quad I_{qn}]^T \tag{7.3}$$

$$\{V_m\} = [V_{dm} \quad V_{qm}]^T \tag{7.4}$$

$$\{V_c\} = [V_{dc} \quad V_{qc}]^T \tag{7.5}$$

$$\{V_t\} = [V_{dt} \quad V_{qt}]^T \tag{7.6}$$

The voltage across the series capacitor is modeled using equation (7.7) given below:

$$\frac{1}{\omega_s}\frac{d}{dt}\{V_c\} = [Z_{se}]\{I_n\} + [N_1]\{V_c\} \tag{7.7}$$

where $[Z_{se}] = X_c[U]$.

The dynamics of the shunt capacitor voltage at the terminals of the induction motor are described by the following equation:

$$\frac{1}{\omega_s}\frac{d}{dt}\{V_m\} = [Z_{sh}]\{I_n - I_s\} + [N_1]\{V_m\} \tag{7.8}$$

where $[Z_{sh}] = X_{sh}[U]$ and $\{I_s\} = [I_{ds} \quad I_{qs}]^T$ are the d and q components of the stator current of the induction motor.

7.1.2 Integration of SG and Network Models

The dynamic model of the synchronous generator is expressed in a reference frame fixed on it's rotor to eliminate time varying inductances. However, when the synchronous machine is interfaced with the rest of the network, the terminal voltage of the generator in the rotor reference frame (V_d, V_q) can be expressed in a synchronously rotating reference frame (V_{dt}, V_{qt}) using equation (7.9) shown below:

$$\begin{bmatrix} V_{dt} \\ V_{qt} \end{bmatrix} = \underbrace{\begin{bmatrix} \sin\delta & \cos\delta \\ -\cos\delta & \sin\delta \end{bmatrix}}_{T_r} \begin{bmatrix} V_d \\ V_q \end{bmatrix} \tag{7.9}$$

where $[T_r]$ is the transformation matrix. The inverse transformation is accomplished through matrix $[Q] = [T_r]^{-1}$. In this system, the synchronous machine is directly connected to the network which means the stator currents of the generator are the same as those of the network currents. The transformation of the generator stator currents in the rotor reference frame to the synchronously rotating reference frame is achieved using equation (7.10).

$$\begin{bmatrix} I_{dn} \\ I_{qn} \end{bmatrix} = \underbrace{\begin{bmatrix} \sin\delta & \cos\delta \\ -\cos\delta & \sin\delta \end{bmatrix}}_{T_r} \begin{bmatrix} I_d \\ I_q \end{bmatrix} \tag{7.10}$$

Using equations (7.9), (7.10) and (7.1) in (2.10), the final equation used to interface the synchronous generator with electrical network and load is obtained which is given by equation (7.11).

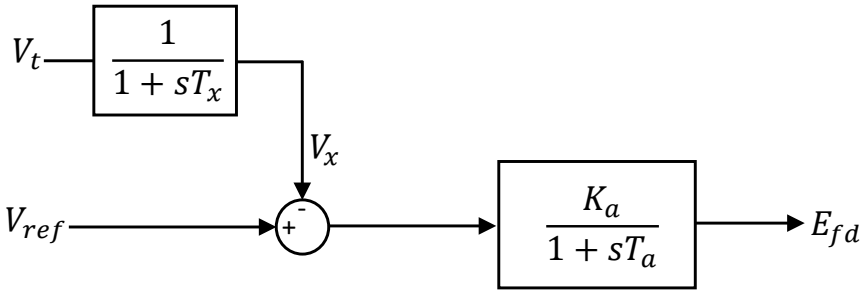

Fig. 7.2: Block diagram of AVR

$$\frac{1}{\omega_s}[X_{sg1}Q - QX_{nw}]\frac{d}{dt}I_n + \frac{1}{\omega_s}[N_1^2]\frac{d}{dt}E'_{sg} + \frac{1}{\omega_s}[X_{sg1}Q_dI_n]\frac{d}{dt}\delta = [Z_{sg}Q + QZ_{nw}]I_n + \omega[N_1^2]E'_{sg} + [Q]V_c + [Q]V_m \tag{7.11}$$

where, in (7.11), the matrix $[Q_d]$ is the derivative of matrix $[Q]$ with respect to the rotor position δ. The elements of matrices $[Q]$ and $[Q_d]$ are given below:

$$[Q] = \begin{bmatrix} \sin\delta & -\cos\delta \\ \cos\delta & \sin\delta \end{bmatrix} \tag{7.12}$$

$$[Q_d] = \begin{bmatrix} \cos\delta & \sin\delta \\ -\sin\delta & \cos\delta \end{bmatrix} \tag{7.13}$$

7.2 Modeling of AVR and Governor

The block diagram of the Automatic Voltage Regulator (AVR) of the SG is shown in Fig. 7.2. The terminal voltage magnitude (V_t) of the SG is measured by a transducer of time constant T_x seconds and is compared with the reference voltage V_{ref}. The AVR is represented using a first order transfer function consisting of a gain K_a and time constant

T_a seconds. The speed governor dynamics are modeled using a first order differential equation which determines the mechanical torque input (T_m) to the rotor of the SG. The differential equations which govern the dynamics of the AVR and the speed governor are given below:

$$T_x \frac{dV_x}{dt} = -V_x + V_t \tag{7.14}$$

$$T_a \frac{dE_{fd}}{dt} = -E_{fd} + K_a(V_{ref} - V_x) \tag{7.15}$$

$$T_g \frac{dT_m}{dt} = -T_m + P_c - (1/R_d)(\omega - 1) \tag{7.16}$$

In equations (7.14) to (7.16), V_x is the output of the measurement transducer, E_{fd} is the input voltage applied to the field winding on the rotor of the SG, P_c is the control input which is fixed and R_d is the droop of the speed governor. The values of T_g and R_d are assumed to be 50 ms and 5% respectively.

7.3 Eigenvalue analysis

The complete state-space model of the system is developed and is linearized and cast in the form $\Delta\dot{X} = [J]\Delta X$ where X is the vector of system state variables and ΔX is the linearized state variable vector. The state variables considered in this system are the d and q axis components of stator and rotor currents, terminal voltage and slip of the induction motor, field and damper winding emfs, mechanical torque, rotor angle and speed of the synchronous generator, d and q axis components of the line current and series capacitor voltage and variables V_x and E_{fd} associated with the AVR as explained in Section 7.2. The eigenvalues of the linearized mathematical model of the system are calculated and analyzed for various values of system parameters and the results are presented in the following sections:

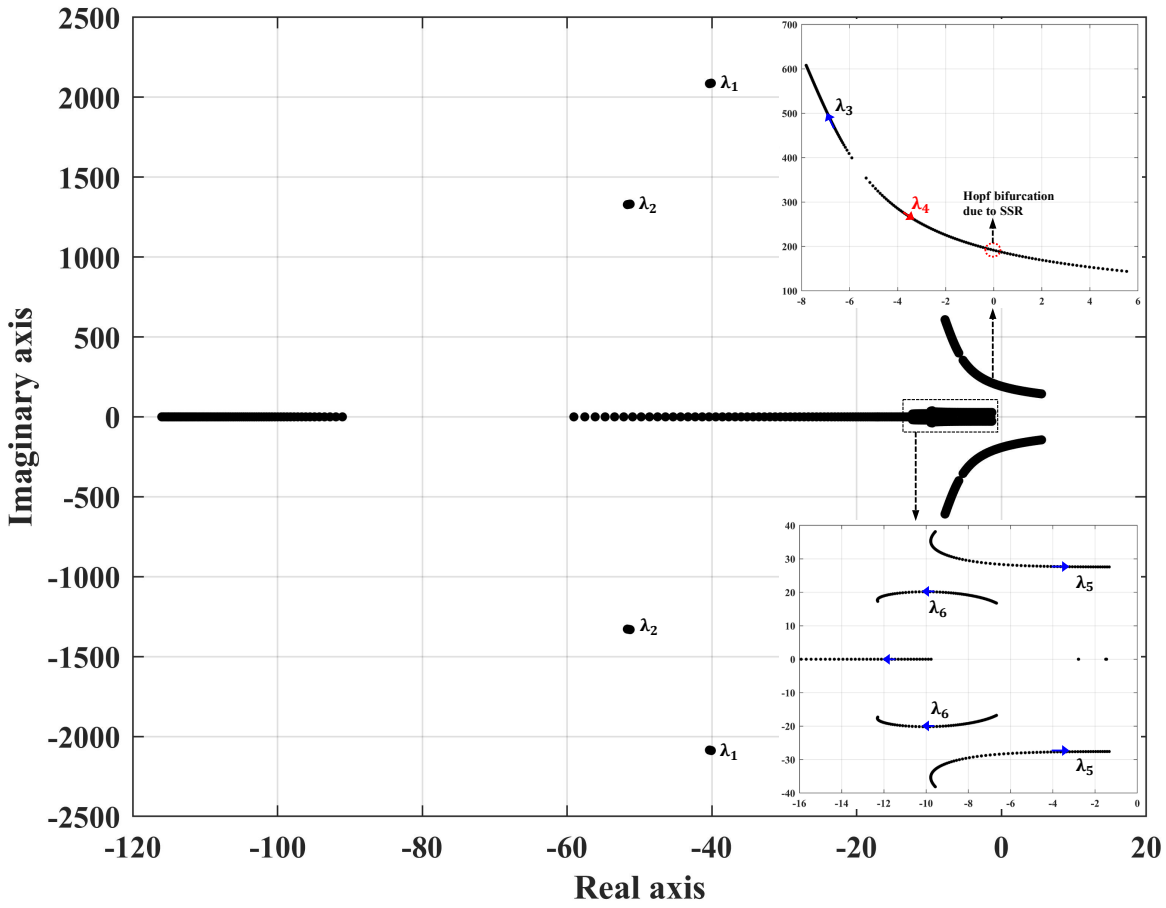

Fig. 7.3: Eigenvalue trajectory for base case

7.3.1 Eigenvalues of base case

Eigenvalues of the system under study are computed for the following operating conditions: the induction motor slip is at 2% and the X/R ratio of the line is assumed to be 20, exciter of the SG has a gain and time constant of 500 and 25 ms respectively and the measurement transducer time constant of the AVR is 10 ms. The series compensation level of the system ($K_c = X_c/X_{nw}$) is varied from 1% to 95%.

The eigenvalues of the system along with the corresponding dominant state variables for each mode are presented in Table 7.1. for a series compensation of 60%. There are 6 oscillatory modes (λ_1 to λ_6) and 5 non-oscillatory modes (λ_7 to λ_{11}). The system starts out to be stable as the series compensation is at 1% and remains stable up to 62%. As

Table 7.1: Eigenvalues for base case

$\boldsymbol{\lambda_i}$	$\boldsymbol{-\sigma \pm j\omega}$	**Participating States**
λ_1	$-40.188 \pm j2086.8$	I_{dn}, I_{qn}, I_{ds}, I_{qs}, I_{dr}, I_{qr}, V_{dm}, V_{qm}
λ_2	$-51.454 \pm j1330$	I_{dn}, I_{qn}, I_{ds}, I_{qs}, I_{dr}, I_{qr}, V_{dm}, V_{qm}
λ_3	$-7.4056 \pm j557.92$	I_{dn}, I_{qn}, I_{ds}, I_{qs}, I_{dr}, I_{qr}, V_{dc}, V_{qc}
λ_4	$-0.2358 \pm j194.8$	I_{dn}, I_{qn}, I_{ds}, I_{qs}, I_{dr}, I_{qr}, V_{dc}, V_{qc}
λ_5	$-7.1786 \pm j28.759$	I_{ds}, I_{qs}, I_{dr}, I_{qr}, E'_q, V_x, E_{fd}
λ_6	$-10.157 \pm j20.166$	I_{ds}, I_{qs}, I_{dr}, I_{qr}, E'_q, s_m
λ_7	-106.99	I_{ds}, I_{qs}, I_{dr}, I_{qr}, E'_q, V_x, E_{fd}
λ_8	-24.485	I_{ds}, I_{qs}, I_{dr}, I_{qr}, E_{fd}
λ_9	-17.112	I_{ds}, I_{qs}, I_{dr}, I_{qr}, T_m, ω
λ_{10}	-2.7822	T_m, ω
λ_{11}	-1.4834	I_{ds}, I_{qs}, I_{dr}, I_{qr}, E'_d

Table 7.2: Critical eigenvalues for different X/R ratios

X/R ratio	$\boldsymbol{K_{cr}}$	$\boldsymbol{\lambda_{cr} = -\sigma \pm j\omega}$	**Participating states**
10	74%	$0.0522 \pm j192.07$	I_{dn},I_{qn},I_{ds},I_{qs},I_{dr},I_{qr},V_{dc},V_{qc}
30	56%	$0.0792 \pm j189.43$	

the compensation is increased beyond 62%, the system becomes unstable due to SSR as the oscillatory mode λ_4 crosses over to the right half of the complex plane resulting in an unstable system. The same analysis when repeated for a lower X/R ratio of the system ($X/R = 10$) revealed a Hopf bifurcation due to SSR at a higher value of critical series compensation ($K_{cr} = 74\%$, $\lambda_{cr} = 0.0522 \pm j192.07$) and for a higher X/R ratio of 30, the critical value of series compensation is $K_{cr} = 56\%$ with $\lambda_{cr} = 0.0792 \pm j189.43$.

7.3.2 Influence of AVR parameters on stability domain

The influence of exciter parameters on the stability domain of the system with respect to series compensation level is explored in this section through eigenvalue analysis. The

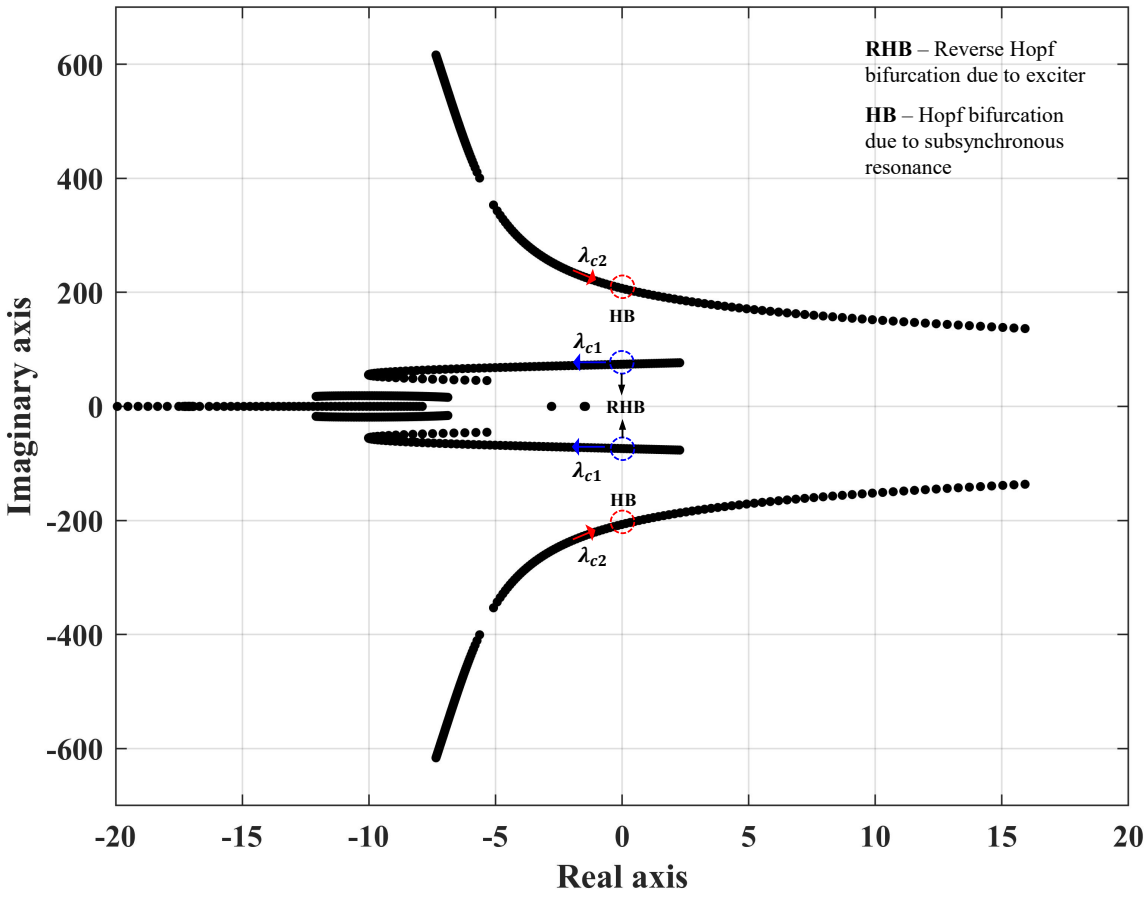

Fig. 7.4: Eigenvalue trajectory for $K_a = 2000$

parameters under study are the gain of the exciter and the time constants of the AVR and measurement transducer.

7.3.2.1 Influence of exciter gain

Eigenvalues of the system are computed for the system under study for the following operating conditions: the induction motor slip is at 2% and the X/R ratio of the feeder (X_{n2}/R_{n2}) is assumed to be 25, exciter of the SG has a gain and time constant of 2000 and 25 ms respectively and the measurement transducer time constant of the AVR of the SG is 10 ms. The eigenvalue trajectory of the system are presented in Fig. 7.4 as the degree of series compensation K_c is varied from 1% to 98%. The non-oscillatory modes are stable

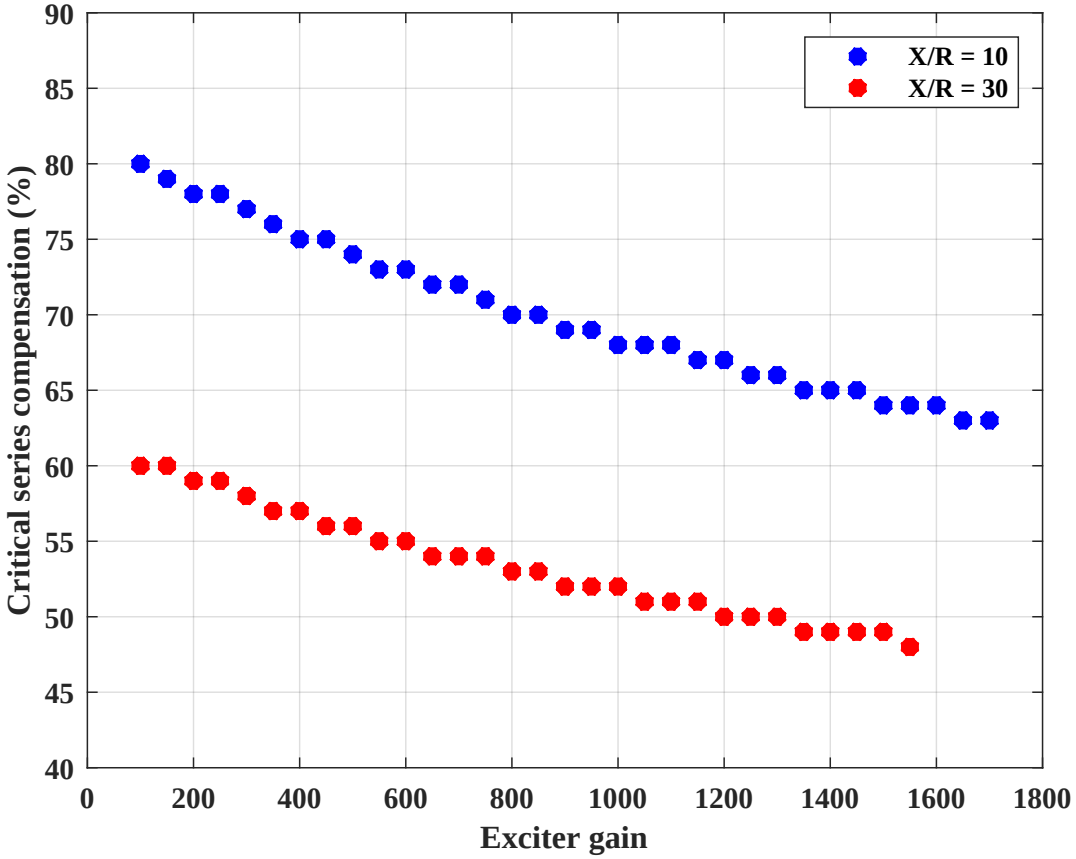

Fig. 7.5: Hopf bifurcation points for varying exciter gains

for the entire range of series compensation considered. When K_c is at 1%, there is an oscillatory mode on the right half of the complex plane ($\lambda_{c1} = 2.2759 \pm j76.585$) making the system unstable. As the compensation increases, λ_{c1} moves toward the left half of the complex plane and when K_c exceeds 24%, λ_{c1} moves into the left half of the complex plane which results in a stable system as a consequence of a reverse Hopf bifurcation. As K_c further increases, the system becomes unstable once again as another oscillatory mode moves to the right half of the complex plane when K_c exceeds 49%. The critical eigenvalues at this point are $\lambda_{c2} = 0.1471 \pm j205.38$. Instability in this case is a result of a Hopf bifurcation occurring due to SSR. Critical eigenvalues and participation factors of the system for 2 different series compensation levels of 15% and 50% are presented in Table 7.1.

Table 7.3: Critical eigenvalues for AVR gain of 2000

K_{cr}	$\lambda_{cr} = -\sigma \pm j\omega$	Participating states
15%	$0.9597 \pm j75.013$	I_{ds},I_{qs},I_{dr},I_{qr},E'_q,V_x,E_{fd}
50%	$0.094 \pm j170.26$	I_{dn},I_{qn},I_{ds},I_{qs},I_{dr},I_{qr},V_{dc},V_{qc}

The eigenvalues of the system were further computed for various exciter gains for X/R ratios of 10 and 30. In Fig. 7.5, the variation of Hopf bifurcation points with respect to exciter gain and series compensation levels are shown. For an AVR gain of 100, the system with X/R ratios of 10 and 30 loses stability through a Hopf bifurcation due to SSR when the series compensation level is 80% and 60% respectively. As the AVR gain increases, the percentage series compensation at which SSR occurs decreases resulting in smaller stability domains.

As the AVR gain was increased to 1600 for an X/R ratio of 30, the system was unstable for K_c of 1% to 3% and when K_c is increased beyond 4%, the system becomes stable causing a reverse Hopf bifurcation. The system remains stable for values of K_c up to 47% and as $K_c \geq 48\%$, the system loses stability due to SSR. As the AVR gain is increased to 1800, the system experiences a reverse Hopf bifurcation (RHB) and a Hopf bifurcation (HB) at K_c values of 16% and 47% respectively. Similar phenomenon was observed for the system with X/R ratio of 10, however the stability domains were found to be much higher. For example, for an AVR gain of 1800 in the system with $X/R = 10$, the RHB and HB points correspond to K_c values of 5% and 62% respectively. Hence, from this it can be inferred that for higher AVR gains, value of K_c at which the reverse Hopf bifurcation occurs increases which further reduces the size of the stability domain. Overall, the size of the stability domain with respect to K_c is much smaller for a weaker system especially for high AVR gains.

7.3.3 Influence of exciter time constant

The time constant of the AVR has a significant impact on the stability domain of the system with respect to series compensation which would be described in this section. Eigenvalues of the system were analyzed as the series compensation is varied from 1% to 98% for various values of exciter time constant. This was done for systems with X/R ratios of 10 and 30. This analysis was performed for AVR gains of 500 and 1000 and the results are presented in Tables 7.4 and 7.5 respectively. Stability domain of the system with respect to K_c is increased as the AVR time constant is increased from 1 ms to 40 ms as the Hopf bifurcation point due to SSR is moved from $K_c = 51\%$ to $K_c = 77\%$ for the system with $X/R = 10$. When the time constant is increased to 42 ms, instability due to a Hopf bifurcation occurs due to a mode corresponding to the exciter at $K_c = 75\%$. As the time constant increases further to 70 ms, the stability domain shrinks further as the Hopf bifurcation point due to the exciter is shifted to $K_c = 6\%$. When $T_a \geq 80$ ms, the stable operation of the system is not possible for any level of K_c as the system is unstable for K_c starting at 1%.

The same phenomenon occurs for the system with $X/R = 30$, however, the stability domain starts decreasing when $T_a \geq 59$ ms which is higher compared to the previous case with $X/R = 10$. Stable operation of the system is impossible for $T_a \geq 100$ ms which is also higher compared to the previous case. Also, when the time constant $T_a = 59$ ms, as K_c changes from 58% to 59%, 2 pairs of complex eigenvalues ($\lambda_{c1} = 0.0277 \pm j184.7$, $\lambda_{c2} = 0.0194 \pm j23.495$ at $K_c = 59\%$) crossover from the left to the right half of the complex plane resulting in a Hopf-Hopf bifurcation.

The exciter gain is increased to 1000 and the same analysis was performed on the systems with X/R ratios of 10 and 30 and the results are presented in Table 7.5. The stability domain with respect to K_c is greater for the system with $X/R = 10$ up to a value of T_a

T_a (ms)	$X/R = 10$		$X/R = 30$	
	K_{cr} (%)	$\lambda_{cr} = -\sigma \pm j\omega$	K_{cr} (%)	$\lambda_{cr} = -\sigma \pm j\omega$
1	51	$0.0203 \pm j224.79$	38	$0.0609 \pm j223.53$
5	57	$0.0423 \pm j214.73$	43	$0.0962 \pm j212.61$
10	65	$0.0473 \pm j203.49$	49	$0.0689 \pm j201.35$
20	72	$0.0279 \pm j194.52$	54	$0.0034 \pm j192.75$
30	75	$0.027 \pm j190.88$	57	$0.0831 \pm j187.81$
40	77	$0.0644 \pm j188.5$	58	$0.0547 \pm j186.24$
50	54	$0.0019 \pm j24.798$	59	$0.0783 \pm j184.65$
60	30	$0.0292 \pm j23.87$	58	$0.0428 \pm j23.408$
70	6	$0.0012 \pm j23.116$	45	$0.0469 \pm j22.703$
80	1	$0.4935 \pm j22.09$	32	$0.0189 \pm j22.111$

Table 7.4: Critical eigenvalues for various AVR time constants at an AVR gain of 500

T_a (ms)	$X/R = 10$		$X/R = 30$	
	K_{cr} (%)	$\lambda_{cr} = -\sigma \pm j\omega$	K_{cr} (%)	$\lambda_{cr} = -\sigma \pm j\omega$
1	37	$0.1122 \pm j247.35$	27	$0.1024 \pm j247.53$
10	56	$0.0463 \pm j215.27$	42	$0.0250 \pm j213.76$
20	66	$0.0725 \pm j201.77$	50	$0.1073 \pm j199.22$
30	70	$0.0172 \pm j196.79$	53	$0.0520 \pm j194.2$
40	73	$0.0694 \pm j193.13$	55	$0.0609 \pm j190.94$
50	36	$0.0147 \pm j36.324$	56	$0.032 \pm j189.36$

Table 7.5: Critical eigenvalues for various AVR time constants at an AVR gain of 1000

close to 40 ms compared to the system with $X/R = 30$. When $T_a = 50$ ms, the system with $X/R = 10$ has a much smaller stability domain as the system loses stability due to a Hopf bifurcation with the exciter mode causing instability at $K_c = 36\%$. This is much smaller compared to the Hopf bifurcation point which corresponds to $K_c = 56\%$ due to SSR for the system with $X/R = 30$. Also note that as T_a varies from 1 to 40 ms, the stability domain increases as the critical value of K_c causing a Hopf bifurcation

T_x (ms)	$X/R = 10$		$X/R = 30$	
	K_{cr} (%)	$\lambda_{cr} = -\sigma \pm j\omega$	K_{cr} (%)	$\lambda_{cr} = -\sigma \pm j\omega$
1	64	$0.052 \pm j205.81$	48	$0.0699 \pm j204$
5	69	$0.0862 \pm j198.52$	52	$0.0973 \pm j196.32$
10	74	$0.0522 \pm j192.07$	56	$0.0792 \pm j189.43$
15	77	$0.0866 \pm j188.41$	58	$0.0713 \pm j186.17$
20	78	$0.0426 \pm j187.26$	59	$0.0583 \pm j184.59$
25	56	$0.014 \pm j26.955$	60	$0.0919 \pm j183.01$
30	30	$0.0039 \pm j26.951$	60	$0.0459 \pm j183.06$
35	1	$0.0933 \pm j27.902$	47	$0.0412 \pm j26.127$

Table 7.6: Critical eigenvalues for various measurement time constants at an AVR gain of 500

T_x (ms)	$X/R = 10$		$X/R = 30$	
	K_{cr} (%)	$\lambda_{cr} = -\sigma \pm j\omega$	K_{cr} (%)	$\lambda_{cr} = -\sigma \pm j\omega$
1	53	$0.0661 \pm j221.22$	39	$0.004 \pm j221$
5	61	$0.1190 \pm j208.75$	46	$0.0354 \pm j206.65$
10	68	$0.0008 \pm j199.28$	52	$0.1094 \pm j195.83$
15	73	$0.1027 \pm j192.97$	55	$0.084 \pm j190.8$

Table 7.7: Critical eigenvalues for various measurement time constants at an AVR gain of 1000

due to SSR increases for each of the systems with X/R ratios of 10 and 30 respectively. Furthermore, the system also undergoes a reverse Hopf bifurcation for $T_a \geq 64$ ms at smaller values of K_c in addition to the Hopf bifurcation which occurs due to SSR as K_c is increased. This shows that for it may be impossible to operate a weak system in a stable manner without a minimum level of series compensation.

7.3.4 Influence of time constant of measurement transducer

Eigenvalue analysis was conducted for the system with X/R ratios of 10 and 30 for various values of time constant of the measurement transducer. Just as it was described

in the previous section with respect to T_a, here, the stability domain increases for both the systems with X/R ratios of 10 and 30 as T_x increases up to 20 ms. Beyond that, as $T_x \geq 25$, the system with $X/R = 10$ becomes unstable at lower values of K_c due to the exciter mode. This phenomenon is observed in the system with $X/R = 30$ as well, however, at a higher value of T_x at 35 ms. Hence, up to a certain value of T_x, the stability domain of the stronger system is bigger than that of the weaker system. However, beyond a certain value of T_x, the weaker system has a larger stability domain. As the AVR gain is increased to 1000, the system shows similar behavior. In addition to Hopf bifurcations due to SSR and exciter mode destabilization, reverse Hopf bifurcations occur as well at small values of K_c. Hence, systems using AVRs with high gains need a minimum level of K_c in order to have stable operation. Depending on the values of T_x and T_a, the upper limit of K_c is determined either by SSR or exciter mode destabilization.

7.4 Time domain simulation results

The nonlinear dynamic model of the system is programmed in SIMULINK and the results generated are presented in this section. The responses of the system with respect to time are studied for AVR gain K_a of 500 and different values of time constants of the AVR control system. The series compensation level for the system is at 50% which is realistic for a weak system with an X/R ratio of 30.

7.4.1 Exciter time constant $T_a = 10$ ms

The responses of induction motor speed and terminal voltage are shown in Fig.7.6 for a disturbance in the form of a 20% increase in the load torque on the induction motor. In this case, the AVR limits have not been modeled as a result of which, oscillations in the voltage increase with time. This is a consequence of a subcritical Hopf bifurcation as a

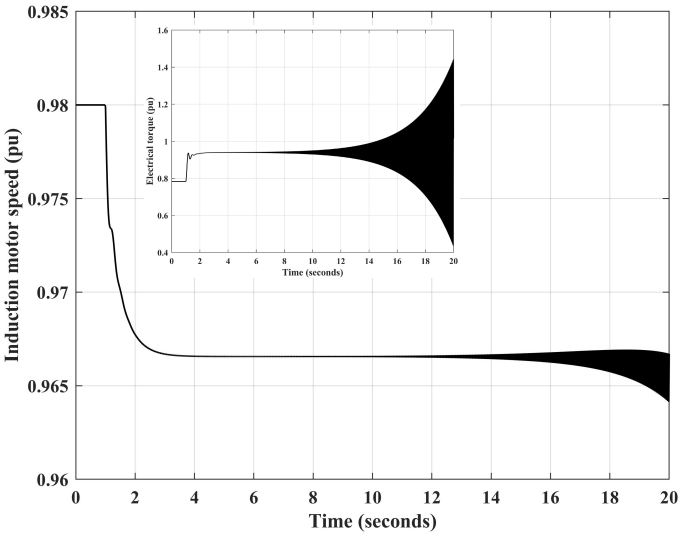

(a) Induction motor speed

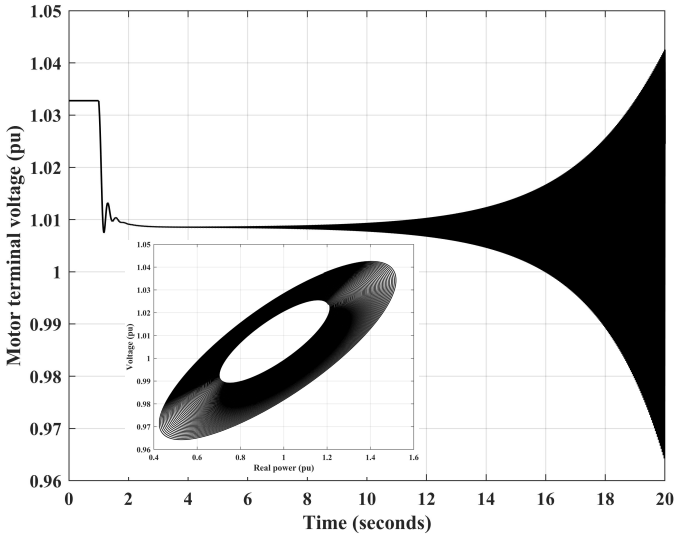

(b) Motor terminal voltage

Fig. 7.6: Time responses for the system without AVR limits

result of SSR which causes excessive voltages and currents.

Limits on the excitation system have been imposed and the simulations were repeated and the time responses are presented in Fig. 7.7. Exciter limits impose an upper and lower limit on the field voltage applied to the rotor winding of the synchronous machine resulting in an arrest on the growth of oscillations in the system states. The system now behaves as if the nature of the bifurcation is supercritical resulting in sustained oscillations

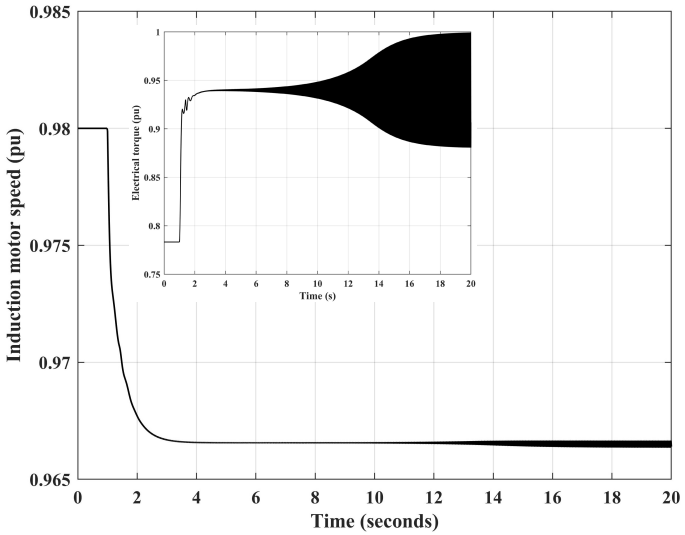

(a) Induction motor speed

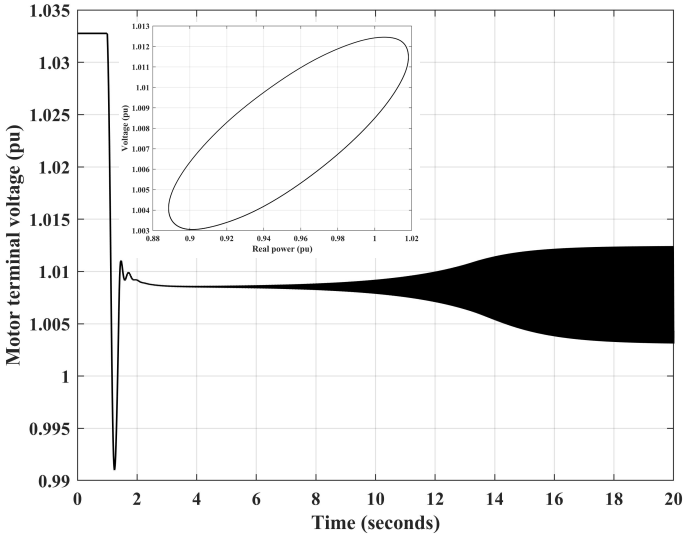

(b) Motor terminal voltage

Fig. 7.7: Time responses for the system with AVR limits

of fixed amplitude with respect to time. Phase plane trajectory of the induction motor speed in Fig. 7.8 reveal an unstable system with growing oscillations if the AVR limits are neglected and a system with oscillations bounded in magnitude if the AVR limits are taken into account.

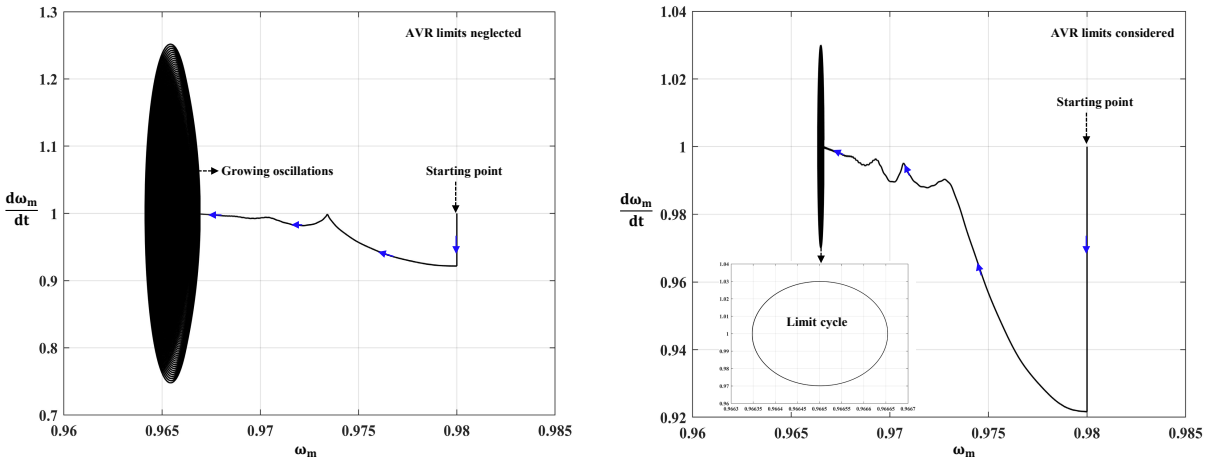

Fig. 7.8: Phase plane trajectory of induction motor speed for $T_a = 10$ ms

7.4.2 Exciter time constant $T_a = 70$ ms

Time traces of induction motor speed and terminal voltage are presented in Fig. 7.9 when the AVR limits of the synchronous machine are neglected. The system shows an oscillatory response bounded in magnitude characterizing a supercritical Hopf bifurcation. The amplitude of oscillations appear to continually change within a bound for the quantities presented. However, with the AVR limits included, the oscillations appear to be bounded with fixed amplitude characterizing a supercritical bifurcation in this case as well. These are evident from the time responses of induction motor speed and terminal voltage as shown in Fig. 7.10.

Phase-plane trajectories of induction motor speed when the AVR time constant is set at 70 ms are presented in Fig. 7.11. In the case where the AVR limits are neglected, a supercritical Hopf bifurcation is observed in the system which appears to undergo repeated period doublings. This is evident in the one to the left in Fig. 7.11. The amplitude of oscillations although bounded appear to change continuously in a random manner which is the characteristic of 'quasi-chaos'. However, with the AVR limits modeled, the phase-plane trajectory of induction motor speed shows a well-defined limit cycle and the absence of a period doubling bifurcation. This is due to the fact that with AVR limits

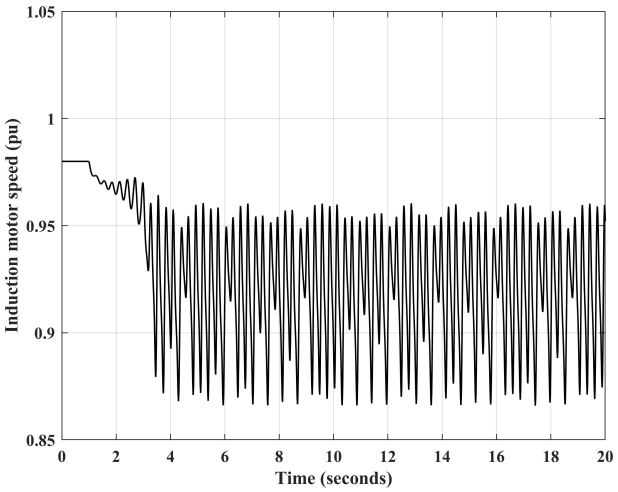

(a) Induction motor speed

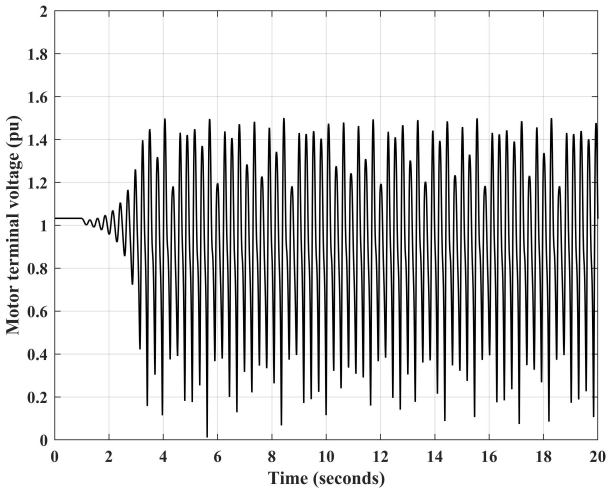

(b) Motor terminal voltage

Fig. 7.9: Time responses for the system without AVR limits

modeled, the voltage applied to the field winding is allowed to vary only between ±3 pu. This limit is much lower than the minimum amplitude of oscillations in E_{fd} when it varies in a random manner when AVR limits are neglected. This imposes a bound on the variations in the generator terminal voltage which is reflected at the motor terminal voltage and impacts the speed of the motor which varies only within a limit.

Further investigations were carried out with regards to the period-doubling bifurcation observed in the system when AVR limits were neglected. The system was subject to

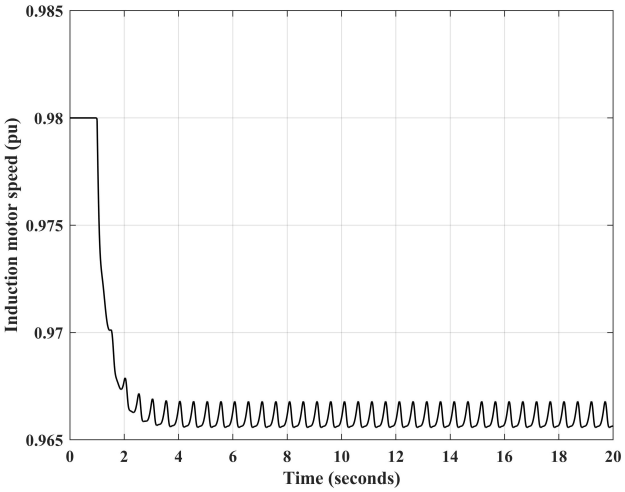

(a) Induction motor speed

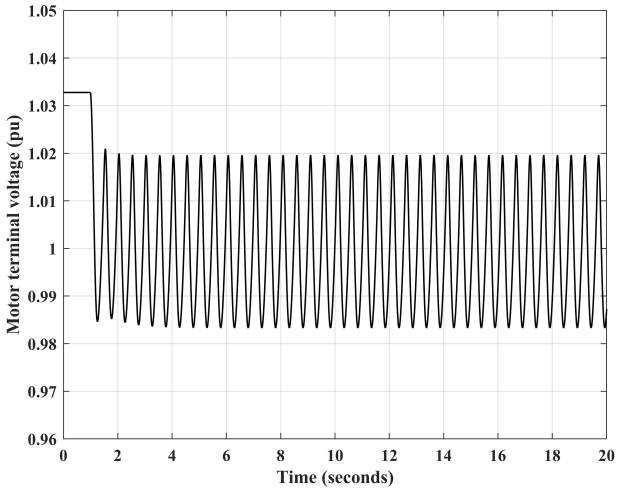

(b) Motor terminal voltage

Fig. 7.10: Time responses for the system with AVR limits

different step increases in the induction motor load torque and phase-plane trajectories of the induction motor speed are plotted and are shown in Fig. 7.12. With the system subject to a 25% increase in the load torque, the number of period doublings are hard to count as the trajectories are so close to each other. As the step change was increased to 30%, 2 period doublings can be observed. The number of period doublings reduced to 1 when the load torque disturbance was increased to 35% and finally, the period doubling bifurcation is found to be absent when the load torque disturbance magnitude was increased to 45%.

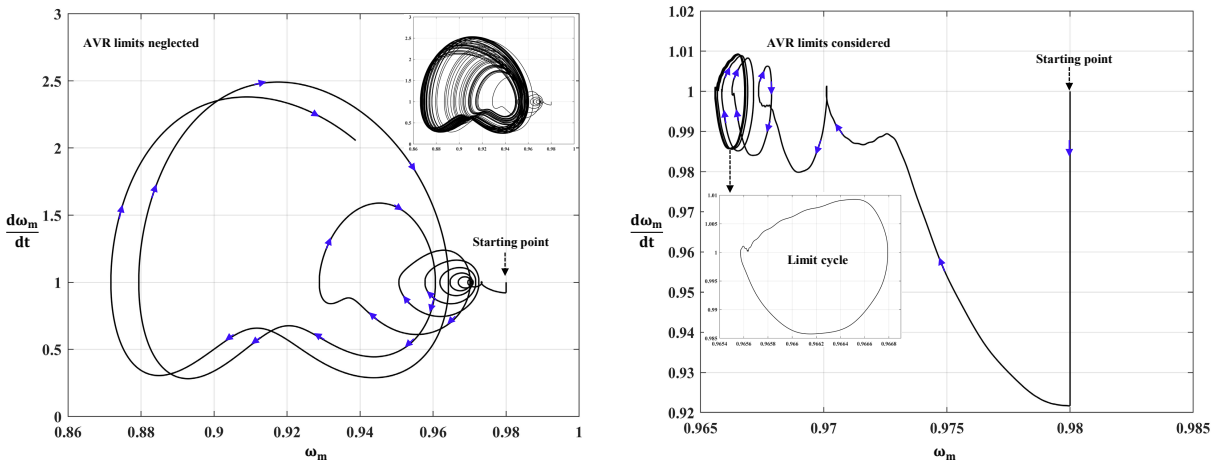

Fig. 7.11: Phase plane trajectory of induction motor speed for $T_a = 70$ ms

7.5 Conclusion

In this chapter, the dynamic analysis of induction motor loads fed through weak interconnections was performed through analyzing eigenvalues of the system and time domain simulations. Control system parameters of the AVR have a significant impact on the stability domain with respect to series compensation. The AVR gain, time constants of AVR and measurement transducers have to be taken into account while determining percentage series compensation to avoid instability due to subsynchronous resonance or exciter mode destabilization. Depending upon the speed of response of the AVR and measurement transducer, the stability domain of the weaker system may be bigger or smaller than that of a relatively stronger system. This shows that a supplementary controller is needed to operate the system in a stable manner.

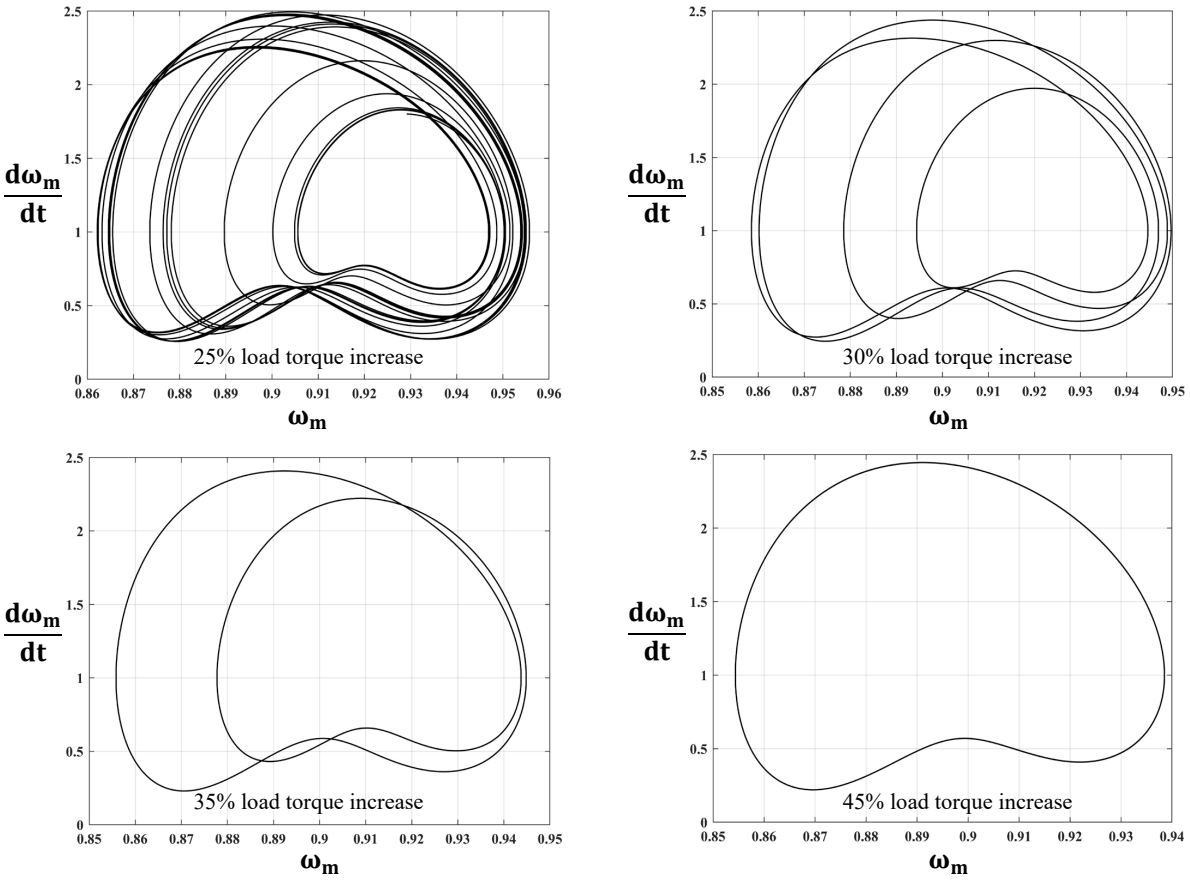

Fig. 7.12: Period doublings for various step changes in load torque

CHAPTER 8

Conclusions and Future Research Direction

Dynamic modeling, stability studies through eigenvalue analysis and time domain simulations of series compensated power systems with weak interconnections have been conducted to analyze bifurcations and stability domains with respect to series compensation. The results of these studies have been presented for various network topologies and the following conclusions are presented in the following section.

8.1 Conclusions

[1] Systems with SCIG-WTs integrated with the grid through series compensated radial feeder lose stability through a Hopf bifurcation due to SSR. Stability domains with respect to series compensation become smaller as the interconnection grows weak due to feeders of high impedance. A saddle-focus equilibrium is possible at high wind speeds in systems where the generator terminal voltage is unregulated due to the usage of only fixed shunt capacitors for reactive power compensation.

[2] Systems with SCIG-WTs integrated to the grid by means of non-radial interconnections may have a bigger stability domain. This is due to the fact that in a non-radial interconnection, the X/R ratio of the network may smaller resulting in a higher stability domain with respect to series compensation. However, the critical series compensation level which determines the size of the stability domain depends on the parameters of the SCIG and the X/R ratio of the interconnection. Wind speed may not play a big role in determining the critical series compensation level at which SSR occurs.

[3] A Static Var Compensator (SVC) used in the place of a fixed shunt capacitor to provide reactive power compensation is able to improve the stability domain of the radially connected system by a small margin. However, delays introduced due to the constants of measurement transducers used in the voltage regulator has an adverse effect on the stability domain. When the SVC is further equipped with a supplementary damping controller using generator slip or real power as it's input signals, the stability domain becomes bigger by a wide margin under various operating conditions.

[4] Induction motors interconnected to substations by series compensated feeders may experience instability through subcritical Hopf bifurcations due to SSR resulting in motor stalling and excessive voltage and current. This is exacerbated by higher feeder impedances resulting in a weaker system. Stability domains due to series compensation also decrease by a small margin under higher loading conditions in the motor. Systems with high X/R ratios may experience a reversal in the direction of rotation of the induction motors in addition to stalling causing excessive voltages and currents.

[5] As the dynamics of synchronous generators connected to substations which supply induction motor loads are taken into account, the stability domain with respect to series compensation is affected by the generator voltage control system parameters in addition to the strength of the grid and the load on the motor. Systems with generators using AVRs of high gains have smaller stability domains. The system may be susceptible to reverse Hopf bifurcations when high gain AVRs are used.

[6] Values of time constants of the AVR and measurement transducer determines if the system may become unstable due to a subcritical Hopf bifurcation due to SSR or a supercritical Hopf bifurcation due to the exciter mode destabilization. Stability

domain of the relatively stronger system is larger if the upper limit of series compensation is determined by the level at which SSR occurs. However, the weaker system has a larger stability domain if the upper limit of series compensation is determined by the critical level at which the exciter mode becomes unstable due to a Hopf bifurcation.

8.2 Future research direction

Stability domain analysis enhancement of weak power systems can be explored in the context of systems with multiple generators of the same type or different types. Utilization of energy storage systems to mitigate SSR is another area of research which can be an offshoot of this work. Using other signals in the system in the supplementary damping controller to eliminate SSR is another potential area of research. Identifying optimal locations of controllers to provide maximum improvement in system stability could be another extension of this research. With regards to the impact of dynamic loads on the stability of series compensated systems, modifying the already existing voltage controller and power system stabilizer design to achieve stability domain enhancement is a way to extend the work done in this dissertation.

List of Abbreviations

AVR	Automatic Voltage Regulator
SCIG-WT	Squirrel Cage Induction Generator - Wind Turbine
FBM	First Benchmark Model
SBM	Second Benchmark Model
SG	Synchronous Generator
IM	Induction Motor
SVC	Static Var Compensator
SSR	Subsynchronous Resonance
HB	Hopf Bifurcation
RHB	Reverse Hopf Bifurcation

List of Key Symbols

K_c	Degree of series compensation
V_w	Wind speed
I_{ds}, I_{qs}	d and q axis component of stator current of induction machine
I_{dr}, I_{qr}	d and q axis component of rotor current of induction machine
I_{dn}, I_{qn}	d and q axis component of network current
I_{d1}, I_{q1}	d and q axis component of current through line 1 of the double circuit
I_{d2}, I_{q2}	d and q axis component of current through line 2 of the double circuit
V_{ds}, V_{qs}	d and q axis component of stator voltage of induction generator
V_{dm}, V_{qm}	d and q axis component of stator voltage of induction motor
V_{dc}, V_{qc}	d and q axis component of series capacitor voltage
V_{dt}, V_{qt}	d and q axis component of stator voltage of synchronous generator
E'_d	Induced emf due to flux linkage in the damper winding of synchronous generator
E'_q	Induced emf due to flux linkage in the field winding of synchronous generator
s_g	Slip of induction generator
s_m	Slip of induction motor
ω_m	Speed of induction motor
ω	Rotor speed of synchronous generator
δ	Rotor position of synchronous generator

V_x	Output voltage from measurement transducer in AVR
E_{fd}	Voltage applied to the field winding of synchronous machine
T_m	Mechanical torque input to the generator (Induction or synchronous generator)

Bibliography

[1] G. Jancke, N. Fahlen, and O. Nerf, "Series capacitors in power systems," *IEEE Transactions on Power Apparatus and Systems*, vol. 94, no. 3, pp. 915–925, 1975.

[2] S. Miske, "Considerations for the application of series capacitors to radial power distribution circuits," *IEEE Transactions on Power Delivery*, vol. 16, no. 2, pp. 306–318, 2001.

[3] J. Miller, M. Brunet-Watson, and J. Leighfield, "Review of series compensation for transmission lines," *PSC North America Specialist Consultant to the Electricity Industry*, 2014.

[4] E. W. Kimbark, "Improvement of system stability by switched series capacitors," *IEEE Transactions on Power Apparatus and Systems*, vol. PAS-85, no. 2, pp. 180–188, 1966.

[5] E. P. Soares-Ramos, L. de Oliveira-Assis, R. Sarrias-Mena, and L. M. Fernández-Ramírez, "Current status and future trends of offshore wind power in europe," *Energy*, vol. 202, p. 117787, 2020.

[6] T. Ackermann, *Wind power in power systems*. John Wiley & Sons, 2012.

[7] C. Canizares, "On bifurcations, voltage collapse and load modeling," *IEEE Transactions on Power Systems*, vol. 10, no. 1, pp. 512–522, 1995.

[8] C. Vournas, M. Pai, and P. Sauer, "The effect of automatic voltage regulation on the bifurcation evolution in power systems," *IEEE Transactions on Power Systems*, vol. 11, no. 4, pp. 1683–1688, 1996.

[9] V. Ajjarapu, *Computational techniques for voltage stability assessment and control*. Springer Science & Business Media, 2007.

[10] C. Rajagopalan, B. Lesieutre, P. Sauer, and M. Pai, "Dynamic aspects of voltage/power characteristics (multimachine power systems)," *IEEE Transactions on Power Systems*, vol. 7, no. 3, pp. 990–1000, 1992.

[11] N. Mithulananthan, C. A. Cañizares, and J. Reeve, "Indices to detect hopf bifurcations in power systems," in *Proc. of NAPS*, vol. 2. Citeseer, 2000, pp. 15–23.

[12] J. Devadason, P. Moses, and W. Fei, "Bifurcation analysis of weak electrical grids considering different load representations," in *2019 IEEE 7th International Conference on Smart Energy Grid Engineering (SEGE)*, 2019, pp. 208–212.

[13] C. A. Cañizares and W. Rosehart, "Bifurcation analysis of induction motor loads for voltage collapse studies," in *Proc. North American Power Symposium (NAPS), MIT*. Citeseer, 1996, pp. 559–565.

[14] W. D. Rosehart and C. A. Cañizares, "Bifurcation analysis of various power system models," *International Journal of Electrical Power & Energy Systems*, vol. 21, no. 3, pp. 171–182, 1999.

[15] C. Rajagopalan, P. Sauer, and M. Pai, "Analysis of voltage control systems exhibiting hopf bifurcation," in *Proceedings of the 28th IEEE Conference on Decision and Control,*, 1989, pp. 332–335 vol.1.

[16] E. H. Abed and P. P. Varaiya, "Nonlinear oscillations in power systems," *International Journal of Electrical Power & Energy Systems*, vol. 6, no. 1, pp. 37–43, 1984.

[17] C.-W. Tan, M. Varghese, P. Varaiya, and F. Wu, "Bifurcation, chaos, and voltage collapse in power systems," *Proceedings of the IEEE*, vol. 83, no. 11, pp. 1484–1496, 1995.

[18] M. Pai, P. W. Sauer, B. C. Lesieutre, and R. Adapa, "Structural stability in power systems-effect of load models," *IEEE Transactions on Power Systems*, vol. 10, no. 2, pp. 609–615, 1995.

[19] S. Ayasun, C. Nwankpa, and H. Kwatny, "Computation of singular and singularity induced bifurcation points of differential-algebraic power system model," *IEEE Transactions on Circuits and Systems I: Regular Papers*, vol. 51, no. 8, pp. 1525–1538, 2004.

[20] W. Marszalek and Z. Trzaska, "Singularity-induced bifurcations in electrical power systems," *IEEE Transactions on Power Systems*, vol. 20, no. 1, pp. 312–320, 2005.

[21] I. Dobson and L. Lu, "Voltage collapse precipitated by the immediate change in stability when generator reactive power limits are encountered," *IEEE Transactions on Circuits and Systems I: Fundamental Theory and Applications*, vol. 39, no. 9, pp. 762–766, 1992.

[22] L. Chen and Y. Min, "Limit induced bifurcation caused by SVC capacity limit," in *2007 IEEE Lausanne Power Tech*, 2007, pp. 250–254.

[23] A. Lerm, C. Canizares, and A. Silveira e Silva, "Multiparameter bifurcation analysis of the south brazilian power system," *IEEE Transactions on Power Systems*, vol. 18, no. 2, pp. 737–746, 2003.

[24] A. A. Lerm, C. A. Cañizares, F. A. Lemos, and A. S. e Silva, "Multi-parameter bifurcation analysis of power systems," in *Proceedings of the North American Power Symposium*. Citeseer, 1998, pp. 76–82.

[25] B. Lee and V. Ajjarapu, "A piecewise global small-disturbance voltage-stability analysis of structure-preserving power system models," *IEEE Transactions on Power Systems*, vol. 10, no. 4, pp. 1963–1971, 1995.

[26] I. Dobson, J. Zhang, S. Greene, H. Engdahl, and P. Sauer, "Is strong modal resonance a precursor to power system oscillations?" *IEEE Transactions on Circuits and Systems I: Fundamental Theory and Applications*, vol. 48, no. 3, pp. 340–349, 2001.

[27] L. A. Kilgore, L. C. Elliott, and E. R. Taylor, "The prediction and control of self-excited oscillations due to series capacitors in power systems," *IEEE Transactions on Power Apparatus and Systems*, vol. PAS-90, no. 3, pp. 1305–1311, 1971.

[28] C. F. Wagner, "Self-excitation of induction motors with series capacitors," *Electrical Engineering*, vol. 60, no. 12, pp. 1241–1247, 1941.

[29] J. W. Butler and C. Concordia, "Analysis of series capacitor application problems," *Transactions of the American Institute of Electrical Engineers*, vol. 56, no. 8, pp. 975–988, 1937.

[30] D. Walker, C. Bowler, R. Jackson, and D. Hodges, "Results of subsynchronous resonance test at mohave," *IEEE Transactions on Power Apparatus and Systems*, vol. 94, no. 5, pp. 1878–1889, 1975.

[31] J. W. Ballance and S. Goldberg, "Subsynchronous resonance in series compensated transmission lines," *IEEE Transactions on Power Apparatus and Systems*, vol. PAS-92, no. 5, pp. 1649–1658, 1973.

[32] K. Padiyar, *Analysis of subsynchronous resonance in power systems*. Springer Science & Business Media, 2012.

[33] A. Mulawarman and P. Mysore, "Detection of undamped sub-synchronous oscillations of wind generators with series compensated lines," in *Minnesota Power Systems Conference*, 2011.

[34] J. Adams, V. A. Pappu, and A. Dixit, "ERCOT experience screening for sub-synchronous control interaction in the vicinity of series capacitor banks," in *2012 IEEE Power and Energy Society General Meeting*. IEEE, 2012, pp. 1–5.

[35] L. Fan, R. Kavasseri, Z. L. Miao, and C. Zhu, "Modeling of DFIG-based wind farms for SSR analysis," *IEEE Transactions on Power Delivery*, vol. 25, no. 4, pp. 2073–2082, 2010.

[36] H. Liu, X. Xie, Y. Li, H. Liu, and Y. Hu, "A small-signal impedance method for analyzing the SSR of series-compensated DFIG-based wind farms," in *2015 IEEE Power Energy Society General Meeting*, 2015, pp. 1–5.

[37] H. A. Mohammadpour and E. Santi, "Sub-synchronous resonance analysis in DFIG-based wind farms: Definitions and problem identification — part I," in *2014 IEEE Energy Conversion Congress and Exposition (ECCE)*, 2014, pp. 812–819.

[38] H. Mohammadpour and E. Santi, "Analysis of sub-synchronous resonance (SSR) in doubly-fed induction generator (DFIG)-based wind farms," *Synthesis Lectures on Power Electronics*, vol. 5, no. 3, pp. 1–64, 2015.

[39] H. Mohammadpour and E. Santi, "Sub-synchronous resonance analysis in DFIG-based wind farms: Mitigation methods — TCSC, GCSC, and DFIG controllers — part II," in *2014 IEEE Energy Conversion Congress and Exposition (ECCE)*, 2014, pp. 1550–1557.

[40] H. Mohammadpour, A.Ghaderi, H. Mohammadpour, and E. Santi, "SSR damping

in wind farms using observed-state feedback control of DFIG converters," *Electric Power Systems Research*, vol. 123, pp. 57–66, 2015.

[41] A. E. Leon, "Integration of DFIG-based wind farms into series-compensated transmission systems," *IEEE Transactions on Sustainable Energy*, vol. 7, no. 2, pp. 451–460, 2016.

[42] U. Karaagac, S. O. Faried, J. Mahseredjian, and A.-A. Edris, "Coordinated control of wind energy conversion systems for mitigating subsynchronous interaction in DFIG-based wind farms," *IEEE Transactions on Smart Grid*, vol. 5, no. 5, pp. 2440–2449, 2014.

[43] R. K. Varma and S. Auddy, "Mitigation of subsynchronous oscillations in a series compensated wind farm with static var compensator," in *2006 IEEE Power Engineering Society General Meeting*, 2006, pp. 7 pp.–.

[44] R. K. Varma, S. Auddy, and Y. Semsedini, "Mitigation of subsynchronous resonance in a series-compensated wind farm using FACTS controllers," *IEEE Transactions on Power Delivery*, vol. 23, no. 3, pp. 1645–1654, 2008.

[45] A. Moharana, R. K. Varma, and R. Seethapathy, "SSR alleviation by STATCOM in induction-generator-based wind farm connected to series compensated line," *IEEE Transactions on Sustainable Energy*, vol. 5, no. 3, pp. 947–957, 2014.

[46] R. Varma and A. Moharana, "SSR in double-cage induction generator-based wind farm connected to series-compensated transmission line," *IEEE Transactions on Power Systems*, vol. 28, no. 3, pp. 2573–2583, 2013.

[47] A. Moharana and R. K. Varma, "Subsynchronous resonance in single-cage self-excited-induction-generator-based wind farm connected to series-compensated lines," *IET Generation, Transmission Distribution*, vol. 5, no. 12, pp. 1221–1232, 2011.

[48] A. Nayfeh, A. Harb, C. Chin, A. Hamdan, and L. Mili, "A bifurcation analysis of subsynchronous oscillations in power systems," *Electric power systems research*, vol. 47, no. 1, pp. 21–28, 1998.

[49] A. Nayfeh, A. Harb, C. Chin, A. Hamdan, and L. Mili, "Application of bifurcation

theory to subsynchronous resonance in power systems," *International Journal of Bifurcation and Chaos*, vol. 8, no. 01, pp. 157–172, 1998.

[50] M. Varghese, F. Wu, and P. Varaiya, "Bifurcations associated with sub-synchronous resonance," *IEEE Transactions on Power Systems*, vol. 13, no. 1, pp. 139–144, 1998.

[51] W. Zhu, R. Mohler, R. Spee, W. Mittelstadt, and D. Maratukulam, "Hopf bifurcations in a SMIB power system with SSR," *IEEE Transactions on Power Systems*, vol. 11, no. 3, pp. 1579–1584, 1996.

[52] M. Widyan, "On the effect of AVR gain on bifurcations of subsynchronous resonance in power systems," *International Journal of Electrical Power & Energy Systems*, vol. 32, no. 6, pp. 656–663, 2010.

[53] W. Ji and V. Venkatasubramanian, "Hard-limit induced chaos in a fundamental power system model," *International Journal of Electrical Power & Energy Systems*, vol. 18, no. 5, pp. 279–295, 1996.

[54] B. Rout, D. Lal, and A. Barisal, "Control of period doubling bifurcation in an SMIB power system using adaptive controller based on lasalle's invariant principle," *Cogent Engineering*, vol. 4, no. 1, p. 1362804, 2017.

[55] A. Mahmoud, T. Ortmeyer, R. Harley, and C. Calabrese, "Effects of reactive compensation on induction motor dynamic performance," *IEEE Transactions on Power Apparatus and Systems*, no. 3, pp. 841–846, 1980.

[56] D. Limebeer and R. Harley, "Subsynchronous resonance of single-cage induction motors," in *IEE Proceedings B-Electric Power Applications*, vol. 128, no. 1. IET, 1981, pp. 33–42.

[57] O. Ojo, "Electro-mechanical subsynchronous resonance of a series capacitive compensated line start induction motor drive," in *Conference Record of the IEEE Industry Applications Society Annual Meeting,*. IEEE, 1989, pp. 238–247.

[58] P. C. Krause and C. Thomas, "Simulation of symmetrical induction machinery," *IEEE transactions on power apparatus and systems*, vol. 84, no. 11, pp. 1038–1053, 1965.

[59] P. C. Krause, O. Wasynczuk, S. D. Sudhoff, and S. D. Pekarek, *Analysis of electric machinery and drive systems*. John Wiley & Sons, 2013, vol. 75.

[60] P. W. Sauer and M. A. Pai, *Power system dynamics and stability*. Wiley Online Library, 1998, vol. 101.

[61] A. Moharana and R. K. Varma, "Subsynchronous resonance in single-cage self-excited-induction-generator-based wind farm connected to series-compensated lines," *IET generation, transmission & distribution*, vol. 5, no. 12, pp. 1221–1232, 2011.

[62] P. Kundur, "Power system stability," *Power system stability and control*, pp. 7–1, 2007.

[63] A. K. Moharana, "Subsynchronous resonance in wind farms," Ph.D. dissertation, The University of Western Ontario, 2012.

[64] J. Undrill, A. Renno, and G. Drobnjak, "Dynamics of a large induction motor load system," in *2003 IEEE Power Engineering Society General Meeting (IEEE Cat. No.03CH37491)*, vol. 3, 2003, pp. 1398–1403 Vol. 3.

[65] "IEEE recommended practice for application of controllers and automation to industrial and commercial power systems," *IEEE Std 3001.11-2017*, pp. 1–91, 2017.

[66] M. A. Mahmud, M. Hossain, and H. Pota, "Effects of large dynamic loads on power system stability," *International Journal of Electrical Power & Energy Systems*, vol. 44, no. 1, pp. 357–363, 2013.

APPENDIX A

Parameters of the induction generators IG1, IG2 and the wind turbine considered in this dissertation are presented in this Tables A.1 and A.2 respectively.

Table A.1: Parameters of IG1

Parameter	Value
Stator resistance (R_s)	0.01105 pu
Rotor resistance (R_r)	0.01102 pu
Stator leakage reactance (X_{ls})	0.0507 pu
Rotor leakage reactance (X_{lr})	0.0507 pu
Magnetizing reactance (X_m)	3.0729 pu
Inertia constant (H_{ig})	2 s

Table A.2: Parameters of IG2

Parameter	Value
Stator resistance (R_s)	0.01 pu
Rotor resistance (R_r)	0.05 pu
Stator leakage reactance (X_{ls})	0.10 pu
Rotor leakage reactance (X_{lr})	0.08 pu
Magnetizing reactance (X_m)	3 pu
Inertia constant (H_{ig})	0.5 s

APPENDIX B

The parameters of the induction motor and the synchronous generator considered in this dissertation are presented below:

Table B.1: Parameters of induction motor load

Parameter	Value
Stator resistance (R_s)	0.02 pu
Rotor resistance (R_r)	0.025 pu
Stator leakage reactance (X_{ls})	0.08 pu
Rotor leakage reactance (X_{lr})	0.08 pu
Magnetizing reactance (X_m)	4 pu
Inertia constant (H_{im})	1 s

Table B.2: Parameters of synchronous generator

Parameter	Value
Armature resistance (R_a)	0.001 pu
Steady state reactance (X_d)	1.75 pu
Steady state reactance (X_q)	1.65 pu
Transient reactance (X'_d)	0.3 pu
Transient reactance (X'_q)	0.75 pu
Transient time constant (T'_{do})	5 s
Transient time constant (T'_{qo})	1 s
Inertia constant (H)	4 s